PERFORMANCE LIMITS OF LINEAR VARIABLE-RELUCTANCE MOTORS IN CONTROLLED LINEAR MOTION APPLICATIONS

A Thesis
Presented to
The Academic Faculty

by

Raga Ahmed

In Partial Fulfillment
of the Requirements for the Degree
Doctor of Philosophy in the
School of Electrical and Computer Engineering

Georgia Institute of Technology
December, 2013

PERFORMANCE LIMITS OF LINEAR VARIABLE-RELUCTANCE MOTORS IN CONTROLLED LINEAR MOTION APPLICATIONS

Approved by:

Dr. David G. Taylor, Advisor
School of Electrical and Computer Engineering
Georgia Institute of Technology

Dr. A. P. Sakis Meliopoulos
School of Electrical and Computer Engineering
Georgia Institute of Technology

Dr. Ronald G. Harley
School of Electrical and Computer Engineering
Georgia Institute of Technology

Dr. Nader Sadegh
School of Mechanical Engineering
Georgia Institute of Technology

Dr. Thomas G. Habetler
School of Electrical and Computer Engineering
Georgia Institute of Technology

Date Approved: August 20, 2013

ACKNOWLEDGEMENTS

Professor David G. Taylor directed this research, and I am profoundly indebted to him for his significant support: for spending long hours reviewing and commenting on my work, for generously sharing his technical and pedagogical expertise, for his patience and for his kindness. Prof. Taylor is equally remarkable as a classroom teacher and as a research advisor.

I would like to thank members of my Final Defense Committee for their time and effort reading this dissertation, providing feedback and carrying out the steps necessary for the completion of this work. Prof. Harley and Prof. Habetler taught me concepts of power electronics and electric machinery and I grew to admire them immensely; I am also grateful for the brief time in the past that I enjoyed working with Prof. Meliopoulos. I am grateful and honored that Prof. Sadegh has granted my wish for him to join and complete this committee.

Many others at Georgia Tech helped on numerous occasions: Prof. Bonny Heck Ferri, Dr. Nattapon Chayopitak, Matt Hortman, Marilou Mycko, Jacqueline Trappier, Dr. Daniela Staiculescu, Chris Malbrue, and Diana Fouts.

Special thanks must go to all members of my family for their long lasting support and encouragement and to my best friends. Thanks must also go to Nelson and Belen for hours of fruitful discussion and encouragement.

I owe immeasurable and unpayable debts to Alla and Nahzik: I am grateful to Nahzik for her sweet regard and patience and for the inspiration brought about by her budding wisdom and unmistakable forthrightness, and to Alla for shouldering enormous weights on my behalf, for his steady and unyielding support and for his consistently gentle spirit.

TABLE OF CONTENTS

LIST OF TABLES

LIST OF FIGURES

SUMMARY

The main objective of this research is to demonstrate improved actuator point-to-point positioning performance, as measured by settling time, for manufacturing automation applications such as circuit board assembly and other product-transfer operations. Automation tasks generally involve multi-axis motion, but in order to simplify the control task, it is often possible to plan motion control separately for each actuation device involved. The control objective then is to move a single mass in a single axis from a starting position to a target position following the fastest possible motion trajectory while meeting final-position accuracy requirements. Position control involves generating and imposing the actuator force command required to accelerate the mass according to the planned motion trajectory. Thus the actuator's achievable force that is available for acceleration is the fundamental variable that determines optimal settling time. Achievable force is of course limited by constraints on heat dissipation but also possibly by additional application-specific constraints.

The actuator technology employed is the linear variable reluctance motor. Achieving maximum possible force requires optimal excitation. Naturally, achievable force limits vary with the existence and tightness of constraints. In this research, higher force capability is achieved when force-ripple constraints, which have been customarily emphasized in positioning applications, are relaxed. The higher capability is exploited by adopting faster motion trajectories, which are then imposed under feedback control to achieve faster settling time. Improved force capability with relaxed ripple constraints is demonstrated by generating average force versus speed capability curves under ripple constraints ranging from minimal ripple to unconstrained

ripple. Improved positioning performance, with relaxed ripple constraints and without violating the final-position accuracy specification, is demonstrated by computing and comparing settling time for multiple positioning tasks with trajectories based on both extremes of force capability, lowest (no-ripple) and highest (unconstrained-ripple) force limits.

Mathematical motor models and simulation programs are developed to help perform several tasks necessary for achieving the objectives of this research: (i) optimal commutation under force ripple constraints is computed to determine ripple-specified force limits and to provide excitation waveforms necessary for force production, (ii) motion profiles for several positioning task scenarios are generated based on computed ripple-specified force limits, (iii) state space integral position control simulations are performed to evaluate the degree of success of the proposed relaxation of force ripple constraints in improving settling time and (iv) the computed settling times for positioning tasks are examined in relation to the copper losses associated with them in order to assess the trade-off.

Two LVR motor configurations are investigated to examine whether or not the research results are limited to one actuator topology or to one excitation type. One motor configuration represents typical (i.e. switched) linear and rotary variable reluctance motors while the other exhibits features of both switched and synchronous varieties of variable reluctance motors. Improvements in settling time resulting from relaxing force ripple constraints are demonstrated for both configurations and are found to be more pronounced for the uncoupled configuration.

CHAPTER 1

INTRODUCTION

Point-to-point positioning, the controlled motion of an object from one point to another, is the principal task performed by robotic machines in manufacturing automation applications such as circuit board assembly and other product-transfer operations. Because of global competition, automation industries are under great market pressure to minimize production cycle times while meeting increasing demands on production quality and versatility. Complex decision making is required at many levels from human and capital resource management, to production planning, to controlling the work flow and operation of the individual assembly machines. Point-to-point positioning control is at the most elementary level in such a hierarchy and naturally has a direct impact on production cycle time. Consequently, manufacturers of assembly machines are also under pressure to maximize the point-to-point positioning performance of the motion actuators inside their machines even as accuracy requirements become stricter.

The main contribution of this thesis is the improvement of settling time in point-to-point positioning applications which would lead to shorter cycle times and higher throughput. The following several sections introduce the main concepts and contain foundational material for the topics covered in this dissertation and serve to explain how these topics are inter-related. This chapter ends with previewing the thesis contributions and summarizing the organization of the remainder of this document.

1.1 Point-to-Point and Continuous-Path Control

The motion of an object from a starting point in space to a target point is characterized by a path (the position of all points in space the object passes through) and

a trajectory (the instants in time the object passes through the points). Robotic positioning control problems, depicted in Figure 1, are classified as continuous-path (e.g., seam welding) or point-to-point (e.g., circuit board assembly) control problems. Both control problems typically address three issues: path determination, trajectory generation and trajectory tracking using feedback control techniques. Continuous-path position control requires precise tracking of the whole path such as the complex contour of a welding seam. Point-to-point positioning control, on the other hand, requires no control of the path between the starting and target points, and so feedback control decisions concern only trajectories, but even then trajectory following is critical only at the target position. This facilitates shorter operation cycles for point-to-point positioning applications; in particular, when the desired positioning points are known a priori, and the workspace is clear of obstacles, optimized (fastest) motion plans can be stored and executed repeatedly in a predetermined sequence. The distinction between the two control problems is additionally important for this research because it brings into focus the position tracking freedom unique to point-to-point positioning and an opportunity for generating faster trajectories.

The freedom from continuous specifications for position tracking in the static sense (tracking the path) implies freedom from continuous specifications for position, speed and acceleration tracking in the dynamic sense (tracking the trajectory). Without this freedom, there is no inherent flexibility in the speed and acceleration requirements to move an infinitesimal distance from each point in the path to the next point. This influences trajectory generation decisions; it is common, for example, to minimize ripple in force production in order to improve force tracking and hence positioning accuracy, but this (and in general any constraint) must in some way diminish force capability. It is proposed here that trajectory tracking freedom allows use of maximum force capability (by relaxing select constraints) thus allowing faster trajectories, for point-to-point positioning, without detrimental effect on settling time

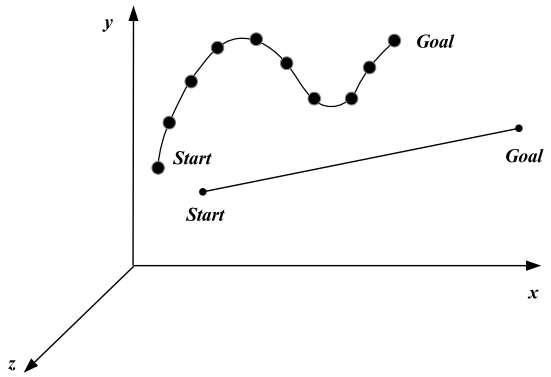

Figure 1: Points in space for continuous (top) and point-to-point paths.

and final-position accuracy. The assessment of settling time improvement based on this proposition is not straightforward and requires the detailed numerical studies documented in this dissertation.

1.2 Single-Axis Point-to-Point Positioning

Positioning tasks generally require multi-axis motion in various workspaces; for example, point-to-point moves in circuit board assembly cover a rectangular workspace and so a Cartesian configuration with three (x, y and z) linear and orthogonal axes of motion is appropriate. It is possible to plan motion separately for each axis thus simplifying the control problem. The principal positioning task then is for an actuator to move a single mass in a single axis from a starting position to a final settling position as fast as possible, yet meet final-position accuracy requirements. A single-mass motion system is shown in Figure 2 where a force, f, from an actuating device is applied to move the mass M along a linear axis (friction is ignored for clarity), resulting in position x. In general the actuator may be electrical, hydraulic or pneumatic. This system would constitute the plant in a feedback point-to-point position control system such as depicted in Figure 3.

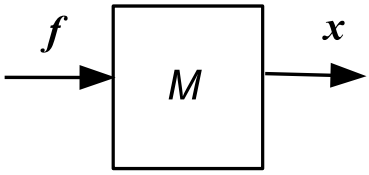

Figure 2: Single-axis linear motion system.

1.2.1 Time-Optimal Motion Trajectory

The minimum travel time, T_{opt}, to complete a point-to-point positioning task is obtained by solving the optimal control problem

$$\text{minimize} \quad T = \int_0^T 1 \; dt \tag{1}$$

$$\text{subject to} \quad M\ddot{x} = f \tag{2}$$

$$|f| \leq F \tag{3}$$

$$\begin{bmatrix} x(0) \\ \dot{x}(0) \end{bmatrix} = \begin{bmatrix} 0 \\ 0 \end{bmatrix}, \begin{bmatrix} x(T) \\ \dot{x}(T) \end{bmatrix} = \begin{bmatrix} \xi \\ 0 \end{bmatrix} \tag{4}$$

where T is the travel time, F is the maximum actuator force and ξ is the travel distance. The classical solution to this optimal point-to-point positioning problem is the so-called bang-bang solution where T_{opt} is given by

$$T_{\text{opt}} \;=\; 2\sqrt{\frac{\xi}{F/M}} \tag{5}$$

The corresponding motion trajectory has the shape shown in Figure 4, and for a given mass and a given travel distance, it is a function of only the maximum force available for acceleration. From (5), it is clear that T_{opt} decreases as F increases. It is implicitly assumed that full acceleration and full deceleration are instantaneously possible and that speeds are feasible up to the maximum speed at the peak of the triangular velocity profile. This time-optimal motion trajectory is not attempted in practice; rather, modified trajectories are obtained after imposing application-specific motion constraints such as maximum jerk (the rate of change of acceleration) and maximum

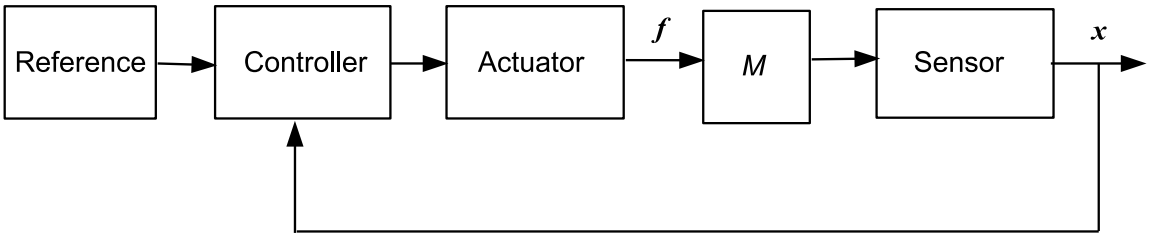

Figure 3: Point-to-point positioning control system block diagram.

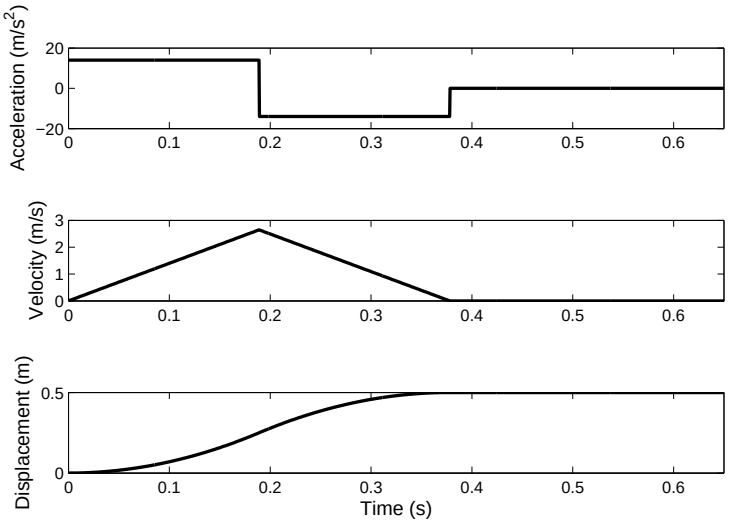

Figure 4: Time-optimal motion trajectory.

speed. The bang-bang trajectory becomes the idealized special case.

1.2.2 Realistic Motion Trajectories

There exist many mathematical models for generating motion trajectories subject to realistic motion constraints on speed, acceleration and jerk (denoted below by $S_{\max}$, $A_{\max}$ and $J_{\max}$ respectively):

$$|\dot{x}| \leq S_{\max} \tag{6}$$

$$|\ddot{x}| \leq A_{\max} \equiv F/M \tag{7}$$

$$|\dddot{x}| \leq J_{\max} \tag{8}$$

Model choice depends on the acceptable trade-off between achievable travel time and motion constraints. For example, a faster trajectory may involve higher jerk than

permitted for some applications. Two example practical motion trajectories using the time-optimal s-curve models in [1] are shown in Figure 5. Common parameters (force, distance and mass) with the time-optimal trajectory in Figure 4 are kept in obtaining the practical trajectories, but speed and jerk constraints are added. Clearly, additionally imposed motion constraints influence not only travel time but also the trajectory shape and whether or not travel at maximum speed is feasible for any length of time.

1.2.3 Measuring Positioning Performance

Precise definition of settling time, the positioning performance measure, is given with the help of Figure 6. This figure shows two generic curves, a desired position trajectory $x^d(t)$ and actual (sensed) position $x(t)$. The desired trajectory specifies a travel interval from t_i to t_f and an associated travel distance ξ from x_i to x_f. After t_f, the commanded position stays constant (at the target position x_f) until the next task begins. This is summarized below

$$x^d(t_i) = x_i \tag{9}$$

$$x^d(t_f) = x_f \tag{10}$$

$$\xi = x_f - x_i \tag{11}$$

Let $e(t)$ be the position error for the entire duration of the task and let $e_p(t)$ be the position error during the constant-position command interval:

$$e(t) = x^d(t) - x(t) \tag{12}$$

$$e_p(t) = e(t)|_{t \geq t_f} \tag{13}$$

Settling to target position is complete if $\max(|e_p(t)|) \leq \Delta x$ where Δx is the positioning tolerance. In other words, the effective settling time is the time elapsed between the start of motion at t_i and the earliest time, t_s, that $x(t)$ enters and stays

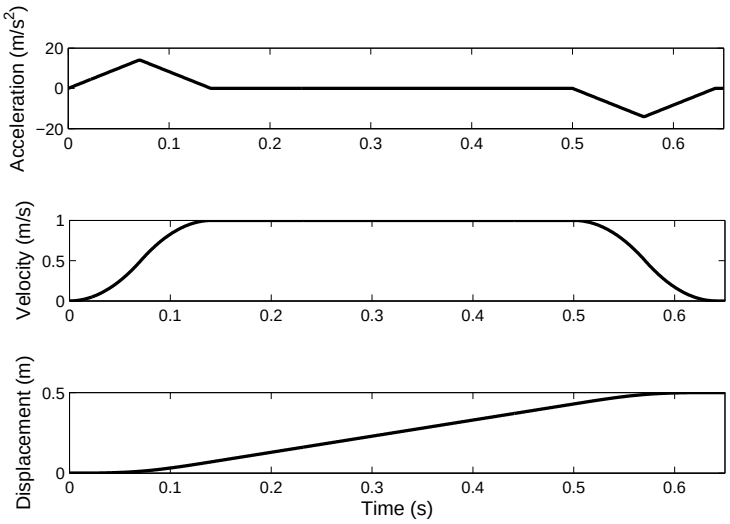

(a) Low jerk.

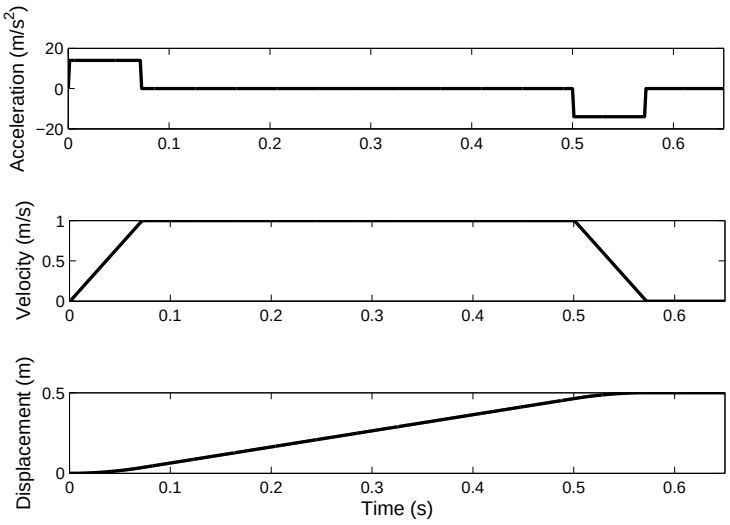

(b) High jerk.

Figure 5: Example s-curve trajectories. The optimal trajectory in Figure 4 adheres to the same force limit but ignores additional limits.

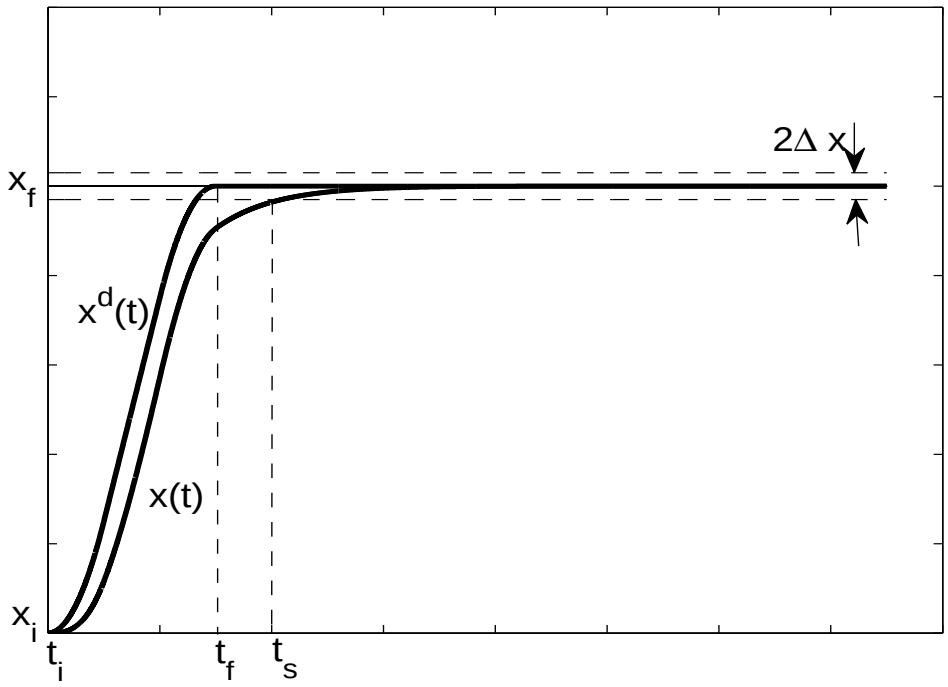

Figure 6: Positioning trajectory and tracking variables.

within an envelope of height $2\Delta x$ about the target position. The following terminology will be used for the various segments in Figure 6 and their associated time intervals:

$$\text{Nominal Travel Segment: } \tau_n = t_f - t_i \tag{14}$$

$$\text{Active Settling Segment: } \tau_a = t_s - t_f \tag{15}$$

$$\text{Effective Settling Segment: } \tau_s = t_s - t_i \tag{16}$$

1.2.4 Actuator Technology for Point-to-Point Positioning

The force necessary for robotic automation may come from electrical, hydraulic or pneumatic actuators, but electrical (DC or AC) motors are most popular [2]. The applications targeted in this research require controlled linear motion in one axis. Controlled linear motion is possible with rotary motors, but rotary-to-linear conversion mechanisms such as ball screws, lead screws, rack-and-pinions, or belts and pulleys are required. The ability of linear motors to directly drive the load without

such mechanisms facilitates higher performance [3, 4]; they feature simplified assembly, improved reliability (there are fewer parts and they are non-contacting), higher repeatability and accuracy (no backlash, higher stiffness), and lower maintenance cost. Challenges with direct drive motors include the lack of gearing, which results in the need for larger electromagnetic force both for moving the payload and rejecting disturbances.

The actuator technology selected for this research is linear variable reluctance (LVR) motors. Such motors are known for large inherent force ripple and higher complexity of control [5], [6]. The interest in LVR motors is inspired by commercialized products from NSK and Universal Instruments Corporation (UIC) and by the surge in research on LVR motor applications for manufacturing machines. NSK developed Megathrust, an LVR motor, for use in high-speed transfer systems for light weight materials [7] several years after its rotary counterpart (Megatorque) which had been used by the US firm Adept Technologies in direct drive robots. UIC has been using patented LVR technology in all its so-called platform positioning systems [8]. The choice of LVR motors for this research is further motivated by the fact that they require only the simplest materials and construction and because their naturally high force ripple may best allow the control design to take advantage of the additional tracking performance freedom described in Section 1.1.

Force capability at any speed, typically depicted by a force-speed curve, is a function of motor magnetic design and operation constraints such as maximum converter voltage. Other constraints include limits on heat dissipation (to ensure integrity of motor coils) and limits on force ripple (for example to avoid mechanical damage from vibrations). Heat dissipation is an unavoidable consequence of force production and its reduction is a common goal regardless of the application or the motor type. Force ripple and torque ripple in linear and rotary VR motors is a consequence of the salient

teeth situated on both sides of the air gap. Because of this double saliency, VR motors have a spatially-periodic variable reluctance (VR) to magnetic flux flow through the non-uniform air gaps giving these motors their name. Force ripple in VR motors is a prominent factor in excitation design and in force (or torque) characteristics; consequently it impacts their positioning performance and is central in this dissertation. The influence of force ripple on structure vibration and on settling time is not investigated in this research; however, this topic is discussed briefly in Sections 1.3.2.1 and 5.3.

1.2.5 Linear Variable Reluctance Motors

Theoretically there is a linear counterpart for every rotary motor including the rotary VR motor. This section is about LVR motors and describes their construction and principles of operation. Background information on various types of brushless linear motors is found in [3, 4, 9, 10], and a summary of advances in linear motors and their industrial and transport applications is found in [11]. Valuable information pertinent to LVR motors can be gained from the existing rich treatment of their rotary counterparts such as found in [12]-[17].

Two LVR motor configurations, coupled and uncoupled, are considered in this research. The coupled configuration (Figure 7 (a)) relies on shared magnetic paths, where the flux induced by energizing one phase necessarily links the turns of the other phases, whereas the uncoupled configuration (Figure 7 (b)) consists of noninteracting magnetic paths. The main parts of these motors are named in Figure 8 (shown using the coupled configuration).

All linear motors have two parts on opposite sides of an air gap. The moving part is called the translator and the stationary part is called the stator. Either one of the two main parts, designated the active part, houses energized windings that are wound around (toothed) poles and are responsible for producing magnetic flux; the other part

is designated the passive part. In LVR motors, both the passive and active parts have a magnetically salient structure that causes the reluctance of the magnetic flux path to vary with displacement, giving these motors their name. LVR motors take many configurations, but this research is concerned with rectangular framed LVR motors with (1) flat air gaps (cylindrical motors have tubular air gaps), (2) concentrated coils (the synchronous variety of variable-reluctance motors has distributed winding), (3) double air gap (the moving part is made of two connected external pieces and the stationary part is sandwiched between (internal to) them, (4) flux paths through the magnetic material in directions that are parallel (longitudinal flux) as opposed to perpendicular (transverse flux) to the direction of mechanical motion, (5) toothed structure in the magnetic material at the air gap to provide the saliency necessary for operation (with anisotropic structures, the saliency is achieved by constructing the core from both magnetic and non-magnetic materials arranged in a suitable pattern) and (6) three phases (the minimum number of phases for controlled motion in either direction).

The middle toothed bar in both configurations of Figure 7 constitutes the passive stator. The identical top and bottom parts holding toothed poles and concentrated coils make the active translator (for comparative advantages of concentrated windings with permanent magnet motors as opposed to distributed windings, see [18]–[20]). Each phase winding is a series connection of the coils belonging to that phase (bearing the same phase number in the figure). The misalignment between opposing stator and translator teeth ensures the generation of force favoring alignment: When current flows in one or more phase windings, electromagnetic fluxes flow and interact with magnetic poles formed within the non-uniformly magnetized material of the salient structure, and force is developed due to the tendency of magnetic fields to align. The uniform distribution of poles and teeth allows repeating operation in cycles. The fundamental cycle of operation corresponds to how much motion is needed before

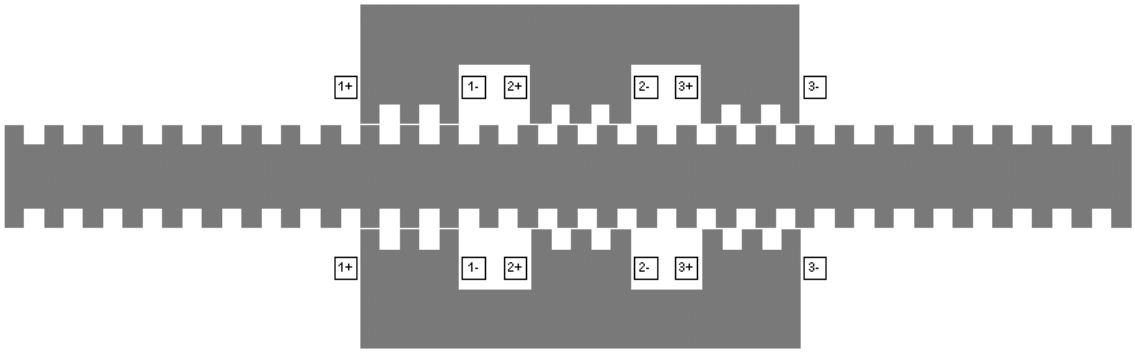

(a) Coupled configuration.

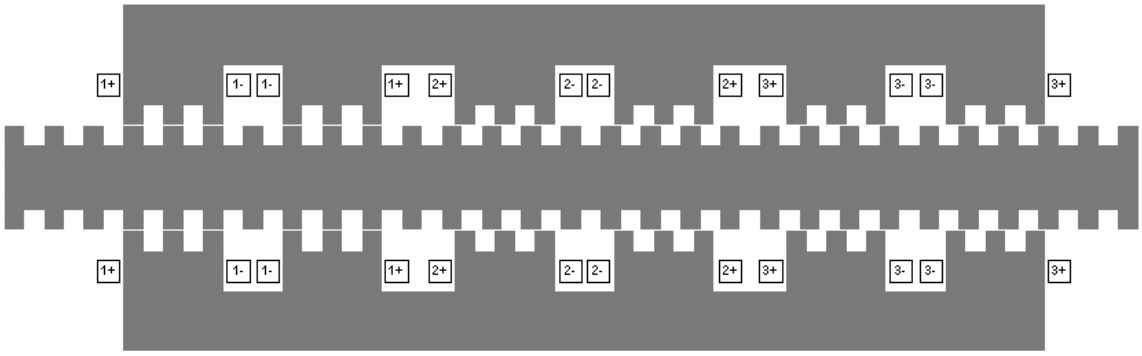

(b) Uncoupled configuration.

Figure 7: Linear variable-reluctance motors.

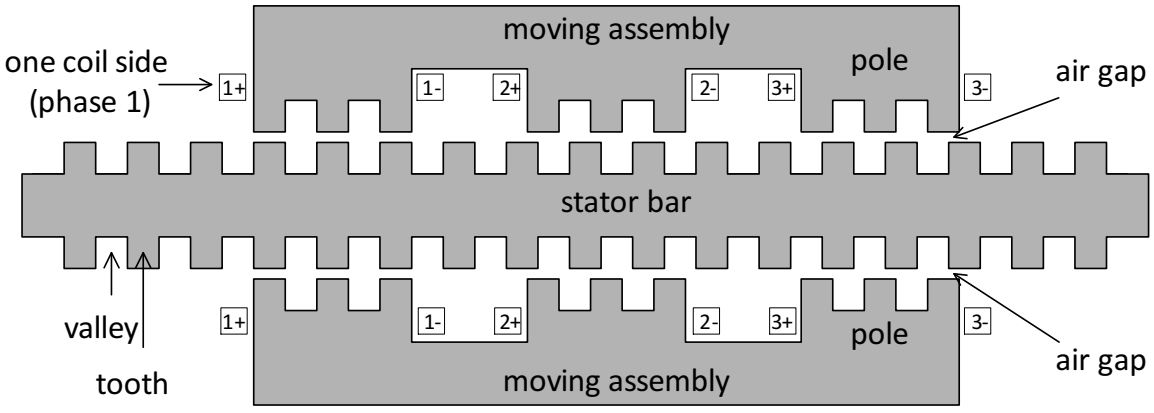

Figure 8: Linear variable-reluctance motor parts.

stator and translator teeth return to the same orientation relative to each other. Representative steps of this cycle are shown in Figure 9.

If both configurations have a common tooth pitch, a common tooth width, and a common depth or third dimension, then their stator bars will be identical (as in the figure). Considering both configurations and keeping as much as possible in common provides the opportunity to examine whether or not superior performance can be attributed to the existence of magnetic coupling or the lack thereof. In addition, considering these two configurations helps examine whether or not the research results are limited to one actuator topology or to one excitation type. The uncoupled motor represents typical (i.e. switched) linear and rotary variable reluctance motors while the coupled motor exhibits features of both switched and synchronous varieties of variable reluctance motors.

The publications cited in this chapter chronicle the evolution of LVR motors into viable competitors to other linear motors in various motion applications and their successful development for industrial use in electronics assembly equipment. Cited advantages over other linear motors include modularity, lower construction cost, higher reliability, higher force/mass ratios, electromagnetic gearing and inherent position sensing due to salient or toothed structure in the passive part. In comparison to induction motors, VR motors have coils on only the active component limiting resistive heating to that one component; they require no flux estimation to achieve high performance control regardless of speed of operation. In comparison to permanent magnet motors, VR motors do not suffer from the high cost of permanent magnets or over-heating and potential for demagnetization.

1.3 Research Objectives and Literature Review

The objective of this research is to ascertain and demonstrate improvements in point-to-point positioning, using LVR motors as the actuating technology. Doing so requires

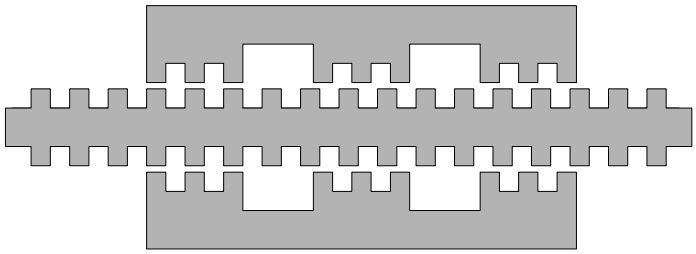

(a) $x = 0$ (exact alignment for phase 1).

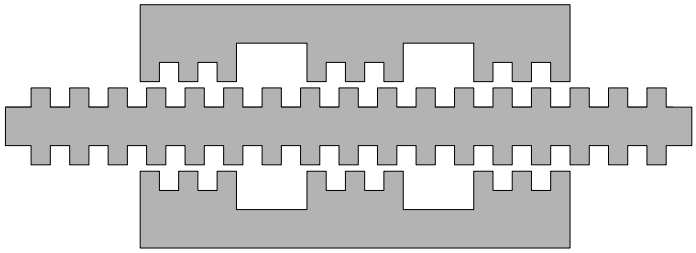

(b) $x = \frac{1}{6}$ cycle.

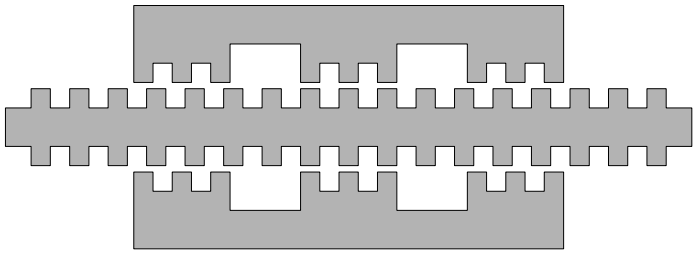

(c) $x = \frac{1}{3}$ cycle.

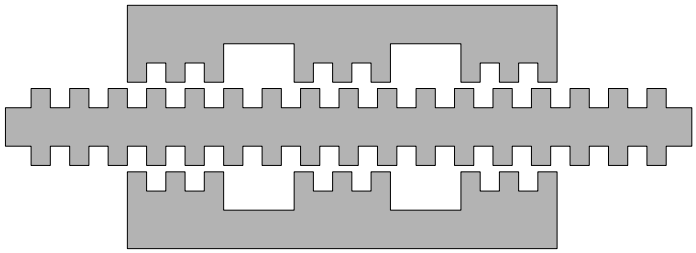

(d) $x = \frac{1}{2}$ cycle.

Figure 9: Several displacements in half a cycle of motion.

- Derivation of force models and quantification of force ripple for LVR motors with coupled and uncoupled phases
- Determination of the optimal ripple-specified commutation
- Assessment of positioning performance in terms of settling time and average power dissipation

All topics listed above are subjects of active research, but the overall objective of this research as stated above, and the entirety of the framework that combines these tasks in order to achieve the research objective, have never before been reported in the published literature. A review of relevant published research in relation to these topics is presented next.

1.3.1 LVR Motor Modeling

Mathematical modeling is necessary for motor characterization and control. Idealized modeling (ignoring magnetic material saturation and, in some cases, higher spatial harmonics) and more accurate modeling using finite element analysis are presented in Chapter 2. The idealized models come from magnetic circuit analysis with flux-tube based air-gap permeances; these models were first reported in [21] and [22] for the coupled motor and in [23] for the uncoupled motor. The linear model was applied in [24, 25] to show the applicability of the uncoupled motor as a direct drive robot actuator: single-phase and double-phase operation were tested under feedback control with electronic (logic-function-based) commutation.

Early efforts to model or compensate for non-linear behavior, e.g. by modifying the control input [25], seem to be based on heuristics and experience. The first mathematical representation of the magnetic system that makes no simplifying assumptions was introduced in [26] (for the uncoupled motor) using function fitting to measured flux linkage data; it was used to derive a dynamic uncoupled motor model for the

full range of operation, including saturation. More recent publications on the coupled motor include [27]-[29], where a nonlinear magnetic circuit model is developed and is used to simulate the dynamic behavior of the motor.

Models exist in the literature for LVR motors other than the coupled and uncoupled motors of this dissertation. MCA methods assuming linear magnetics are reported in [30], and accounting for nonlinear magnetics in [31] and in [32], but in the latter it was used only for two critical relative positions of stator and translator teeth (fully aligned and fully unaligned). Models seeking a compromise between accuracy and computational efficiency are discussed in [33]-[35]. More accurate modeling, e.g. using finite element analysis, is discussed in [36]-[39]. In [40], measurement data is saved in look-up tables and used in the implementation of an LVR motor in precise positioning.

This research employs the idealized models, but expands on them in order to obtain new results, gain insight and conduct investigations with clarity (some investigation results have been published in [41]-[46] and more recent results have been published in [47] and [48]). The finite-element-based models in Chapter 2 are derived by function fitting not only to flux linkage data but also to magnetic energy and thrust force all at the same time enabling a better fit. Moreover, the resulting models are smooth functions throughout as opposed to tabular models with multilinear interpolation. The model for the uncoupled motor completely characterizes that motor while the coupled motor model is limited to single-phase excitation.

1.3.2 Optimal Commutation of LVR Motors

Optimal commutation of VR motors is concerned with determining optimized current profiles for desired force production; common objectives include maximizing force production, minimizing power dissipation (from copper losses) or minimizing force ripple. Optimal excitation to minimize ripple so as to produce smooth force or torque

dominates the literature ([49]-[58]). With few exceptions, in all published research on optimal excitation of linear and rotary VR motors, assumptions are made a priori on the positions (or angular positions) for turning a phase on or off (based on the slope of the inductance curve and the desired direction of force) and on the number of phases that can be excited simultaneously. Multiple-phase excitation is studied, but still under the turn-on turn-off assumptions in [59] where two-phase excitation is found to result in reduced peaks and reduced rates of change of currents resulting in reduced ripple and reduced normal force (more important for single sided motors where normal force is not balanced). Minimization of average power dissipation has been examined in [60] and [61] without a priori assumptions for rotary variable reluctance motors and the results apply to the uncoupled motor (Figure 7 (b)). Both maximization of force production and minimization of copper losses without a priori assumptions are reported in [62] for the coupled configuration; however, the formulation of these problems assumes current sources as controls without any consideration of voltage limits.

The optimal commutation in this research differs from these publications and all published research in redefining the commutation problems to include force ripple specification. It extends previously published work by covering the complete range of force-ripple values from no ripple (smooth force) to unconstrained ripple for both maximum force and minimum average power dissipation problems. The commutation results are conveniently employed in the assessment of LVR motor force-speed limits as covered in Chapter 3. Commutation results are also used in computing phase currents to be used during controlled operation as covered in Chapter 4.

1.3.2.1 Force Ripple and Structure Vibration

Vibration problems due to flexibility in structures may arise in many engineering areas; tall buildings, suspended bridges, cranes, automobiles and robots all exhibit

vibratory behavior. Structure vibration is not investigated in this research; however, its consideration would be a natural and important extension to this work; specifically, it is important to find out how vibratory behavior (and ultimately settling time) is influenced by the proposed non-conventional high force-ripple commutation strategy. Brief comments on select publications [63]–[71] are given here and useful insight from them is further discussed in Section 4.1.1.5. These publications are chosen because they address one or more relevant issues, namely (i) motor configurations like the ones studied in this dissertation (describing vibration causes and vibration reduction), (ii) measures that can be applied successfully towards the end of motion to recover from the vibrations induced by fast motion (suggesting that any residual vibration caused by the proposed high-ripple commutation strategy may be similarly overcome) and (iii) command shaping methods that modify force (acceleration) reference trajectories similar to those used in this research and produce trajectories that will not excite the resonances of system structures (suggesting that optimal commutation design may be modified to accommodate vibration reduction measures in the force production process).

In general, when robots are moved rapidly they experience vibrations which can excite resonances and as a result improvements in move time by commanding fast motion may be offset by the wait time required to allow residual vibrations to subside to acceptable levels [63]. Flexibility in robotic manipulators is unavoidable (given constraints imposed by manufacturing and operating costs, as well as by various operating environments) and causes residual vibration that can degrade trajectory tracking and thus require vibration reduction measures such as input shaping [64]. Oscillatory behavior makes precise-pointing or tip-positioning in applications such as robotic booms in the aerospace industry a daunting task that requires complex closed-loop control [65].

A patent [66] on vibration reduction methodology issued for UIC (a developer of

linear and rotary VR motor technology for electronic assembly and other product transfer applications [8]) concerns the coupled LVR motor configuration of Figure 7 (a). In [66] the stator is described as susceptible to vibration (being a pseudo simply supported beam). Vibrations are said to occur mainly when the system is approaching the target position and is moving slowly, and are attributed to (i) reduced stiffness resulting from the reduction in normal forces between the stator and the translator as phase currents get smaller and (ii) the high gains used in the velocity control loop; resonance frequencies are found to be within the desired (for fast positioning) velocity control loop bandwidth. Three measures for vibration suppression are described in [66]. First, bearings are mounted on the translator via mechanical dampers and contact the stator so that stator vibrations are transmitted to the bearings and dissipated in the dampers. Second, excitation computation is modified so that, even at zero commanded (lateral) force, currents are applied in at least one phase so that normal force never falls below an empirically determined level; only the magnitude of the normal force is emphasized and is satisfied through switched excitation that provides the desired normal and lateral forces with no emphasis on the ripple content of the lateral force. Third, conditional (applied near target position) filtering is used to reduce the velocity loop gain and thus reduce closed loop sensitivity to vibrations.

The feedforward method of command shaping applies without regard to the particular form of the desired trajectory and has been applied successfully (including with modifications for example to accommodate nonlinear behavior) in several different applications [64]; a comparison of input shaping methods is given in [67]. In [68] input shaping has been applied to a Cartesian robot to modify a square wave force input (corresponding to the time optimal trajectory shown in Figure 4) resulting in vibration reduction even when resonant frequencies varied (in a manner similar to variations observed in an actual system) from the nominal values used in command shaping. Vibration reduction is also achieved for the same system when velocity

constraints were included in trajectory generation [69]. In [70] a method has been presented for concurrently designing a PD feedback position controller and an input shaper that performed better than PD control alone. The design method takes into account limits on allowable residual vibration as well as overshoot and actuator effort (with the possibility to integrate other requirements). Additional methods and more literature references can be found in [71].

1.3.3 Positioning Performance Assessment

The capability of LVR motors with uncoupled phases to provide controlled linear motion at low speeds has been recognized for some time; this is evidenced by early publications such as [24, 25, 72]. The potential performance, particularly as measured by force density, of rectangular and cylindrical LVR motors in controlled motion applications is discussed in [73]-[79]. Control of the coupled motor in Figure 7 (b) to operate as a stepper motor has also been studied in early publications [22, 80].

Despite an obvious surge in VR motor research since the early publications just mentioned, the modern literature on LVR motor position control in the context of automated manufacturing applications is scarce. An LVR motor with uncoupled phases is shown in [40], [52], [81]-[82] to perform well in high precision positioning experiments. The coupled motor has been examined in [42] (force control), [28] (dynamic simulation of position control) and [83] (excitation design for periodic motion). It has been shown in [84] to perform satisfactorily in initial experimental testing and also under additional experiments using adaptive PID sliding mode position control [85] and adaptive integral sliding mode position control [6]. Because the model of the uncoupled LVR motor is similar to that of rotary VR motors, their successful experimental application in position and speed control with automation as the ultimate target application deserves mention (see for example [86]–[88]).

The research in this dissertation is different from all literature cited in this section in a fundamental way: no published research integrates modeling, ripple-specified commutation and position control as used in this research to seek and demonstrate improved performance in point-to-point positioning and to explore the trade-offs among force ripple, settling time and average power dissipation.

1.4 Thesis Outline

The remainder of this thesis is organized as follows: Chapter 2 derives mathematical models for the LVR motors. First linear (idealized) models are derived assuming magnetic linearity and subsequent to that non-linear models are derived using finite element analysis (FEA) methods. The FEA-based model of the uncoupled motor completely characterizes the motor while the coupled motor model is limited to single-phase excitation. Chapter 3 uses motor models in conjunction with numerical optimization methods to solve two optimal commutation problems: maximization of force production and minimization of average power dissipation while producing a desired average force value. Solutions to the first problem in its most general formulation provide force-speed characterization parameterized by force ripple and also provide input (namely, available force) to models used (Chapter 4) in generating s-curve position trajectories. Solutions to the second problem in its most general formulation provide the actual current waveforms to populate look-up tables so that the currents for producing commanded forces in dynamic operation (Chapter 4) can be retrieved. Chapter 4 presents the point-to-point positioning control problem, and describes the framework that has been developed to seek and demonstrate improvement in point-to-point positioning. The development of the control system design and simulation software are described, and an assessment is presented using simulation results conducted with multiple positioning tasks. In order to reveal the trade-off between fast operation and cool operation, the comparisons of settling time results are presented

together with the associated average power dissipation. Chapter 5 summarizes the thesis and discusses opportunities for future research.

1.5 Preview of Contributions

The main contribution of this thesis is the demonstration of improvements in point-to-point positioning as measured by settling time; such improvements would benefit manufacturing automation applications that require shorter cycle times for higher throughput. A framework is developed for demonstrating the improvement and offering a prescription for finding and assessing positioning task solutions. No published research has been found that integrates the four main factors influencing point-to-point positioning: (i) actuator ripple-specified characterization and optimal static commutation, (ii) determination of feasible position trajectories based on ripple-specified optimal capability, (iii) determination of ripple-specified heat-minimizing phase currents to be recalled by the control system indexed by desired force and position, and (iv) position control design and simulation for performance assessment and comparison to predictions and for examining trade-offs. The general framework is not limited to the motors chosen in this dissertation or linear motors only. In the process of implementing this framework, the following contributions resulted:

- Analytical modeling using functional expressions for coupled (single-phase excitation) and uncoupled LVR motors from accurate numerical data
- Solutions to two optimal commutation problems, maximum force production and desired force with minimum power dissipation for idealized coupled and uncoupled LVR motors
  - Force-speed characterization parameterized by ripple
    - Expanded feasible trajectory space by matching minimum-time s-curve trajectories to ripple-based force-speed capability

  - Heat-minimizing current waveforms for desired ripple-specified average force production
  - Analysis of the internal force production mechanism of LVR motors and the influence of geometry and converter connection
  - Comparison of idealized coupled and uncoupled LVR motors in terms of their force-speed capabilities and associated performance measures

- Point-to-point position control assessment integrating optimal commutation results and digital implementation of state-space integral control

- Exploring the trade-offs among ripple, settling time and average power dissipation in the context of single-axis point-to-point positioning

CHAPTER 2

MODELING

2.1 Introduction

This chapter is concerned with the mathematical modeling of the two LVR motors shown in Figure 7 and introduced in Section 1.2.5. Mathematical models are necessary for motor characterization (to establish motor force capability) and for motor operation (to determine phase current excitation based on desired force production). First idealized modeling based on magnetic circuit analysis (MCA) is presented followed by more accurate modeling based on finite element analysis (FEA).

2.2 Idealized Models of LVR Motors

Physics-based models are derived in this section using MCA techniques. The coupled configuration relies on shared magnetic paths, whereas the uncoupled configuration consists of noninteracting magnetic paths. Both motors have concentrated coils on toothed poles on the moving assembly, and each phase winding is a series connection of the coils belonging to that phase (bearing the phase number in Figure 7). The pitch of opposing teeth is equal, so pole-to-pole offsets provide the misalignment needed to ensure controllability. Figure 10 shows the geometrical parameters referenced in the discussion.

Certain restrictions must be imposed on the arrangement of poles and teeth. Feasible pole spacings are determined by the number of teeth per pole n and the tooth pitch p_t. The pole pitch p_p, representing the distance between neighboring poles of separate phases, must satisfy

$$p_p = (m + \tfrac{1}{3})p_t \tag{17}$$

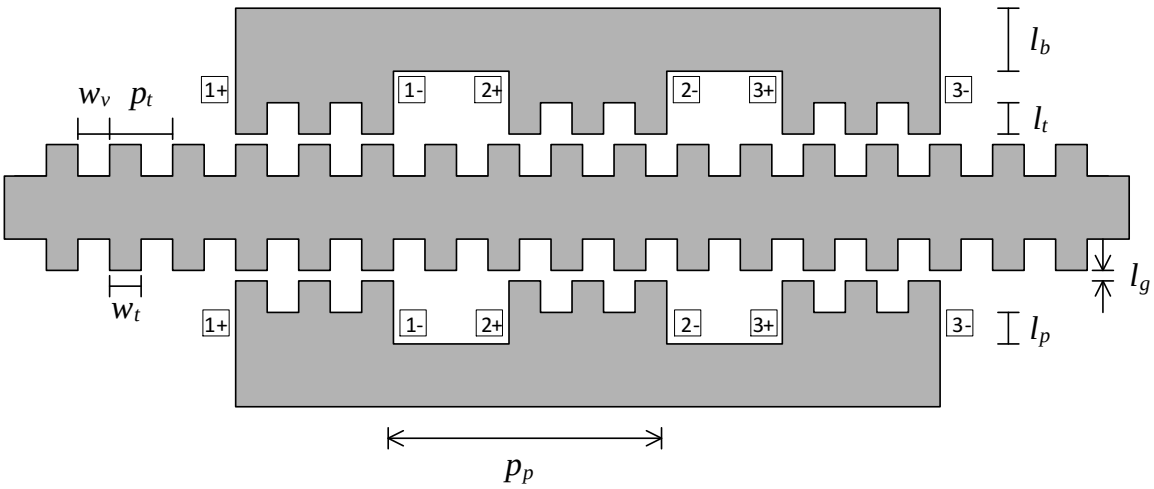

Figure 10: Geometrical parameters.

where m is an integer such that $m \geq n$; the parameter p_p applies to both coupled and uncoupled configurations. The pole pitch p'_p, representing the distance between poles of a single phase, must satisfy

$$p'_p = m' p_t \tag{18}$$

where m' is an integer such that $m' \geq n$; the parameter p'_p applies only to the uncoupled configuration. Throughout this thesis $m' = m$, since this choice minimizes the total unusable area of the coil slots.

Once the distribution of poles and teeth is established, an opportunity exists to shape the teeth. In this research, the teeth are rectangular and opposing teeth have equal width. This is the simplest choice reducing the number of studied motor designs to a manageable size while allowing the opportunity to explore the influence of geometry on force production; ultimately, the research results promote designs that would maximize force production through magnetic design (including tooth shape), optimal excitation or both. Hence, the choice of tooth shape reduces to the choice of the ratio of tooth width to tooth pitch. This ratio should be between $\frac{1}{3}$ and $\frac{1}{2}$ which

implies that the tooth width w_t and the valley width w_v must satisfy

$$w_t = p_t\ (2+\alpha)/6 \tag{19}$$

$$w_v = p_t\ (4-\alpha)/6 \tag{20}$$

where $\alpha \in [0,1]$ is a free parameter. The minimum feasible tooth width corresponds to $\alpha = 0$; any further decrease in tooth width would eliminate tooth overlap where overlap is desired. The maximum feasible tooth width corresponds to $\alpha = 1$; any further increase in tooth width would lead to tooth overlap where none is wanted. If both configurations have a common p_t, a common α, and a common depth or third dimension, then their stator bars will be identical (as in Figure 7).

2.2.1 The Fundamental Cycle of Operation

The global position variable is represented by x. Position $x = 0$ is defined here with phase 1 as reference and corresponds to the position at which the teeth on the poles of phase 1 are perfectly aligned with the stator teeth (as shown in Figure 7). At this position phase 2 and phase 3 are each at a certain offset from having the teeth on their poles at perfect alignment with stator teeth. As the translator moves (say to the left for example), the poles of phase 1 leave the perfect alignment position, pass through a position of no alignment before returning to perfect alignment again at which point a fundamental cycle of displacement equal to p_t is covered (see Figure 9 for visualization). Concurrently, the other two phases also go through one cycle in a similar fashion while at any point maintaining their offset with respect to the relative tooth orientation of phase 1. For these three-phase motors the offset is a third of the operating cycle.

From the magnetic point of view (focusing on the orientation of translator teeth with respect to stator teeth) all subsequent positions as the translator continues to move are repeats of those covered in the original cycle. Therefore, for magnetic modeling, it is only necessary to consider a set $\mathcal{X}$ of values of the relative orientation

χ_j of one phase covering one period; using phase 1, $\mathcal{X} = \{\chi_1 : 0 \leq \chi_1 \leq p_t\}$. During dynamic operation, the relative orientation χ_j of any phase can be retrieved from the global position variable x:

$$\chi_j = \begin{cases} \mathrm{mod}(x, p_t) & , j = 1 \\ \mathrm{mod}(x - \frac{1}{3}p_t, p_t) & , j = 2 \\ \mathrm{mod}(x + \frac{1}{3}p_t, p_t) & , j = 3 \end{cases} \tag{21}$$

2.2.2 Magnetic Circuit Analysis

The equivalent magnetic circuits for the coupled and uncoupled motors, constructed according to the geometry of each motor's magnetic material, are shown in Figure 11. By analyzing these equivalent magnetic circuits, it is possible to derive force models from basic design parameters. The dominant elements in the equivalent magnetic circuits are air gap permeances and mmf sources.

The air gap regions near poles of the three phases are characterized by permeances (P_1, P_2, P_3) that vary as functions of displacement x and are computed from basic design parameters using the method described in the following subsection. These permeances are periodic functions of x, with period equal to p_t and with phase-to-phase spatial shifts equal to $p_t/3$. If $x = 0$ represents a position at which the poles of phase 1 are aligned, as shown in Figure 7, these permeances may be represented in the form

$$P_j = \sum_{k=0}^{\infty} p_k \cos\left(k(\omega x - (j-1)\tfrac{2\pi}{3})\right) \tag{22}$$

where $\omega = 2\pi/p_t$. The p_k coefficients depend on air gap geometry and can be computed from derived permeance expressions using harmonic analysis. Phase currents (i_1, i_2, i_3) give rise to mmf sources (F_1, F_2, F_3) modeled by

$$F_j = N i_j \tag{23}$$

where N is the total number of turns for each series-connected phase winding. For the ideal cases under consideration, in which the magnetic material is assumed to be infinitely permeable and flux leakage is neglected, (22)–(23) completely characterize the equivalent magnetic circuits.

2.2.2.1 Air Gap Permeance

When using the equivalent magnetic circuit method, a determination is made about the probable flux paths through the magnetic material and the air gaps, and associated permenaces are computed. In the idealized modeling, the magnetic material is assumed to have infinite permeability; thus the modeling relies on air gap permeances.

The position-dependent permeances that characterize the air gap regions near poles of the three phases are computed, using the method in [21], by modeling the flux paths through the air gap regions by straight line and circular arc segments. Example flux paths for various displacements are shown in Figure 12 for two values of α. The figure shows representations of opposing teeth at different displacements and the probable flux paths, forming so-called flux tubes, at each displacement.

The permeance of each flux tube is found analytically from the parallel combination of an infinite number of differential permeances:

$$\mathsf{P}_{\text{tube}} = \mu_0 \int \frac{dA}{l} \tag{24}$$

where μ_0 is the permeability of air, l is the length of the tube and dA is the differential cross section of the tube. At any displacement, the expression in (24) must be evaluated for each distinctly shaped flux tube. The permeances of all flux tubes in the air gap region near a pole are combined in parallel to obtain a single effective permeance for that region. It is important to note that, because the LVR motors studied are double-sided, the effective permeance of a pole region at any given displacement also exists on the other side of the air gap. For the coupled motor a phase permeance consists of two permeances associated with two poles (one on each side

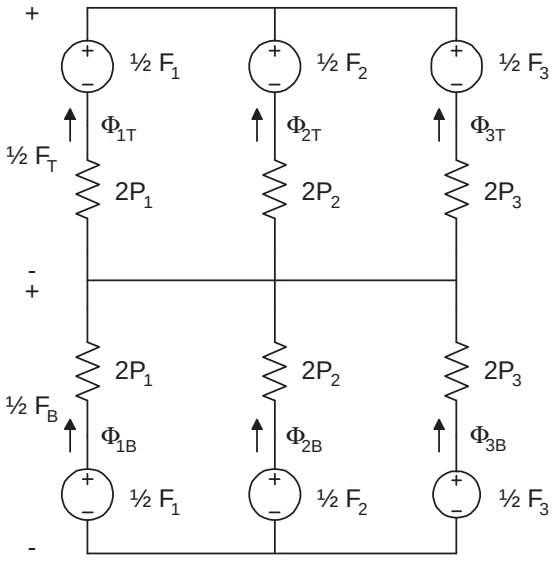

(a) Coupled configuration.

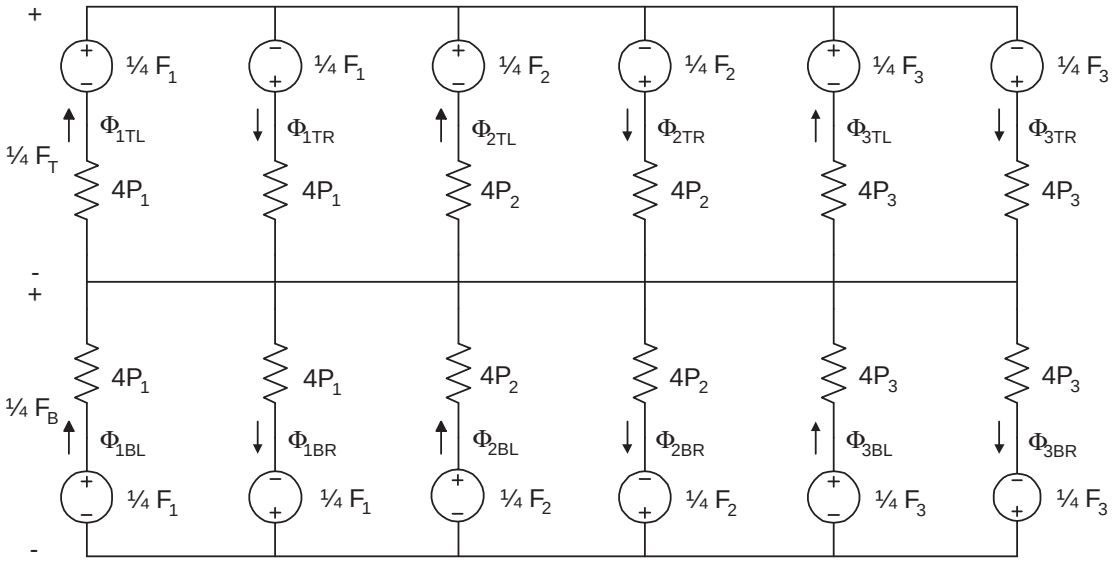

(b) Uncoupled configuration.

Figure 11: Magnetic circuit diagrams.

of the air gap), whereas for the uncoupled motor a phase permeance consists of four permeances associated with four poles (two per side).

In pursuing explicit expressions for tube permeances, it helps to identify various spatial intervals where the flux tubes maintain their shapes at any displacement within an interval. Example flux paths for several positions and the intervals to which they belong are shown in Figure 13. In this figure, tubes of the same shape share one label. Using (24), the permeances $\mathtt{P}_{\text{tube}}(x)$ of all possible tubes are found:

$$
\begin{aligned}
\mathtt{P}_1 &= \frac{\mu_0(w_t - x)d}{l_g} && , \quad 0 \le x \le w_t \\
\mathtt{P}_2 &= \frac{2}{\pi}\mu_0 d \ln\left(1 + \frac{0.5\pi x}{l_g}\right) && , \quad 0 \le x \le 0.5w_v \\
\mathtt{P}_{2'} &= \frac{2}{\pi}\mu_0 d \ln\left(1 + \frac{0.25\pi w_v}{l_g}\right) && , \quad 0.25w_v \le x \le 0.5w_t \\
\mathtt{P}_3 &= \frac{\mu_0 d}{\pi} \ln\left(1 + \frac{\pi(0.5w_v - x)}{l_g + 0.5\pi x}\right) && , \quad 0 \le x \le 0.5w_v \\
\mathtt{P}_4 &= \frac{\mu_0 dx}{l_g + 0.5\pi(w_v - x)} && , \quad 0 \le x \le 0.5w_v \\
\mathtt{P}_{4'} &= \frac{\mu_0 d(w_v - x)}{l_g + 0.5\pi(w_v - x)} && , \quad 0.5w_v \le x \le w_v \\
\mathtt{P}_{4''} &= \frac{\mu_0 d(x - w_t)}{l_g + 0.5\pi(x - w_t)} && , \quad w_t \le x \le w_v \\
\\
\mathtt{P}_5 &= \frac{2}{\pi}\mu_0 d \ln\left(\frac{l_g + 0.25\pi w_v}{l_g + 0.5\pi(w_v - x)}\right) && , \quad 0.5w_v \le x \le w_v \\
\mathtt{P}_{5'} &= \frac{2}{\pi}\mu_0 d \ln\left(\frac{l_g + 0.25\pi w_v}{l_g + 0.5\pi(x - w_t)}\right) && , \quad w_t \le x \le w_v
\end{aligned}
$$

In the expressions above, the left-hand side subscripts match the labels in Figure 13. Assume, for example, that a pole associated with phase 1 is at the displacement (and exhibits the flux tubes) shown in Figure 13 (a). The pole permeance for this displacement is then given by $\mathtt{P}_1 + 2\mathtt{P}_2 + 2\mathtt{P}_3 + \mathtt{P}_4$ and corresponds to $2P_1(x)$ for the coupled motor and $4P_1(x)$ for the uncoupled motor. The concept applies to the pole

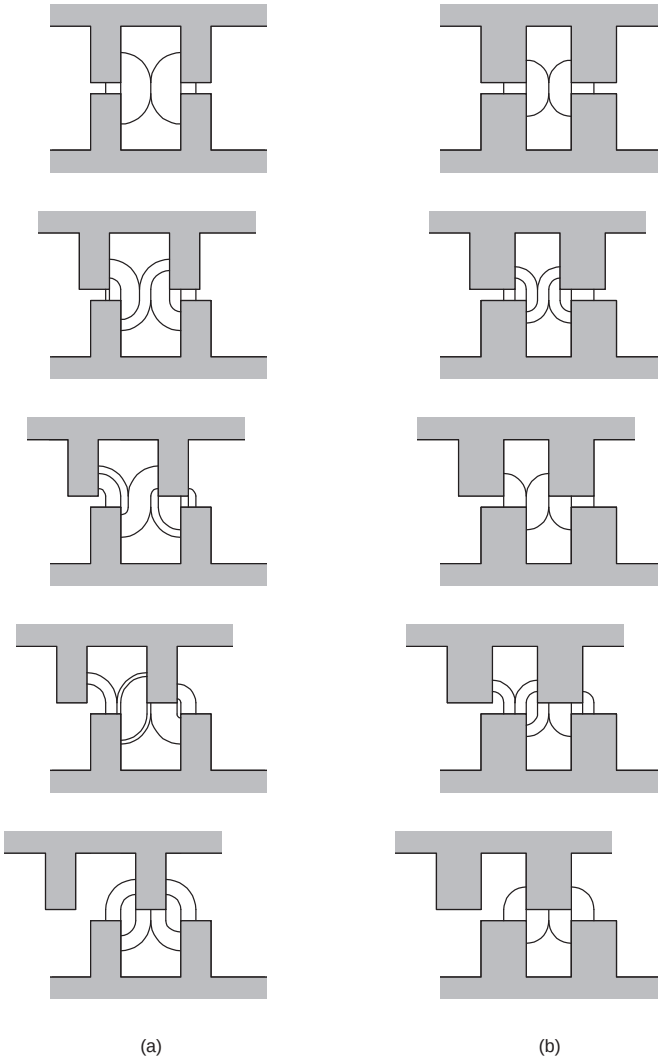

Figure 12: Flux tubes for (a) $\alpha = 0$ and (b) $\alpha = 1$.

regions in any phase; however, the appropriate tooth orientation for the poles must be carefully identified.

The piecewise continuous permeance expressions just derived (and their derivatives which can be computed directly) relate the geometric design parameters to the magnetic field computation analytically, and can provide insight into motor operation and design. Some aspects of the influence of geometry are addressed in Chapter 3.

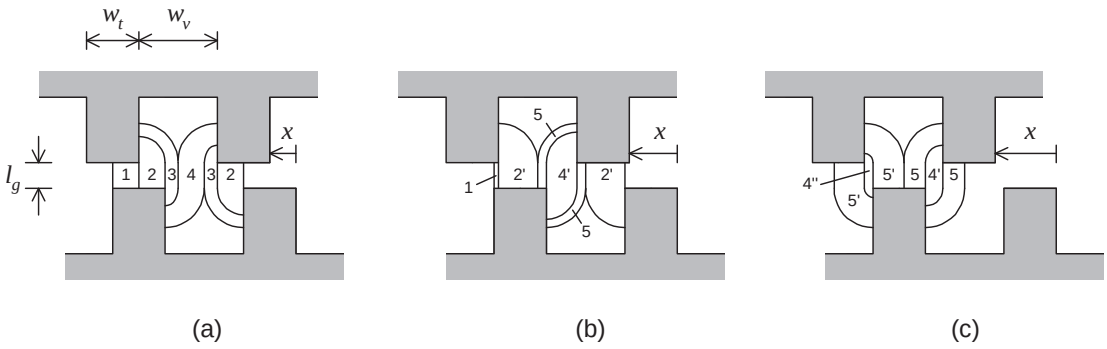

Figure 13: Assumed flux paths between toothed structures at different displacement values: (a) $0 \leq x \leq 0.5w_v$, (b) $0.5w_v \leq x \leq 0.5w_t$ and (c) $w_t \leq x \leq 0.5(w_t + w_v)$.

2.2.2.2 Pole Fluxes

Computation of pole fluxes is illustrated first for the coupled motor. The flux flowing through each air gap permeance must be the product of that permeance and the potential difference across that permeance, leading to

$$\phi_{jT} = P_j(F_j - F_T) \tag{25}$$

$$\phi_{jB} = P_j(F_j - F_B) \tag{26}$$

The fluxes entering the top and bottom nodes of the magnetic circuit must sum to zero, implying from (25) and (26) that

$$\sum_{k=1}^{3} P_k(F_k - F_T) = 0 \tag{27}$$

$$\sum_{k=1}^{3} P_k(F_k - F_B) = 0 \tag{28}$$

Solving (27) for F_T and (28) for F_B shows that the potential differences across the top and bottom portions of the magnetic circuit are identical, i.e.

$$F_T = F_B =: F_0 \tag{29}$$

where

$$F_0 = \frac{\sum_{k=1}^{3} P_k F_k}{\sum_{k=1}^{3} P_k} \tag{30}$$

Substitution of (30) into (25) and (26) shows further that the fluxes in the top and bottom portions of each pole pair are identical, i.e.

$$\phi_{jT} = \phi_{jB} =: \phi_j \tag{31}$$

where

$$\phi_j = \frac{\sum_{k=1}^{3} P_j P_k (F_j - F_k)}{\sum_{k=1}^{3} P_k} \tag{32}$$

The relationship between air gap permeance, phase current and pole flux is clearly displayed by the combination of (23) and (32).

Computation of pole fluxes for the uncoupled motor follows similar steps. The top and bottom flux expressions, which for the uncoupled motor come in a left branch and a right branch, are given by

$$\phi_{jTL} = P_j(F_j - F_T) \tag{33}$$

$$\phi_{jTR} = P_j(F_j + F_T) \tag{34}$$

$$\phi_{jBL} = P_j(F_j - F_B) \tag{35}$$

$$\phi_{jBR} = P_j(F_j + F_B) \tag{36}$$

The fluxes entering the top and bottom nodes of the magnetic circuit must sum to zero (equivalently, fluxes of the left and right branches are equal), implying from (33) – (36) that

$$\sum_{k=1}^{3} P_k(F_k - F_T) = \sum_{k=1}^{3} P_k(F_k + F_T) \tag{37}$$

$$\sum_{k=1}^{3} P_k(F_k - F_B) = \sum_{k=1}^{3} P_k(F_k + F_B) \tag{38}$$

Solving (37) for F_T and (38) for F_B shows that the potential differences across the top and bottom portions of the magnetic circuit are identical, i.e.

$$F_T = F_B =: F_0 \tag{39}$$

$$F_0 = 0 \tag{40}$$

Finally, the fluxes in the top and bottom branches of all poles of a phase are seen to be identical, i.e.

$$\phi_{jTL} = \phi_{jTR} = \phi_{jBL} = \phi_{jBR} =: \phi_j \tag{41}$$

where

$$\phi_j = F_j P_j \tag{42}$$

Again, the relationship between air gap permeance, phase current and pole flux is clearly displayed by the combination of (23) and (42).

2.2.2.3 Inductance Matrix

Models for the phase inductances are obtained by examining the relationships between phase currents and pole fluxes. Self inductances (L_{11}, L_{22}, L_{33}) and mutual inductances (L_{12}, L_{23}, L_{31}) are naturally influenced by the topologies of the equivalent magnetic circuits. If the currents, fluxes and flux linkages are denoted by vectors i, ϕ and λ, respectively, the inductance matrix L is defined by

$$\lambda = N\phi = Li \tag{43}$$

For the coupled motor, substituting (23) and (32) into (43), reveals that the self and mutual inductances are modeled by

$$L_{jj} = N^2 P_j (P_t - P_j)/P_t \tag{44}$$

$$L_{jk} = -N^2 P_j P_k / P_t \tag{45}$$

where $P_t = P_1 + P_2 + P_3$. For the uncoupled motor, substituting (23) and (42) into (43), reveals that the self and mutual inductances are modeled by

$$L_{jj} = N^2 P_j \tag{46}$$

$$L_{jk} = 0 \tag{47}$$

Note that the self and mutual inductance expressions are general expressions that hold for the basic magnetic circuit topologies under consideration; no assumptions regarding the air gap permeance model are imbedded in these expressions.

2.2.2.4 Force Model

There are two complementary ways to model force production: one emphasizing the forces due to each product of phase currents (the external viewpoint), the other emphasizing the forces developed on each pole pair (the internal viewpoint). In the first case, the force f is modeled in terms of the symmetric inductance matrix L, current vector i and position x, and is given by the quadratic function

$$f = \tfrac{1}{2} i^T \frac{dL}{dx} i \tag{48}$$

where self inductances (L_{11}, L_{22}, L_{33}) and mutual inductances (L_{12}, L_{23}, L_{31}) are modeled by (44)-(45). In the second case, which helps reveal internal LVR motor behavior (as discussed in Section 3.2.2), the individual pole forces (f_1, f_2, f_3) are modeled by

$$f_j = \tfrac{1}{2}(F_j - F_0)^2 \frac{dP_j}{dx} \tag{49}$$

where F_0 represents the potential differences across the top and bottom portions of the magnetic circuit including the mmf sources and is given by (30) for the coupled motor and by (40) for the uncoupled motor. The total force developed is thus

$$f = f_1 + f_2 + f_3 \tag{50}$$

2.2.3 Sinusoidal Characterization

The permeance model (22) accounts for spatial harmonics. However, all essential features of the air gap permeances are captured by the first two terms of this infinite series; the higher harmonics simply enhance the accuracy of the model. Hence, for clarity and insight into LVR motor operation, the previously developed model can be

specialized for sinusoidal air gap permeances and sinusoidal inductances. If higher harmonics are neglected, (22) reduces to

$$P_j = p_0 + p_1 \cos(\omega x - (j-1)\tfrac{2\pi}{3}) \tag{51}$$

and similarly sinusoidal inductances are given for the coupled motor by

$$L_{jj} = L_s + L_m \cos(\omega x - (j-1)\tfrac{2\pi}{3}) \tag{52}$$

$$L_{jk} = M_s + L_m \cos(\omega x + (j+k-2)\tfrac{2\pi}{3}) \tag{53}$$

and for the uncoupled motor by

$$L_{jk} = L_s + L_m \cos(\omega x - (j-1)\tfrac{2\pi}{3}) \tag{54}$$

$$L_{jk} = 0 \tag{55}$$

where L_s is the average self inductance, M_s is the average mutual inductance, and L_m is the variation in inductance due to air gap variation. Inductances computed with both sinusoidal and non-sinusoidal models for the motors defined in Table 1 (with $\alpha = 1$) are displayed for comparison in Figures 14–15 (coupled motor) and Figure 16 (uncoupled motor). The mutual inductances of the coupled motor are almost as large as the self inductances; all inductances include significant harmonic components. Note that only the parameters of Table 1 that define the air gap geometry (d, p_t, l_g, n and α) are needed for inductance computations.

2.2.4 Synchronous Feature of the Coupled Motor

This section provides an interpretation of the coupled motor as a classical dq transformable synchronous motor in the first approximation where higher spatial harmonics are excluded. As shown below, the specific way in which (52) and (53) depend on the coefficients L_s, M_s and L_m is significant. If one substitutes the sinusoidal inductances (52) and (53) into the force model (48), it becomes clear that phase current products are scaled by various spatially shifted sinusoidal functions of position. In order

Table 1: Parameters of Coupled and Uncoupled LVR Motors

Parameter	Symbol	Value
Device depth	d	50 mm
Tooth pitch	p_t	10 mm
Air gap length	l_g	$\frac{1}{4}$ mm
Tooth length	l_t	5 mm
Pole length	l_p	10 mm
Back iron length	l_b	15 mm
Teeth per pole	n	3
Pole pitch integer	m	4
Tooth shape factor	α	0–1
Current limit	$i_{\max}$	8.2 A
Voltage limit	$v_{\max}$	170 V, 270 V
Flux density limit	$B_{\max}$	1.0 T

to further simplify the analysis of force production, consider the position-dependent change of current variables defined by

$$\begin{bmatrix} i_1 \\ i_2 \\ i_3 \end{bmatrix} = \sqrt{\tfrac{2}{3}} \begin{bmatrix} \cos x_1 & -\sin x_1 & \frac{1}{\sqrt{2}} \\ \cos x_2 & -\sin x_2 & \frac{1}{\sqrt{2}} \\ \cos x_3 & -\sin x_3 & \frac{1}{\sqrt{2}} \end{bmatrix} \begin{bmatrix} i_d \\ i_q \\ i_0 \end{bmatrix} \tag{56}$$

$$\begin{bmatrix} i_d \\ i_q \\ i_0 \end{bmatrix} = \sqrt{\tfrac{2}{3}} \begin{bmatrix} \cos x_1 & -\sin x_1 & \frac{1}{\sqrt{2}} \\ \cos x_2 & -\sin x_2 & \frac{1}{\sqrt{2}} \\ \cos x_3 & -\sin x_3 & \frac{1}{\sqrt{2}} \end{bmatrix}^T \begin{bmatrix} i_1 \\ i_2 \\ i_3 \end{bmatrix} \tag{57}$$

where

$$x_j := \tfrac{1}{2}\omega x + (j-1)\tfrac{2\pi}{3} \tag{58}$$

The new current variables (i_d, i_q, i_0) are introduced purely for mathematical convenience; it is the original current variables (i_1, i_2, i_3) that represent the currents physically flowing in the phase windings. Substitution of (52), (53), (56) and (58) into (48), combined with trigonometric simplification, ultimately reduces (48) to the

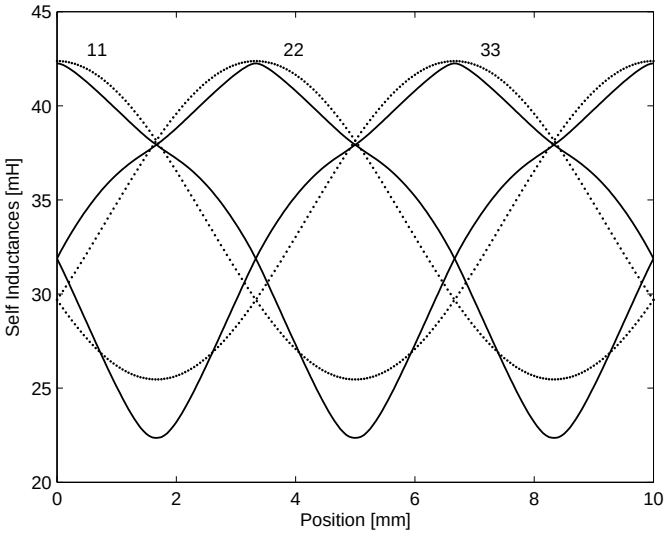

Figure 14: Self inductances and their sinusoidal approximations (coupled motor).

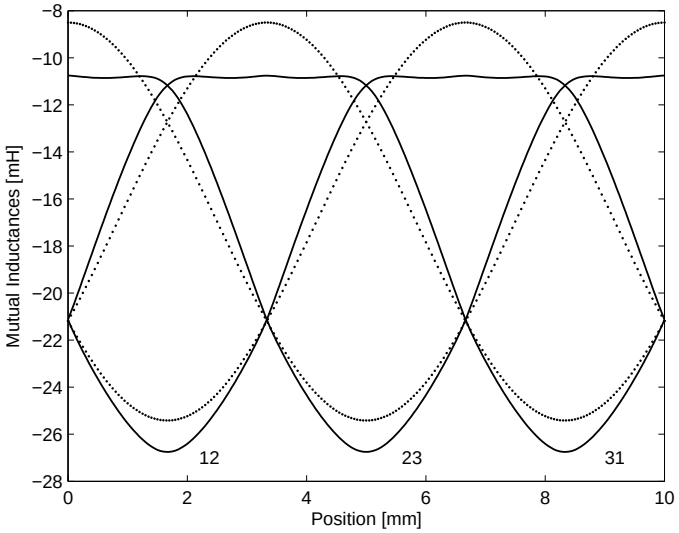

Figure 15: Mutual inductances and their sinusoidal approximations (coupled motor).

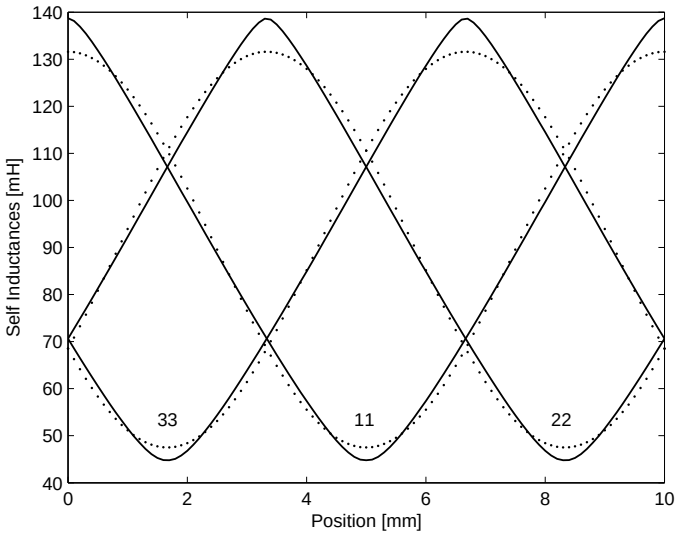

Figure 16: Self inductances and their sinusoidal approximations (uncoupled motor).

simpler form

$$f = \tfrac{1}{2}\omega(L_d - L_q)i_d i_q \tag{59}$$

where

$$L_d = L_s + M_s + \frac{3}{2}L_m \tag{60}$$

$$L_q = L_s + M_s - \frac{3}{2}L_m \tag{61}$$

or equivalently

$$L_d = \tfrac{3}{2} \text{ aligned self inductance} \tag{62}$$

$$L_q = \tfrac{3}{2} \text{ unaligned self inductance} \tag{63}$$

In the new variables, (59) indicates that force is proportional to a product of just two currents, i_d and i_q, and the scale factor is simply a constant; the dependence on position is no longer present.

The fact that the change of variables reduced (48) to (59) has a simple explanation; the self and mutual inductances (52) and (53) happen to match the inductance

characteristics of classical synchronous reluctance motors. In other words, this analysis has established that magnetically-coupled LVR motors are dq transformable, in the first approximation. This interpretation is useful and is revisited in Chapter 3.

2.2.5 Validation of MCA Models

MCA offers computational efficiency and yields analytical insight; in comparison, finite element analysis (FEA) offers accuracy but requires large computational effort and provides only numerical results. For purposes where an MCA-based model is attractive, it is worthwhile to use one that can predict critical motor characteristics with an accuracy roughly comparable to an FEA-based model.

In this section, a comparative analysis to demonstrate qualitative agreement between the MCA and the FEA models is presented using two example motors of the coupled configuration. Table 1 lists the parameters that define the geometry of the motors being investigated. MCA requires only the parameters that define the air gap geometry, whereas FEA requires all geometrical parameters (including those defining magnetic material geometry). Assuming AWG 21 wire for coils gives 200 turns per phase and a maximum phase current of about 8 A. The magnetic material is assumed to be M19 steel.

2.2.5.1 Leakage Effect

The topology of Figure 11 (a) assumes that all flux induced by a coil will cross the air gap. In reality, other so-called leakage paths for flux exist. As a first approximation, the topology can be modified to include a constant leakage permeance of $2P_l$ in parallel with each mmf source. In that case, the self inductances are modified by the addition of a leakage component

$$L_l = N^2 P_l \tag{64}$$

but the mutual inductances are unchanged. Since this modification to the inductance matrix does not depend on x, (48) shows that force production is not influenced by this leakage effect. Considering the wedge-like air regions between the poles and back iron of the E-cores, one possible approximation of leakage permeance is

$$P_l = \frac{4\mu_0}{\pi} d \tag{65}$$

where d is the depth of the motor structure.

2.2.5.2 Comparative Results

MCA has been implemented in MATLAB, using the air gap permeance model (22), the inductance model (44)–(45) and the force model (48). Leakage is introduced according to (64)–(65). FEA has been implemented in MAGNET, using a 2D magnetostatic solver and adaptive mesh refinement, yielding flux linkage and force values. Due to symmetry, only the top half of the motor and surrounding air box is included in the problem domain.

Coupled motors defined by Table 1, for the cases of minimum tooth width ($\alpha = 0$) and maximum tooth width ($\alpha = 1$) are analyzed. The analyses are restricted to the position interval $x \in [0, 5]$ mm, i.e. one-half of the tooth pitch, due to periodicity and symmetry. The reference position $x = 0$ mm is chosen to represent the aligned position for pole-pair 1; $x = 5$ mm therefore corresponds to the unaligned position for pole-pair 1. The self inductance $L_{11}(x)$ and mutual inductance $L_{23}(x)$ both possess even symmetry about $x = 0$ mm. The force $f(x)$ due to constant current in phase 1, being proportional to the spatial derivative of $L_{11}(x)$, exhibits odd symmetry about $x = 0$ mm.

Visualizations of the two motors in aligned and unaligned positions are shown in Figures 17 and 18. The upper portion of Figure 17 (the aligned case) and the lower portion of Figure 18 (the unaligned case) illustrate the logic behind the feasibility constraints (19)–(20). The minimum feasible tooth width is generated by $\alpha = 0$ since

any further decrease in tooth width would eliminate tooth overlap where overlap is desired. The maximum feasible tooth width is generated by $\alpha = 1$ since any further increase in tooth width would lead to tooth overlap where none is wanted.

The flux contours shown in Figures 17 and 18 are obtained from FEA with 1 A excitation in phase 1. Magnetic coupling between phases is clearly evident. The only difference between the two motors is the width of their teeth, yet this difference has a very significant impact on the two air gap geometries. The motor with minimum tooth width has relatively high-reluctance flux paths, and hence relatively lower levels of flux. The motor with maximum tooth width has relatively higher flux densities, and hence relatively deeper saturation of magnetic material. In the aligned position, evidence of saturation appears at 5 A for the maximum-tooth-width motor and at 7 A for the minimum-tooth-width motor.

Comparisons between MCA and FEA are shown in Figures 19–21. FEA data for L_{11} and L_{23} are generated by computing λ_1/i_1 and λ_2/i_3, respectively, using single phase excitations of 1 A. FEA data for f are generated using the Maxwell stress method. These comparisons demonstrate a qualitative agreement between the two analysis methods, at low excitation; each method indicates the same trends with respect to x and α. Strong magnetic coupling is revealed by the fact that the mutual inductances are roughly as large as the self inductances. The size of the harmonics in the spectra of the inductance-position profiles is significant; the harmonic content of the force-position profile is further amplified due to spatial differentiation.

As a function of x, self inductance modeling mismatch is in the range of 0.3–10.8% for the $\alpha = 0$ design and 0.6–4.8% for the $\alpha = 1$ design; mutual inductance modeling mismatch is in the range of 1.4–33.7% for the $\alpha = 0$ design and 0.9–16.1% for the $\alpha = 1$ design; and worst-case force modeling mismatch is 1.0 N for the $\alpha = 0$ design and 0.3 N for the $\alpha = 1$ design. For each design individually, the inductance predictions are in best agreement at positions for which more magnetic material occupies the air

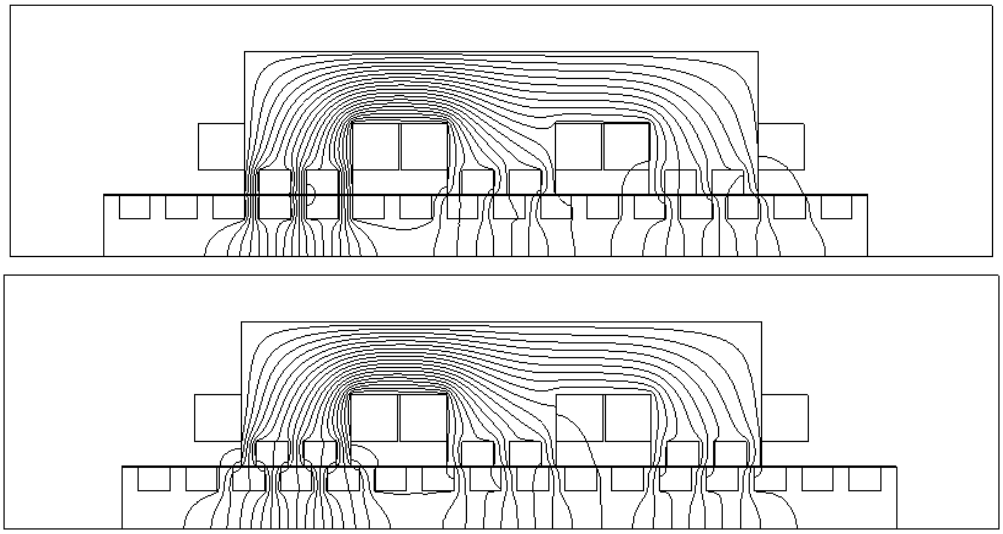

Figure 17: Flux contours for $\alpha = 0$ design: $x = 0$ and 5 mm, $i_1 = 1$ A.

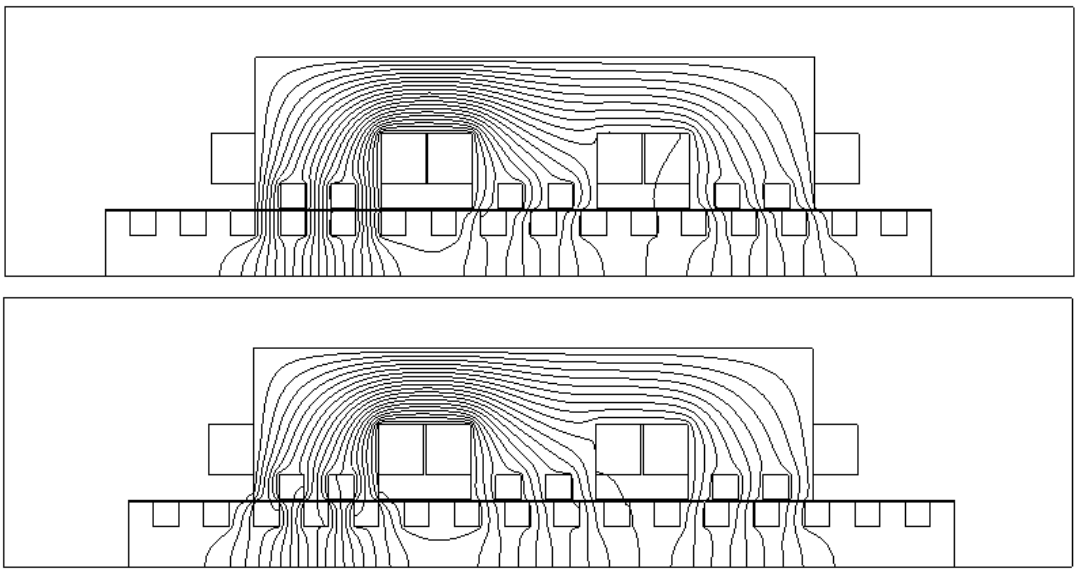

Figure 18: Flux contours for $\alpha = 1$ design: $x = 0$ and 5 mm, $i_1 = 1$ A.

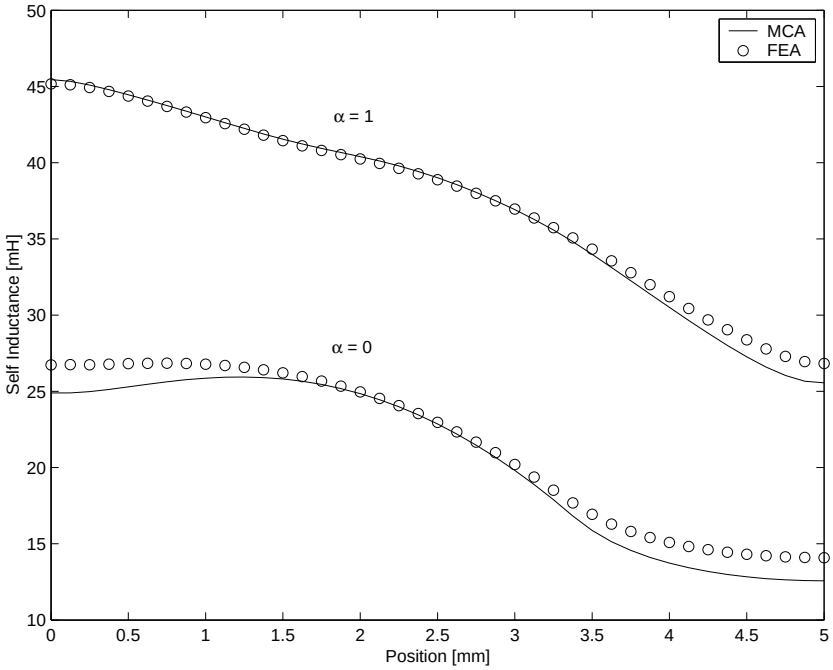

Figure 19: Self inductance $L_{11}(x)$ for $\alpha = 0$ and $\alpha = 1$ designs.

gap regions; in these positions, the flux paths are more predictable and hence are more accurately modeled by simple magnetic circuits. Since the $\alpha = 0$ design uses less magnetic material in the air gap regions than the $\alpha = 1$ design, the flux paths of the $\alpha = 0$ design are less well modeled by simple magnetic circuits than the flux paths of the $\alpha = 1$ design; this accounts for the differing levels of modeling mismatch for the two designs. Since force depends on the spatial derivative of inductance, the positions at which force modeling mismatch is large are those positions at which the inductance slopes (rather than magnitudes) exhibit large modeling mismatch.

2.3 Modeling by Finite Element Analysis and Least Squares

LVR motors exhibit complex air gap geometry and material nonlinearities, and for that reason FEA is an appealing analysis technique. In this section FEA is used to derive LVR motor models that are potentially more accurate by systematically accounting for both of these phenomena and by incorporating a novel data fitting technique.

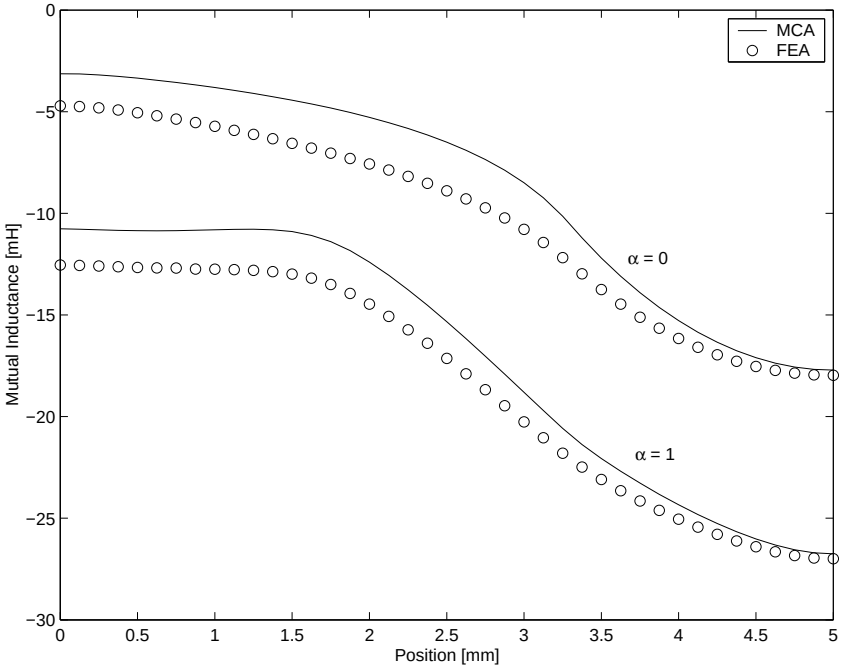

Figure 20: Mutual inductance $L_{23}(x)$ for $\alpha = 0$ and $\alpha = 1$ designs.

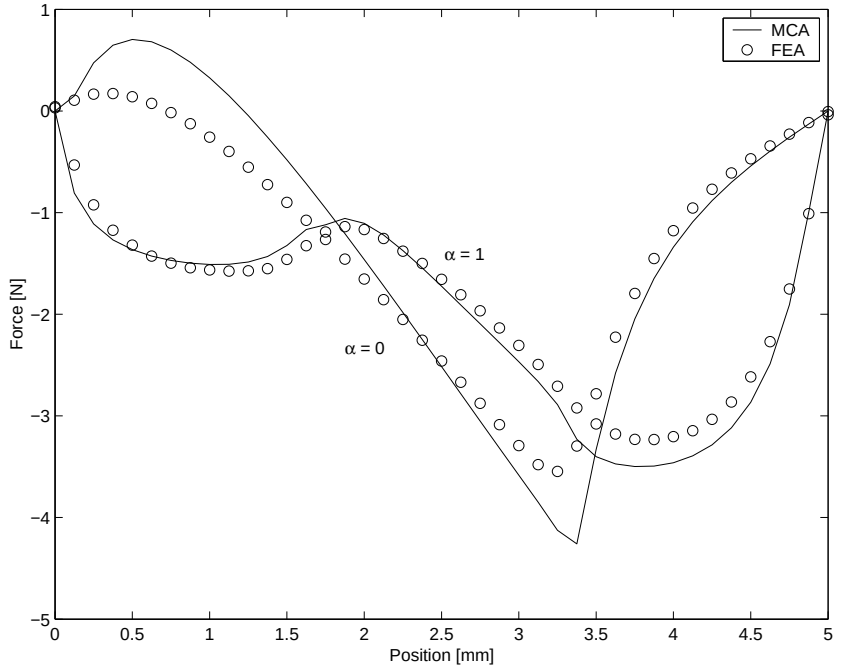

Figure 21: Force $f(x)$ for $\alpha = 0$ and $\alpha = 1$ designs with $i_1 = 1$ A.

2.3.1 Linearly Parameterized Model Formulation

In this section, an accurate data-based modeling concept is pursued. Finite element analysis is used to compute flux linkage, coenergy and force for various values of phase current and position, and least squares methods are used to fit these data to explicit mathematical expressions that account for spatial harmonics and magnetic saturation. The formulation presented here results in complete three phase characterization of the uncoupled motor. For the coupled motor, the results are restricted to single phase excitation; consideration of multiphase excitation is complicated by the presence of magnetic coupling making this problem much more difficult.

The relationship between user specifiable quantities and computed results is summarized by

$$\begin{array}{ccc} \text{Input} & \text{FEA} & \text{Output} \\ \{i_1, i_2, i_3, x\} & \Longrightarrow & \{\lambda_1, \lambda_2, \lambda_3, w, f\} \end{array} \tag{66}$$

where (i_1, i_2, i_3) are the currents, x is the position, $(\lambda_1, \lambda_2, \lambda_3)$ are the flux linkages, w is the coenergy and f is the force. The goal is to obtain a full-range FEA data set and to fit this data set to some explicit functional relationships.

For either the uncoupled motor with multiphase excitation or the coupled motor with single phase excitation, the magnetization characteristics may be modeled by functions of the form

$$\lambda(x, i) = \sum_{m=0}^{M} \sum_{n=1}^{N} c_{mn} \cos(mx^*) \tanh(ni^*) \tag{67}$$

where phase subscripts have been dropped for simplicity, the c_{mn} are coefficients to be determined, and where

$$x^* = \left(\frac{2\pi}{p_t}\right) x \tag{68}$$

$$i^* = \left(\frac{1}{i_m}\right) i \tag{69}$$

denote normalized values for position and current, where i_m is the maximum current. The cos functions capture periodicity and spatial harmonics, whereas the tanh

functions capture the magnetic saturation that occurs because of the nonlinear BH curve for steel. Note that (67) assumes even symmetry about $x = 0$, so the reference position must be chosen with this in mind.

Least squares methods will ultimately be used to assign appropriate values to the model coefficients. To emphasize the linearity of (67) with respect to these coefficients, and to prepare for compact modeling expressions, it is beneficial to introduce the vectorized version of the coefficient matrix, namely

$$C = \begin{bmatrix} c_{01} & \cdots & c_{0N} & \cdots & c_{M1} & \cdots & c_{MN} \end{bmatrix}^T \tag{70}$$

Vectorized cos and tanh functions may be similarly represented by

$$X_\lambda(x) = \begin{bmatrix} \cos(0x^*) & \cdots & \cos(Mx^*) \end{bmatrix}^T \tag{71}$$

$$I_\lambda(i) = \begin{bmatrix} \tanh(1i^*) & \cdots & \tanh(Ni^*) \end{bmatrix}^T \tag{72}$$

Using these vector notations, (67) may be equivalently expressed in the form

$$\lambda(x, i) = \Lambda(x, i)C \tag{73}$$

where

$$\Lambda(x, i) = (X_\lambda(x) \otimes I_\lambda(i))^T \tag{74}$$

and where $\otimes$ denotes the Kronecker tensor product. According to (73), flux linkage exhibits a simple linear dependence on the coefficient vector.

From a mathematical description of flux linkage, it is possible to determine other related quantities of interest. Coenergy is obtained by integrating flux linkage with respect to current. Hence, it follows that coenergy may be represented in the form

$$w(x, i) = W(x, i)C \tag{75}$$

where

$$W(x, i) = (X_w(x) \otimes I_w(i))^T \tag{76}$$

and where

$$X_w(x) = X_\lambda(x) \tag{77}$$

$$I_w(i) = i_{\mathrm{m}} \left[\begin{array}{ccc} \frac{\log(\cosh(1i^*))}{1} & \cdots & \frac{\log(\cosh(Ni^*))}{N} \end{array} \right]^T \tag{78}$$

Force is obtained by differentiating coenergy with respect to position. Hence, it follows that force may be represented in the form

$$f(x,i) = F(x,i)C \tag{79}$$

where

$$F(x,i) = (X_f(x) \otimes I_f(i))^T \tag{80}$$

and where

$$X_f(x) = -\tfrac{2\pi}{p_{\mathrm{t}}} \left[\begin{array}{ccc} 0\sin(0x^*) & \cdots & M\sin(Mx^*) \end{array} \right]^T \tag{81}$$

$$I_f(i) = I_w(i) \tag{82}$$

Expressions (75) and (79) for coenergy and force have the same structure as (73). This establishes the fact that all quantities in (66) obtained from FEA are modeled by computable functions that are linearly parameterized by a common unknown coefficient vector C.

2.3.1.1 Least Squares Data Fitting

The unknown coefficient vector C may be conveniently computed using linear least squares methods. Suppose that the user specified input data in (66) consists of several positions $\{x_1, \ldots, x_{p_x}\}$ and several currents $\{i_1, \ldots, i_{p_i}\}$. At each possible position-current pair defined by these sets, FEA is performed yielding values for flux linkage, coenergy and force denoted by $\{\lambda_{jk}, w_{jk}, f_{jk}\}$ where $j \in \{1, \ldots, p_x\}$ and $k \in \{1, \ldots, p_i\}$. These data may be manipulated as follows.

If one is primarily interested in studying flux linkage characteristics, the FEA positions and currents are used to define the constant data matrices

$$X_\lambda^{\mathrm{D}} = \begin{bmatrix} \cos(0x_1^*) & \cdots & \cos(Mx_1^*) \\ & \vdots & \\ \cos(0x_{p_x}^*) & \cdots & \cos(Mx_{p_x}^*) \end{bmatrix} \tag{83}$$

and

$$I_\lambda^{\mathrm{D}} = \begin{bmatrix} \tanh(1i_1^*) & \cdots & \tanh(Ni_1^*) \\ & \vdots & \\ \tanh(1i_{p_i}^*) & \cdots & \tanh(Ni_{p_i}^*) \end{bmatrix} \tag{84}$$

and the FEA flux linkages are placed by row order into the constant data vector

$$\lambda^{\mathrm{D}} = \begin{bmatrix} \lambda_{11} & \cdots & \lambda_{1p_i} & \cdots & \lambda_{p_x1} & \cdots & \lambda_{p_xp_i} \end{bmatrix}^T \tag{85}$$

Application of (73) on a point-by-point basis yields the linear system

$$(X_\lambda^{\mathrm{D}} \otimes I_\lambda^{\mathrm{D}})C = \lambda^{\mathrm{D}} \tag{86}$$

Assuming that the number of FEA problems p_xp_i is larger than the number of model coefficients mn, (86) is overdetermined. Solution of (86) in the least squares sense provides the coefficient vector C that minimizes the sum of the squared errors between the computed FEA data and the modeling function (67).

Since FEA provides not only flux linkage, but coenergy and force as well, it follows that one may wish to fit data to several functions in order to balance the quality of data fit over all functions of interest. To prepare for such a formulation, it is necessary to define the constant data matrices $X_w^{\mathrm{D}} = X_\lambda^{\mathrm{D}}$ and

$$I_w^{\mathrm{D}} = i_{\mathrm{m}} \begin{bmatrix} \frac{\log(\cosh(1i_1^*))}{1} & \cdots & \frac{\log(\cosh(Ni_1^*))}{N} \\ & \vdots & \\ \frac{\log(\cosh(1i_{p_i}^*))}{1} & \cdots & \frac{\log(\cosh(Ni_{p_i}^*))}{N} \end{bmatrix} \tag{87}$$

for coenergy, and

$$X_f^{\mathrm{D}} = -\tfrac{2\pi}{p_{\mathrm{t}}} \begin{bmatrix} 0\sin(0x_1^*) & \cdots & M\sin(Mx_1^*) \\ & \vdots & \\ 0\sin(0x_{p_x}^*) & \cdots & M\sin(Mx_{p_x}^*) \end{bmatrix} \tag{88}$$

and $I_f^{\mathrm{D}} = I_w^{\mathrm{D}}$ for force. The associated constant data vectors for coenergy and force are given by

$$w^{\mathrm{D}} = \begin{bmatrix} w_{11} & \cdots & w_{1p_i} & \cdots & w_{p_x1} & \cdots & w_{p_xp_i} \end{bmatrix}^T \tag{89}$$

and

$$f^{\mathrm{D}} = \begin{bmatrix} f_{11} & \cdots & f_{1p_i} & \cdots & f_{p_x1} & \cdots & f_{p_xp_i} \end{bmatrix}^T \tag{90}$$

respectively. If all FEA data are to be accounted for in the least squares fit, with equal weights assigned to all data values, then it follows from (73), (75) and (79) that

$$\begin{bmatrix} X_\lambda^{\mathrm{D}} \otimes I_\lambda^{\mathrm{D}} \\ X_w^{\mathrm{D}} \otimes I_w^{\mathrm{D}} \\ X_f^{\mathrm{D}} \otimes I_f^{\mathrm{D}} \end{bmatrix} C = \begin{bmatrix} \lambda^{\mathrm{D}} \\ w^{\mathrm{D}} \\ f^{\mathrm{D}} \end{bmatrix} \tag{91}$$

represents the complete set of simultaneous constraints on C. The linear system (91) may be solved in the sense of least squares to obtain the coefficient vector C that best fits all available data returned by the FEA solver. An obvious extension of this idea would be to introduce weights, so that different types of data, having differing magnitudes and/or differing levels of suspected accuracy, could be processed accordingly.

Solving the linear system (91) and obtaining the coefficient vector C completes single-phase excitation characterization for both motors.

2.3.1.2 Complete Three-Phase Characterization of the Uncoupled Motor

Ideally uncoupled LVR motors exhibit no magnetic coupling between phases and the uncoupled phases of the motor have identical (with phase shifting) characteristics.

Therefore, it is both sufficient and more computationally efficient to derive mathematical models for one phase using the FEA-based modeling concept developed above. The magnetic characteristics of all three phases can be constructed from the single phase results by denoting the electrical position of phase j by (21) or in compact form

$$\chi_j = \mathrm{mod}\left\{x - (j-1)\frac{p_t}{3}, p_t\right\},\ j = 1, 2, 3$$

and the current and flux linkage of phase j by i_j and λ_j.

2.3.2 Numerical Results for the Uncoupled Motor

Three uncoupled motors (distinguished by tooth width) are now considered. Table 1 provides the motor parameter values employed. The magnetic material is assumed to be M19 steel. Using AWG 21 wire, the three motors accommodate $N = 408$, 384 and 364 turns distributed over 4 poles.

FEA has been implemented in MAGNET, using a 2D magnetostatic solver and adaptive mesh refinement. For each motor, FEA solutions were obtained over 21 positions and 4 currents, for a total of 84 data sets, each containing 3 elements (flux linkage, coenergy and force). The positions considered cover only one-half tooth pitch, or 5 mm, due to symmetry. The currents considered are 2, 4, 6 and 8 A, covering the full feasible range based on current density limits and AWG 21 wire. Considering the flux linkage of phase 1 (only self magnetization characteristics of one phase are needed for the uncoupled motor), and employing the combined formulation (91) generates a total of 252 constraints. Choices of $M = 5$ and $N = 4$ for (67) were made, leading to a total of 24 model coefficients. The computed coefficient values are given in Tables 2, 3 and 4 for the $\alpha = 0$, $\alpha = 0.5$ and $\alpha = 1$ motors, respectively.

To determine the quality of fit, it is possible to compute the values of flux linkage, coenergy and force at any position and current using (73), (75) and (79), and to compare these functionally computed values to the corresponding values computed by FEA. The results of such an exercise are shown in Figure 22, where the columns

Table 2: Magnetization Parameters for Uncoupled LVR Motor with $\alpha = 0$

c_{mn}	$n = 1$	$n = 2$	$n = 3$	$n = 4$
$m = 0$	0.3106	-0.2690	0.3646	-0.1452
$m = 1$	-0.0738	-0.1002	0.3872	-0.1801
$m = 2$	0.0072	-0.1182	0.1699	-0.0654
$m = 3$	0.0473	-0.0922	0.0710	-0.0183
$m = 4$	0.0227	-0.0545	0.0509	-0.0146
$m = 5$	0.0091	-0.0197	0.0157	-0.0038

Table 3: Magnetization Parameters for Uncoupled LVR Motor with $\alpha = 0.5$

c_{mn}	$n = 1$	$n = 2$	$n = 3$	$n = 4$
$m = 0$	0.2618	-0.2037	0.3685	-0.1596
$m = 1$	-0.0703	-0.1384	0.4617	-0.2195
$m = 2$	0.0987	-0.2664	0.2746	-0.0981
$m = 3$	0.1003	-0.2300	0.2291	-0.0797
$m = 4$	0.0293	-0.0678	0.0666	-0.0230
$m = 5$	0.0035	-0.0063	0.0038	-0.0001

correspond to $\alpha = 0, 0.5$ and 1. The functionally computed values are shown as solid curves, whereas the values computed by FEA are represented by individual data points. It is clear that, over the entire current range, the models accurately capture both harmonics and saturation; saturation can be seen since, for a fixed position, the flux linkage does not scale linearly with current and the force does not scale quadratically with current over the entire current range. Examination of the force characteristics shows that for a fixed current level, both the magnitude of the peak and the position where it occurs change with tooth width.

Table 4: Magnetization Parameters for Uncoupled LVR Motor with $\alpha = 1$

c_{mn}	$n = 1$	$n = 2$	$n = 3$	$n = 4$
$m = 0$	0.2501	-0.2667	0.5492	-0.2489
$m = 1$	-0.0187	-0.2877	0.5746	-0.2469
$m = 2$	0.2583	-0.5364	0.4782	-0.1559
$m = 3$	-0.0081	-0.0008	0.0054	0.0019
$m = 4$	0.0007	0.0096	-0.0211	0.0114
$m = 5$	-0.0110	0.0148	-0.0109	0.0045

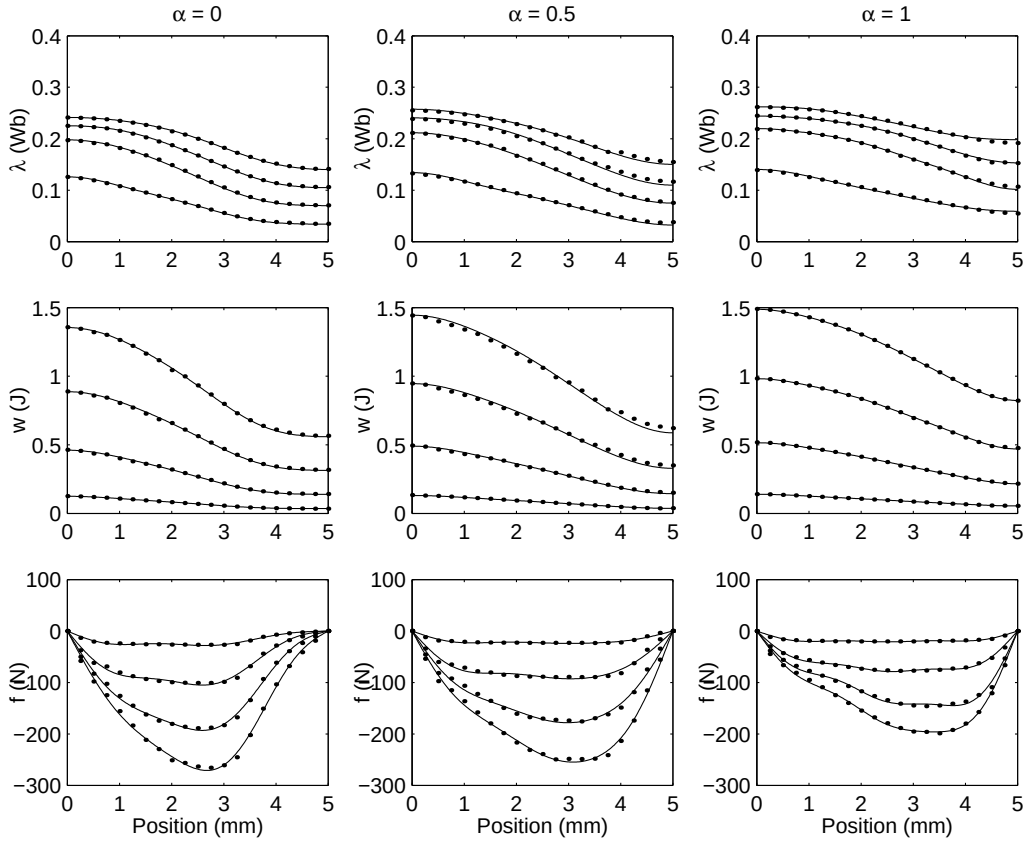

Figure 22: Magnetization characteristics of three uncoupled LVR motors with $i = 2$, 4, 6, 8 A.

2.3.3 Numerical Results for the Coupled Motor

Numerical results have been obtained for two coupled motors defined by Table 1, for the limiting cases of $\alpha = 0$ and $\alpha = 1$. The magnetic material is assumed to be M19 steel. FEA has been implemented in MAGNET, using a 2D magnetostatic solver and adaptive mesh refinement.

FEA solutions were obtained over $p_x = 21$ positions and $p_i = 4$ currents, for a total of 84 data sets, each containing 3 elements (flux linkage, coenergy and force). The positions considered cover only one-half tooth pitch, or 5 mm, due to symmetry. The currents considered are 2, 4, 6 and 8 A, covering the full feasible range based on current density limits and AWG 21 wire. In the first case, the current was i_1 and the flux linkage was λ_1; this yields the self magnetization characteristics, and the combined formulation (91) was employed to generate a total of 252 constraints. In the second case, the current was i_2 and the flux linkage was λ_3; this yields the mutual magnetization characteristics, and the reduced formulation (86) was employed to generate a total of 84 constraints. Choices of $M = 5$ and $N = 3$ for (67) were made, leading to a total of 18 model coefficients. The computed coefficient values are given in Tables 5 and 6 for the $\alpha = 0$ and $\alpha = 1$ motors, respectively.

To determine the quality of fit, values of flux linkage, coenergy and force may be functionally computed at any position and current using (73), (75) and (79) and compared to the corresponding values computed by FEA. Such a comparison is shown in Figures 23 and 24 for both motors. Figure 23 displays (self) flux linkage, coenergy and force, whereas Figure 24 displays (mutual) flux linkage. The functionally computed values are shown as solid curves, whereas the values computed by FEA are represented by individual data points. The narrow tooth cases are presented in the left columns and the wide tooth cases are presented in the right columns. In both figures, it is clear that modeling errors are sufficiently small. At low currents, the results are in agreement with those reported in Section 2.2.5. Here the high current

Table 5: Magnetization Parameters for Coupled LVR Motor with $\alpha = 0$

c^{s}_{mn}	$n=1$	$n=2$	$n=3$	c^{m}_{mn}	$n=1$	$n=2$	$n=3$
$m=0$	258.5789	-46.2327	1.6634	$m=0$	-88.1155	-22.5049	18.2914
$m=1$	-3.8173	82.9790	-36.6260	$m=1$	25.5637	53.3934	-28.8636
$m=2$	15.8024	-24.4336	7.5902	$m=2$	-0.8060	-13.0670	5.7426
$m=3$	15.1590	-24.8951	10.5166	$m=3$	-5.1115	9.2179	-3.9366
$m=4$	-9.9111	10.0770	-2.6479	$m=4$	-2.4825	4.5060	-1.5670
$m=5$	-1.1852	1.7444	-1.1874	$m=5$	-2.3866	1.7537	-0.7442

Table 6: Magnetization Parameters for Coupled LVR Motor with $\alpha = 1$

c^{s}_{mn}	$n=1$	$n=2$	$n=3$	c^{m}_{mn}	$n=1$	$n=2$	$n=3$
$m=0$	193.3332	190.5684	-95.2601	$m=0$	-98.1241	-99.3508	52.3099
$m=1$	-200.4790	326.3309	-135.1045	$m=1$	16.4158	74.9133	-37.4303
$m=2$	17.5169	-39.6764	17.5646	$m=2$	-13.6747	2.2946	-0.8235
$m=3$	-52.3673	67.1539	-24.9663	$m=3$	5.0498	-7.7662	1.7741
$m=4$	-5.6202	8.3672	-4.0503	$m=4$	-8.3591	10.0670	-4.1800
$m=5$	-2.9194	2.3266	-0.0365	$m=5$	-4.6008	8.4670	-3.9796

results are displayed as well. Magnetic saturation is apparent at the higher currents, e.g. for a fixed position the flux linkage does not scale linearly with current and the force does not scale quadratically with current, over the entire current range. The presence of spatial harmonics is also clear, at all current levels.

2.4 Conclusion

This chapter has presented linear (idealized) and non-linear modeling techniques for LVR motors. The linear models ignore magnetic material saturation and (in some cases) higher spatial harmonics. This research expands the utility of the idealized models by employing them to obtain new results, gain insight and conduct investigations with clarity. In this chapter, the (idealized modeling) analysis excluding higher spatial harmonics has established that magnetically-coupled LVR motors are dq-transformable, in the first approximation. In Chapter 3 the idealized models are used in conjunction with optimization theory and numerical techniques to explore excitation optimization without assumptions (such as made with pulsed excitation) on firing positions (when to turn a phase on or off) or the number of simultaneously

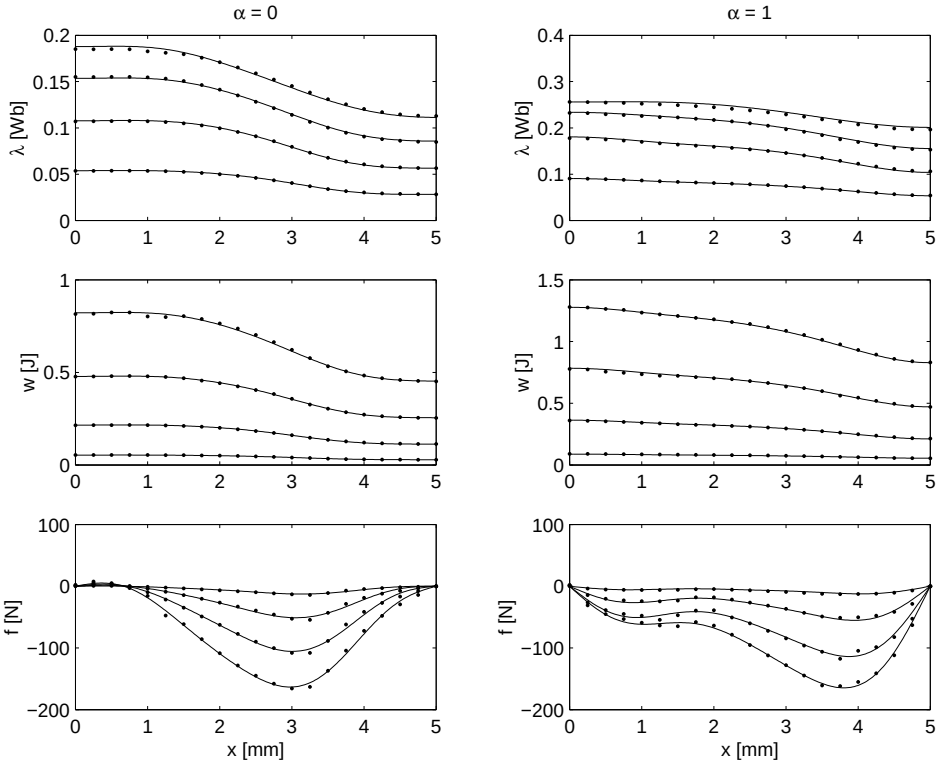

Figure 23: Self magnetization characteristics for two coupled LVR motors with excitations of $i = 2, 4, 6, 8$ A.

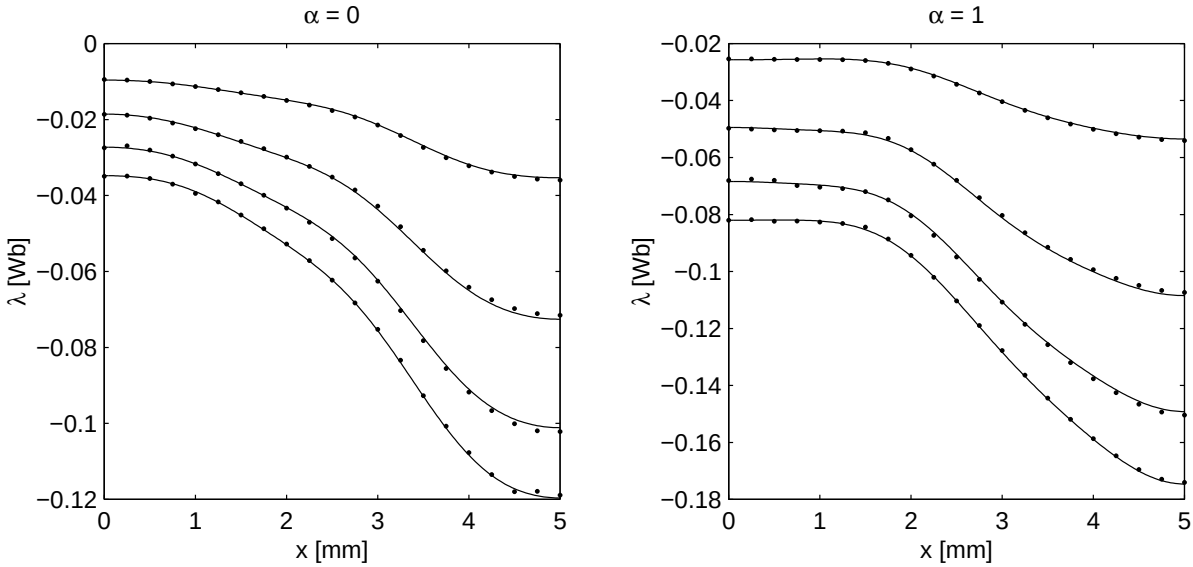

Figure 24: Mutual magnetization characteristics for two coupled LVR motors with excitations of $i = 2, 4, 6, 8$ A.

excited phases; this includes the determination of force-speed characteristics as well as the excitation currents to be recalled during the position control simulations of Chapter 4. They are also used in the design and simulation models in Chapter 4. A comparative analysis has been presented to ascertain that the MCA model can predict critical motor characteristics with an accuracy roughly comparable to an FEA-based model (at low excitation levels).

The non-linear models of LVR motors are obtained using finite element analysis and least squares. The models are simple in structure, involving cos and tanh functions in a linearly parameterized way. The model coefficients are determined from FEA data using linear least squares methods, with the option to combine mixed data types to form mixed sets of constraints so as to improve the overall quality of fit. The approach has been successfully demonstrated on three uncoupled LVR motors and two coupled LVR motors that differ with respect to tooth geometry. FEA data take time to generate, so it is customary to build up only a sparse tabular model using the combination of several values of i and x. Detailed analyses require higher resolution models, and one obvious solution would be to augment the tabular model with multilinear interpolation; with this approach, each cell in the (i, x)-plane is modeled by different functional relationships and the resulting interpolated model is not differentiable at cell boundaries. In contrast, the approach taken here results in a single smooth function, valid over the entire (i, x)-plane, for each variable of interest (i.e. λ, w and f).

The simplicity of the uncoupled motor allowed the derivation of an analytical model that completely characterizes this motor using functional expressions. This non-linear model is used in Chapter 3 to show that conclusions from commutation results are not a consequence of the magnetic linearity assumptions. Because of the complexity and computational effort, coupled motor modeling by functional expressions has been limited to the single-phase excitation case. Future attempts to extend

the approach to multiphase excitation may be to either modify the functional expressions used in data fitting or to consider the LVR motor as a type of synchronous reluctance motor and to account for the coupled-saturation effect by examining the magnetic properties of the d-axis under high excitation (adding the contributions from separately constructed single phase models is not likely to produce accurate results since superposition cannot be expected to hold within the magnetically coupled and saturating poles).

CHAPTER 3

OPTIMAL COMMUTATION

3.1 Introduction

This chapter is concerned with the optimal commutation of LVR motors. Optimal commutation refers to determining optimized current profiles for desired force production. The optimal currents are computed as phase currents versus position as opposed to time, and that is possible because the relationship between currents and force is static.

The presentation progresses from simple problem formulations to more advanced formulations that are ultimately employed in the assessment of LVR motor force-speed capability and in producing the current waveforms that would be needed during position control operations. Two optimal goals are pursued:

1. maximizing force production

2. minimizing power dissipation while producing a desired force value

In this chapter, two formulations of the position-dependent optimal commutation problems just listed are studied:

- **instantaneous-force optimal commutation** where the objective is to determine three phase currents that (i) maximize instantaneous force or (ii) minimize instantaneous power dissipation while producing a desired instantaneous force. This problem is solved *separately* for any value of the position variable x. It is possible to compute average force and average power dissipation once optimization is carried out for position values covering a spatial period of excitation

currents, but these average quantities are not part of problem formulation and do not influence optimal solutions.

- **average-force optimal commutation** where the objective is to determine the current waveforms that (i) maximize average force or (ii) minimize average power dissipation while producing a desired average force. This problem is formulated and solved *simultaneously* for (a discrete grid of) all points in a spatial period of excitation currents.

3.2 Instantaneous-Force Commutation

Instantaneous-force optimal commutation is presented first for the coupled motor starting with the simplest formulations for clarity and for insight into this motor (the coupled motor is sparsely covered in the literature). Instantaneous-force commutation of the uncoupled motor is addressed later in a comparative analysis with the coupled motor.

3.2.1 Minimum Power Dissipation without Current Limits

In this section, the optimization objective is to find, for a given position x, the phase currents that provide some given desired force with minimum power dissipation. This type of problem falls into the general category of nonlinear constrained optimization problems.

3.2.1.1 Problem Formulation

Let z be the optimization vector (the unknown to be found), $g(z)$ the objective function (the scalar function of z to be optimized) and $h(z)$ an equality constraint function. The optimization problem may be stated as follows:

$$\text{minimize} \quad g(z) \tag{92}$$

$$\text{subject to} \quad h(z) = 0 \tag{93}$$

For systematic treatment of the equality constraints, it is customary to introduce the Lagrangian

$$\mathcal{L}(z, \lambda) = g(z) + \lambda^T h(z) \tag{94}$$

The vector λ contains Lagrange multipliers. As discussed in [89], the first-order necessary conditions for this problem are

$$\nabla_z \mathcal{L}(z, \lambda) = 0 \tag{95}$$

$$\nabla_\lambda \mathcal{L}(z, \lambda) = 0 \tag{96}$$

Any solution to the constrained optimization problem (92)–(93) must be a solution of the system of simultaneous algebraic equations (95)–(96). One computational technique for solving the constrained optimization problem is thus to search for solutions to (95)–(96) using Newton's method.

3.2.1.2 Nonsinusoidal Formulation

Using force model (48), the optimization problem must be defined and solved separately for each position of interest. To fit the framework of problem (92)–(93), define

$$z := i \equiv \begin{bmatrix} i_1 & i_2 & i_3 \end{bmatrix}^T \tag{97}$$

$$g(z) := \tfrac{1}{2} i^T i \tag{98}$$

$$h(z) := \tfrac{1}{2} i^T K i - f^* \tag{99}$$

where f^* denotes the desired force and where K is shorthand notation for the inductance matrix derivative appearing in (48). The dependence of K on position is suppressed. The Lagrangian becomes

$$\mathcal{L} = \tfrac{1}{2} i^T i + \lambda \left(\tfrac{1}{2} i^T K i - f^* \right) \tag{100}$$

and hence the necessary conditions are

$$i + \lambda K i = 0 \tag{101}$$

$$\tfrac{1}{2} i^T K i - f^* = 0 \tag{102}$$

This nonlinear system of equations may be solved by Newton's method. New iterates (i^+, λ^+) are obtained from current iterates (i, λ) in recursive fashion. Each iteration involves solving the linear system

$$\begin{bmatrix} I + \lambda K & Ki \\ i^T K & 0 \end{bmatrix} \begin{bmatrix} \tilde{i} \\ \tilde{\lambda} \end{bmatrix} = \begin{bmatrix} i + \lambda K i \\ \frac{1}{2} i^T K i - f^* \end{bmatrix} \tag{103}$$

to obtain the increments $(\tilde{i}, \tilde{\lambda})$, then updating the solution estimate according to

$$\begin{bmatrix} i^+ \\ \lambda^+ \end{bmatrix} = \begin{bmatrix} i \\ \lambda \end{bmatrix} - \begin{bmatrix} \tilde{i} \\ \tilde{\lambda} \end{bmatrix} \tag{104}$$

The iteration process is terminated once the norm of the right hand side of (103) is sufficiently small.

3.2.1.3 Sinusoidal Formulation

Using force model (59), the optimization problem is defined and solved just once in a position-independent fashion. To fit the framework of problem (92)–(93), define

$$z := \begin{bmatrix} i_d & i_q \end{bmatrix}^T \tag{105}$$

$$g(z) := \tfrac{1}{2} \left(i_d^2 + i_q^2 \right) \tag{106}$$

$$h(z) := K i_d i_q - f^* \tag{107}$$

where f^* denotes the desired force and where K is shorthand notation for the constant coefficient appearing in (59). The Lagrangian becomes

$$\mathcal{L} = \tfrac{1}{2} \left(i_d^2 + i_q^2 \right) + \lambda \left(K i_d i_q - f^* \right) \tag{108}$$

and hence the necessary conditions are

$$i_d + \lambda K i_q = 0 \tag{109}$$

$$i_q + \lambda K i_d = 0 \tag{110}$$

$$K i_d i_q - f^* = 0 \tag{111}$$

In this case the nonlinear system of equations admits an explicit solution, namely

$$i_d = i^* \tag{112}$$

$$i_q = i^* \text{sign}(f^*) \tag{113}$$

where

$$i^* := \sqrt{\frac{|f^*|}{K}} \tag{114}$$

The quadratic dependence of force on current is compensated by the square root in (114).

The cost functions (98) and (106) are consistent; this is established by substituting (57) into (106) with $i_0 = 0$. Since the solution (112)–(113) is expressed in terms of transformed variables, use of (56) with $i_0 = 0$ is required for its implementation. For constant f^*, the optimal (i_d, i_q) computed by (112)–(113) will be constant and the corresponding optimal (i_1, i_2, i_3) will be sinusoidal.

3.2.1.4 Force Control Implementation

The optimization problem posed in Sections 3.2.1.2 for the non-sinusoidal case and in Section 3.2.1.3 for the sinusoidal case actually represents the force control problem. In effect these sections have formulated and solved the problem of optimal force control for the magnetically-coupled LVR motor, under the assumption that minimum copper loss is the optimization objective. The force controller, or commutator, is essentially a mapping from desired force and position to desired phase currents. The desired phase currents are used as reference commands for a current-regulated inverter. Other control objectives, such as speed control or position control, can be met by closing control loops around the commutation subsystem.

On the one hand (with sinusoidal modeling), the magnetically-coupled LVR motor is equivalent to a classical synchronous reluctance motor, despite having the features of double saliency and concentrated windings (see Section 2.2.4). This result has

conceptual value, since the classical synchronous reluctance motor is conveniently modeled using dq variables and is generally well understood. On the other hand, accurate modeling of air gap permeances has shown that the harmonic content of reluctances, inductances and inductance derivatives is too large to be ignored for many applications. For example, in the force control problem, use of sinusoidal commutation on a nonsinusoidal motor leads to significant levels of potentially undesirable force ripple. The nonsinusoidal formulation offers a force control scheme that actively compensates for spatial harmonics in order to provide smooth ripple-free force.

In both formulations, if all phase currents are multiplied by -1, the force will not be affected in any way. Furthermore, a sign change on all phase currents has no effect on power dissipation. Hence, there are two solutions to the optimization problem, corresponding to ± 1 current multipliers, due to the quadratic dependence of force on phase currents.

If all phase currents are multiplied by $\pm k$, the force magnitude will be scaled by k^2 but the force sign will remain the same. This implies that once a set of optimal phase currents is found that provides 1 N of force, the same set of phase currents may be used for all other positive force levels by simple scaling. Similarly, a set of optimal phase currents providing -1 N of force is sufficient to construct the phase currents required to reach all negative force levels. Furthermore, the optimal phase currents corresponding to positive and negative force modes are actually related to each other in a simple way. This feature suggests that a single 1D lookup table, together with some simple logic, would be sufficient to implement either (with or without harmonics) optimal commutation scheme.

3.2.1.5 Examples

The optimal commutation problem was solved for an example coupled motor defined by Table 1 (for the case of $\alpha = 1$) using force commands of $f^* = \pm 1$ N. Note that

only the parameters that define the air gap geometry are needed. Since there are two motor models, one with harmonics and one without, there are two formulations of the optimal commutation problem to consider. The results are displayed in Figures 25–26. The optimal phase currents computed for the nonsinusoidal motor are indeed perturbations of the optimal phase currents computed for the sinusoidal motor, as predicted. The optimal commutation scheme employs continuous excitation of all phases rather than some switched excitation method. Consequently, this new excitation scheme is a significant departure from earlier recommendations ([22], [80] and [25]). The period of the optimal commutation is twice that of the magnetic system, i.e. two tooth pitches. Figures 25 and 26 reveal that all phase current waveforms are derivable from just one fundamental waveform. To reverse the force direction, the indexing of current values should be reversed.

3.2.2 Coupled Motor Force Production Features

The uncoupled motor represents typical linear and rotary VR motors while the coupled motor exhibits features of both switched and synchronous varieties of variable reluctance motors. This section highlights the distinct internal force production behavior of the coupled motor, which is better visualized using the internal viewpoint of force production. Recall that there are two complementary ways to model force production: one emphasizing the forces due to each product of phase currents (the external viewpoint), the other emphasizing the forces developed on each pole pair (the internal viewpoint). In the first case, the force f is modeled in terms of the symmetric inductance matrix L, current vector i and position x, and is given by the quadratic function (48). In the second case, the force f is modeled as the sum of individual pole forces (f_1, f_2, f_3) which are given in (49); the individual pole fluxes (ϕ_1, ϕ_2, ϕ_3) are given by (32).

Numerical results have been obtained for coupled motors defined by Table 1.

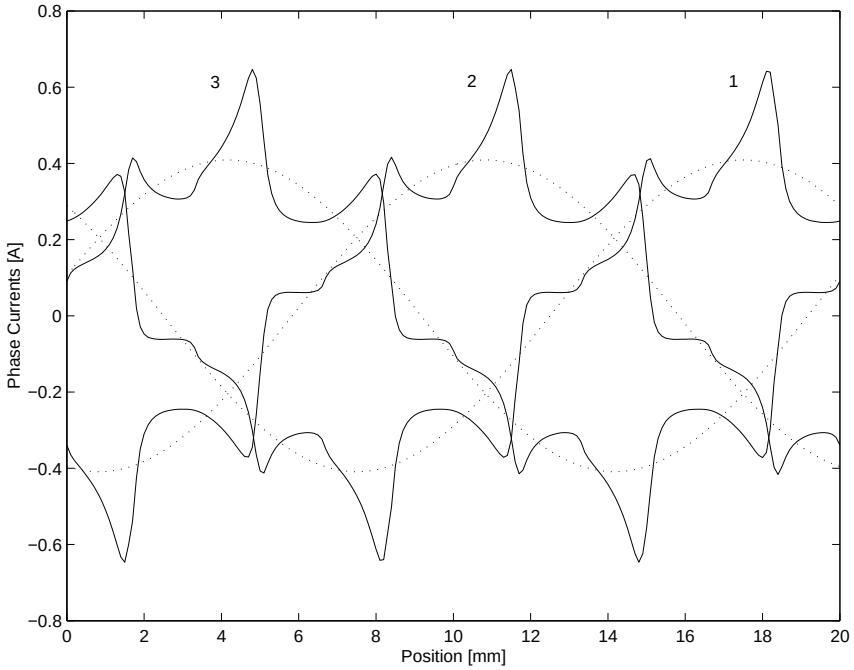

Figure 25: Optimal phase currents for both models with $f^* > 0$.

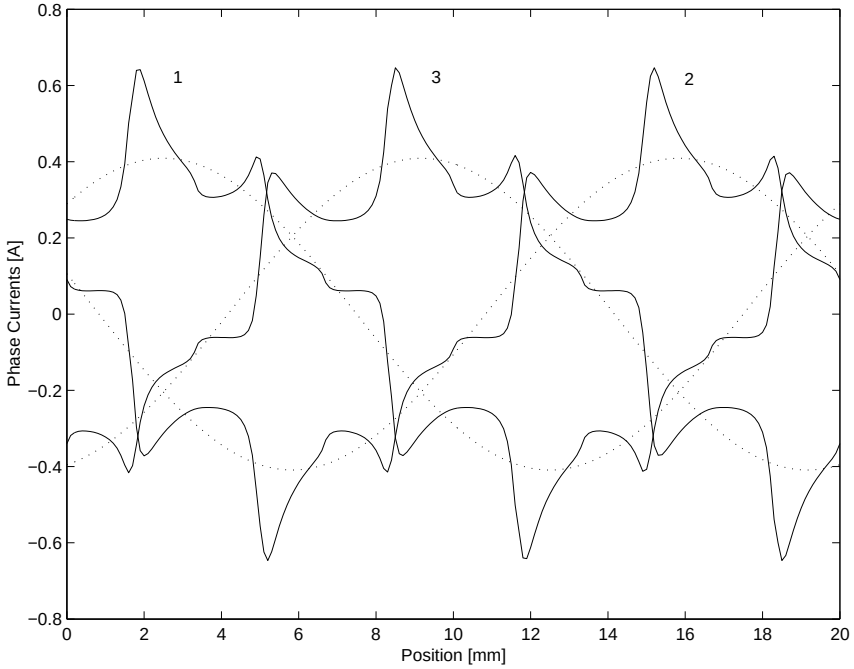

Figure 26: Optimal phase currents for both models with $f^* < 0$.

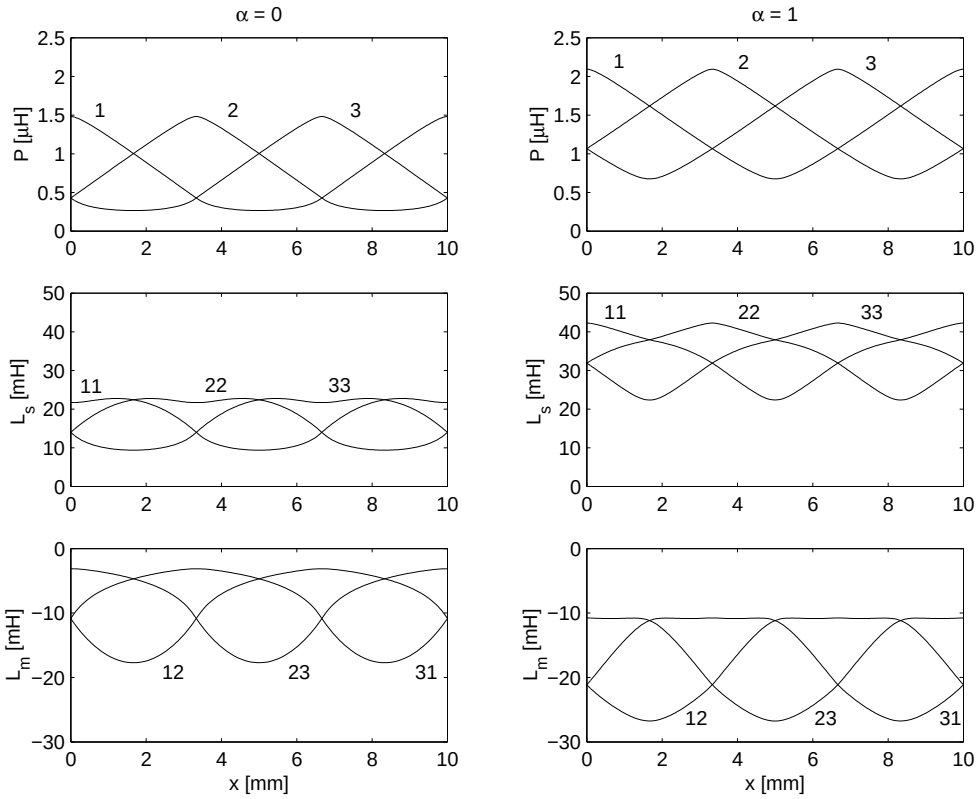

Figure 27: Air gap permeances and inductances of two coupled LVR motors ($\alpha = 0$ and 1).

Permeances and inductances are displayed in Figure 27, for the limiting cases of $\alpha = 0$ and $\alpha = 1$. Note again that all permeances and inductances include significant harmonic components, and the mutual inductances are almost as large as the self inductances.

The optimal excitation problem was solved for the example motors of Table 1 with $\alpha = 0$ and $\alpha = 1$, using force commands of $f^* = \pm 1$ N. The results are displayed in Figures 28 and 29; the columns correspond to values of α, whereas the rows correspond to phase currents, pole fluxes and pole forces. One distinction from the uncoupled (switched) motor is immediately observed: this force control scheme employs continuous excitation of all phases rather than some switched excitation method (early publications report switched excitation for the coupled motor).

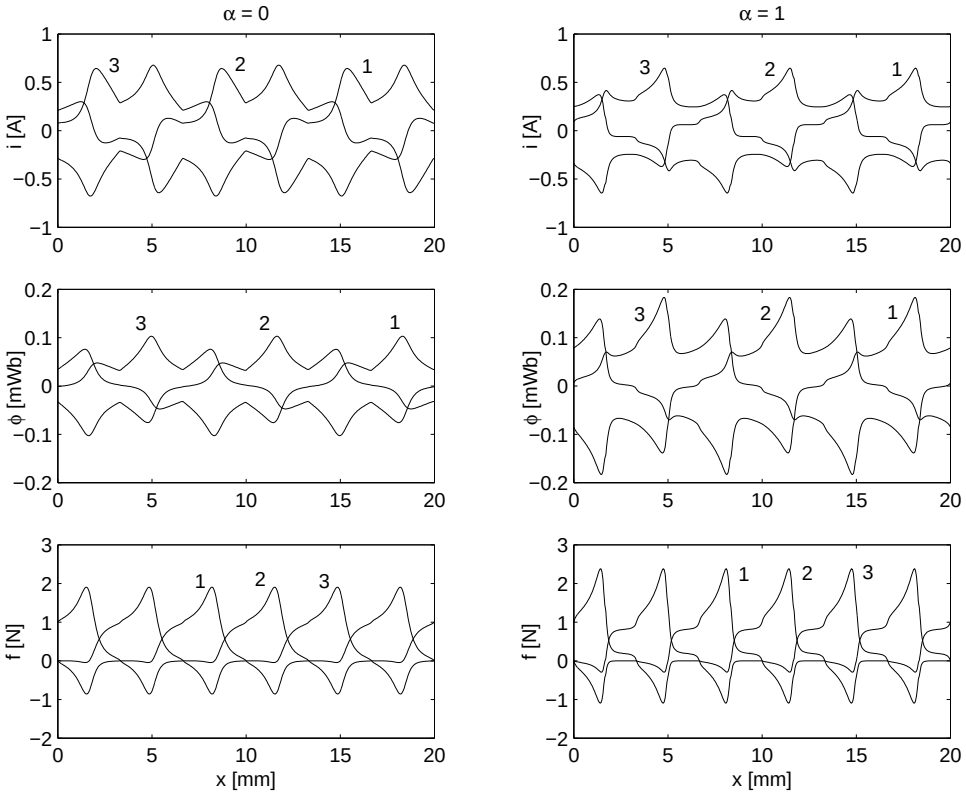

Figure 28: Phase currents, pole fluxes and pole forces of two LVR motors ($\alpha = 0$ and 1) for +1 N force.

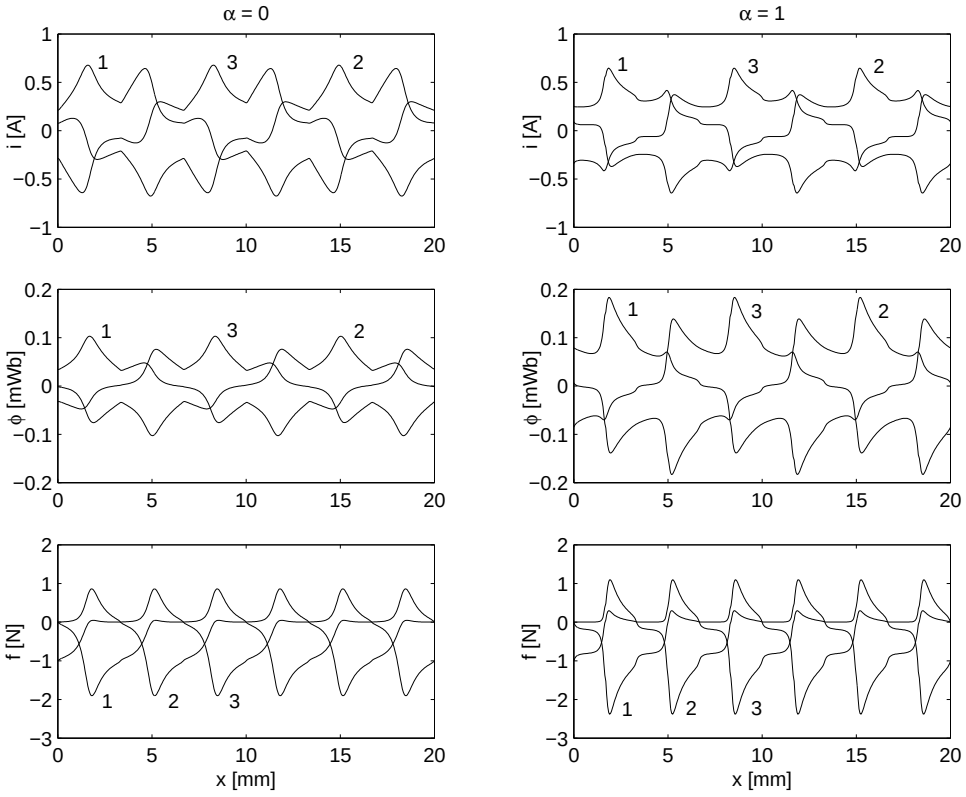

Figure 29: Phase currents, pole fluxes and pole forces of two coupled LVR motors ($\alpha = 0$ and 1) for -1 N force.

Figures 28 and 29 reveal the internal behavior of the optimally excited motors. Increasing position in these figures corresponds to leftward motion of the E-cores in Figure 7 (a). The period of the phase currents and pole fluxes is twice that of the magnetic system, i.e. two tooth pitches, whereas the period of the pole forces is just one tooth pitch since these forces do not depend on the direction of flux. The phase currents and pole fluxes are perturbations of the sinusoidal currents and fluxes that provide maximum force/ampere when spatial harmonics are neglected in the motor model. The high harmonic content in the air gap permeances and winding inductances of Figure 27 gives rise to high harmonic content in the phase currents and pole fluxes. The phase currents and pole fluxes each sum up to zero, even for the realistic case when spatial harmonics are not neglected. The pole forces change signs every one-half tooth pitch since (49) implies that

$$\text{sign}\{f_j\} = \text{sign}\left\{\frac{dP_j}{dx}\right\} \tag{115}$$

The particular interval over which a given pole force is positive or negative can be predicted exclusively from the spatial derivative of the corresponding air gap permeance shown in Figure 27. The pole forces are attractive rather than repulsive, and thus it is impossible to have all three poles contributing force of the desired polarity at all times. Depending on position, there will be either one or two poles that contribute force of the desired polarity and the remaining pole(s) will generate an opposing force. For this reason, the peak values of pole forces must exceed the commanded force value. Intervals exist over which a given pole flux is nearly zero, and (49) may be manipulated to show that the corresponding pole force will likewise be nearly zero over this same interval. However, the phase currents are never identically zero over position intervals as in the case of switched excitation strategies. This feature of continuous excitation has not been imposed *a priori*, but is a consequence of the optimization. The pole forces sum up to equal the commanded force of ± 1 N, as expected.

3.2.2.1 Influence of Air Gap Geometry

Figures 28 and 29 also illustrate the influence of motor design parameters on the optimal excitation scheme (in this case the α parameter which sets the air gap geometry). The impact of α can be seen by comparing the two columns of these figures. For example, the shape of the phase currents is somewhat different for the two cases, and the peak-to-peak variation of pole fluxes and pole forces is larger for $\alpha = 1$ than for $\alpha = 0$. Since α clearly has an influence on the optimization results, it is logical to consider additional design questions. Which value of α yields the smallest value of power dissipation for the same force command, and which value of α provides the largest value of smooth ripple-free force when current limits are imposed? These questions are explored in Table 7.

For values of α ranging from 0 to 1 in 0.1 increments, both energy dissipation values and maximum force values are reported in Table 7. The energy dissipation values correspond to one period of the excitation waveforms for a ± 1 N force command (computed after the optimal currents have been computed for x values covering one such period); energy over one period is likely more relevant than instantaneous power at specific positions. Since both force and power are quadratic functions of current, the dissipation values reported in the table are sufficient to cover other force commands as well; e.g. the tabulated dissipation values should be multiplied by 10 for a ± 10 N force command. The trend with respect to α is essentially monotonic, and the lowest dissipation value corresponds to $\alpha = 1$. The maximum force values represent the largest force command magnitudes that satisfy the thermal phase current magnitude limit of 8 A (checked after the currents have been computed). In this case, the trend with respect to α is not monotonic, and for α between 0.7 and 1.0 a high parametric sensitivity is apparent. Such high sensitivity is simply a consequence of the shape change in phase currents, in particular the peaking of phase currents,

Table 7: Energy Dissipation and Maximum Force Versus Tooth Shape

α	E_{period} [mJ] for $f^* = \pm 1$ N	$\lvert f \rvert_{\max}$ [N] for $\lvert i \rvert_{\max} = 8$ A
0.0	12.5	139
0.1	11.7	140
0.2	11.1	142
0.3	10.5	143
0.4	10.1	143
0.5	9.7	141
0.6	9.5	138
0.7	9.3	132
0.8	9.3	122
0.9	9.3	114
1.0	9.2	152

as α varies. It is quite interesting to note that the $\alpha = 1$ design, as shown in Figure 7 (a), rates higher than the other members of this design family as far as both energy dissipation and smooth force limit are concerned. It is important to further investigate and verify, using experimental or detailed finite-element-based analysis, all trends and phenomena observed under idealized modeling but in particular changes such as seen between $\alpha = 0.9$ and $\alpha = 1.0$, where the maximum ripple-free force goes from a minimum to maximum value.

3.2.3 Instantaneous-Force Commutation with Current Limits

This section addresses current limited maximization of force and minimization of power dissipation of the coupled LVR motor. Constrained optimization is used below for two purposes: first, to determine the motor's continuous force limit corresponding to some given continuous current limit; second, to determine currents that satisfy the current limits and produce a desired force with minimum power dissipation. The roles of tooth geometry and the connection between motor and inverter are also examined.

3.2.3.1 Problem Formulation

To accommodate constraints, such as an upper limit on some function of the optimization vector, the problem statement in (92)–(93) must be modified; for example

adding one inequality constraint function $c(z)$ gives

$$\begin{aligned} \text{minimize} \quad & g(z) && (116) \\ \text{subject to} \quad & h(z) = 0 && (117) \\ & c(z) \leq 0 && (118) \end{aligned}$$

With the addition of not one but three inequality constraints on phase currents (more constraints in later sections), the complexity of the optimization problems increases and so does the ability to track problem solutions analytically. Formulating necessary conditions for optimality, such as (95)–(96) in the previous subsection, and iteratively solving them for each optimization problem studied, despite its appeal, becomes impractical. A more practical and efficient alternative is to use a commercially available software (in this case the MATLAB Optimization Toolbox [90]) with the ability to define and solve constrained and unconstrained optimization problems of various types such as linear, quadratic or nonlinear programming and general nonlinear constrained optimization. This change is reflected in subsequent problem formulation; programming details that are left out in this document (for maximum clarity) can be found in [90] (such details include proper syntax, writing and calling function files, choosing solution algorithms and adjusting tolerances and parameters that control algorithm execution).

As before let z and g be respectively the optimization vector and the objective function. The equality and inequality constraints are modified to reflect multiple constraint functions and are represented, respectively, by h_p ($p \in \mathcal{P}$) and c_q ($q \in \mathcal{Q}$) where p, q represent function indices and $\mathcal{P}$, $\mathcal{Q}$ represent sets of indices. For example, if there is no equality constraint function in an optimization problem then $\mathcal{P} = \{\phi\}$ or if there are two inequality constraint functions then $\mathcal{Q} = \{1, 2\}$. The general

optimization problem statement is as follows:

$$\begin{aligned} \text{minimize} \quad & g(z) && (119)\\ \text{subject to} \quad & h_p(z) = 0,\ p \in \mathcal{P} && (120)\\ & c_q(z) \leq 0,\ q \in \mathcal{Q} && (121) \end{aligned}$$

Obviously, the objective of maximizing some function $g(z)$ is translated into minimizing $-g(z)$ to fit this general framework.

3.2.3.2 Maximum Instantaneous Force

The first optimization problem considered is the problem of finding magnitude constrained currents that maximize the magnitude of force produced at any given position. For a 3-wire connection between motor and inverter, this problem is stated as

$$\begin{aligned} \text{maximize} \quad & \pm\tfrac{1}{2} i^T \frac{dL}{dx} i && (122)\\ \text{subject to} \quad & |i_j| - i_{\max} \leq 0,\ j = 1,2,3 && (123)\\ & i_1 + i_2 + i_3 = 0 && (124) \end{aligned}$$

For a 6-wire connection between motor and inverter, the problem is restated in the form

$$\begin{aligned} \text{maximize} \quad & \pm\tfrac{1}{2} i^T \frac{dL}{dx} i && (125)\\ \text{subject to} \quad & |i_j| - i_{\max} \leq 0,\ j = 1,2,3 && (126) \end{aligned}$$

to reflect the removal of the equality constraint on current. In both cases, the sign of the objective function is chosen to match the desired force sign. These problems fit

the general framework (119)–(121) where

$$z := i \equiv \begin{bmatrix} i_1 & i_2 & i_3 \end{bmatrix}^T \tag{127}$$

$$g(z) := \mp\tfrac{1}{2} i^T \frac{dL}{dx} i \tag{128}$$

$$h_1(z) := i_1 + i_2 + i_3, \text{ only for the 3-wire connection case} \tag{129}$$

$$c_{1,2,3}(z) := |i_j| - i_{\max},\ j = 1, 2, 3 \tag{130}$$

Here the sets of constraint function indices are $\mathcal{P} = \{1\}$ for a 3-wire connection and $\mathcal{P} = \{\phi\}$ for a 6-wire connection and $\mathcal{Q} = \{1,2,3\}$.

The solutions to these optimization problems have applications in bang-bang control, but they also serve to provide the continuous force limit corresponding to a given continuous current limit. The achievable range of ripple-free force is determined by minimizing the maximum force magnitudes over x.

3.2.3.3 Minimum Instantaneous Power Dissipation

The second optimization problem considered is the problem of finding magnitude-constrained currents that produce a given desired force at a given position and that further minimize the power dissipated in the winding resistances. For a 3-wire connection between motor and inverter, this problem is stated as

$$\text{minimize} \quad i^T i \tag{131}$$

$$\text{subject to} \quad \tfrac{1}{2} i^T \frac{dL}{dx} i - f^* = 0 \tag{132}$$

$$|i_j| - i_{\max} \leq 0,\ j = 1, 2, 3 \tag{133}$$

$$i_1 + i_2 + i_3 = 0 \tag{134}$$

For a 6-wire connection between motor and inverter, the problem is restated in the form

$$\begin{aligned} \text{minimize} \quad & i^T i && (135) \\ \text{subject to} \quad & \tfrac{1}{2} i^T \frac{dL}{dx} i - f^* = 0 && (136) \\ & |i_j| - i_{\max} \leq 0, \ j = 1, 2, 3 && (137) \end{aligned}$$

to reflect the removal of the equality constraint on current. In both cases, f^* denotes the desired force (positive or negative). These problems fit the general framework (119)–(121) where

$$\begin{aligned} z &:= i \equiv \begin{bmatrix} i_1 & i_2 & i_3 \end{bmatrix}^T && (138) \\ g(z) &:= i^T i && (139) \\ h_1(z) &:= i_1 + i_2 + i_3, \text{ only for the 3-wire connection case} && (140) \\ c_{1,2,3}(z) &:= |i_j| - i_{\max}, \ j = 1, 2, 3 && (141) \end{aligned}$$

The solutions to these optimization problems find applications in force control, speed control and position control. These optimization problems are solvable if and only if the magnitude of f^* is within the limits identified by the solution of the corresponding maximum force control problem.

3.2.3.4 Numerical Results

Numerical results have been obtained for the motors defined by Table 1 with $\alpha = 1$ (only the parameters that define the air gap geometry and the current limit are used). Air gap permeance computation is explained in Section2.2.2.1, the magnetic material is assumed to be infinitely permeable and flux leakage is neglected. Numerical optimization was performed using the function `fmincon` of the MATLAB Optimization Toolbox [90]. This function finds the constrained minimum of a scalar function of several variables starting at an initial estimate. This type of procedure is generally referred to as constrained nonlinear optimization or nonlinear programming.

The maximum force control problem (for positive force) is first explored for the classical case of sinusoidal magnetics, i.e. the spatial harmonics of inductance are temporarily neglected. For this special case, the solutions are shown separately in Figures 30 and 31 for 3-wire and 6-wire connections, respectively. In both cases, the optimal current profiles are trapezoidal and the resulting maximized force varies sinusoidally about a maximized average value. At every position, the maximized force for the 6-wire connection exceeds the maximized force for the 3-wire connection. A ripple-free force limit can be defined by taking the minimum (over position) of the maximized force values. With this definition, use of the 6-wire connection augments the range of ripple-free force by 33%. Figure 32 provides further explanation of the superiority of the 6-wire connection over the 3-wire connection. At this x the optimal currents are $i_3 = -8$ A with (i_1, i_2) equal to $(8, 8)$ A and $(4, 4)$ A for the 6-wire and 3-wire connections, respectively. All values of (i_1, i_2) with magnitudes bounded by 8 A are feasible with the 6-wire connection, whereas only values along the dashed line are feasible with the 3-wire connection. Figure 33 shows the ripple-free force limit with inductance harmonics included, for various values of the tooth shape parameter. The 6-wire connection outperforms the 3-wire connection, and the wide-tooth design outperforms all other feasible choices of tooth shape.

The minimum-copper-loss force control problem has also been solved separately for the 3-wire and 6-wire connections. The optimal excitation currents corresponding to the largest admissible (positive) force command are displayed for the 3-wire and 6-wire connections in Figures 34 and 35, respectively. In the 3-wire case, the force command cannot exceed the critical value at which the excitation currents first reach their saturation limits; once one current saturates, the other two currents are completely determined by the force and current equality constraints. In the 6-wire case, larger force commands are possible since more freedom exists to increase non-saturated currents during intervals on which one current is saturated. For the wide-tooth design,

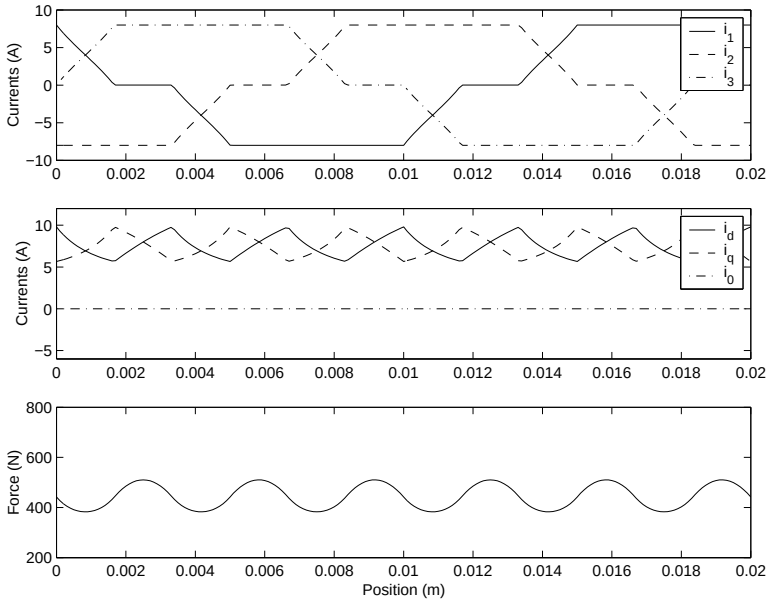

Figure 30: Force maximizing currents and resulting force for 3-wire connection of $\alpha = 1$ motor (excluding spatial harmonics).

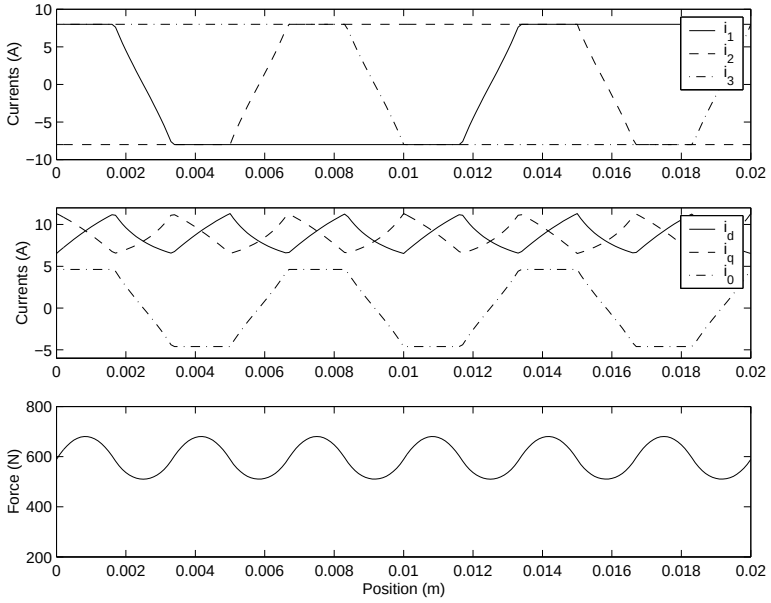

Figure 31: Force maximizing currents and resulting force for 6-wire connection of $\alpha = 1$ motor (excluding spatial harmonics).

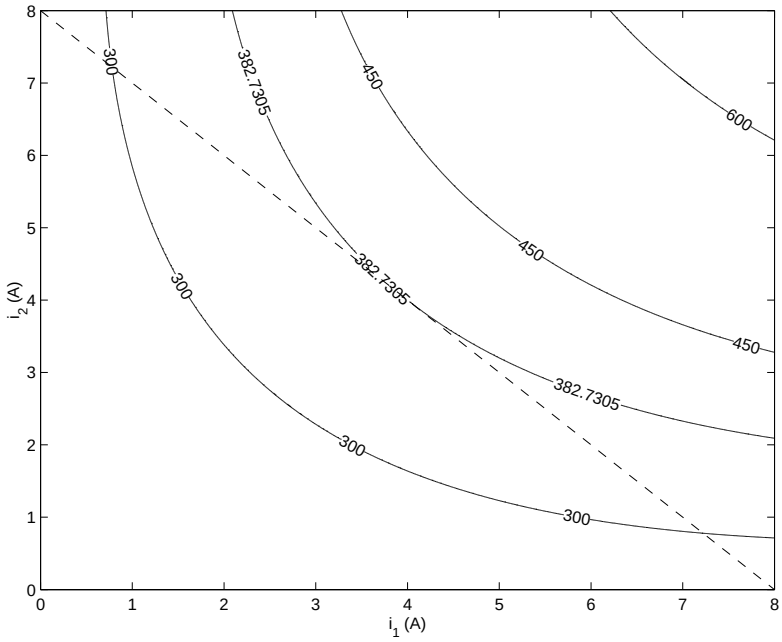

Figure 32: Force contours in (i_1, i_2) plane with $i_3 = -8$ A at $x = \frac{17}{12}p_t \approx 14$ mm of $\alpha = 1$ motor (excluding spatial harmonics).

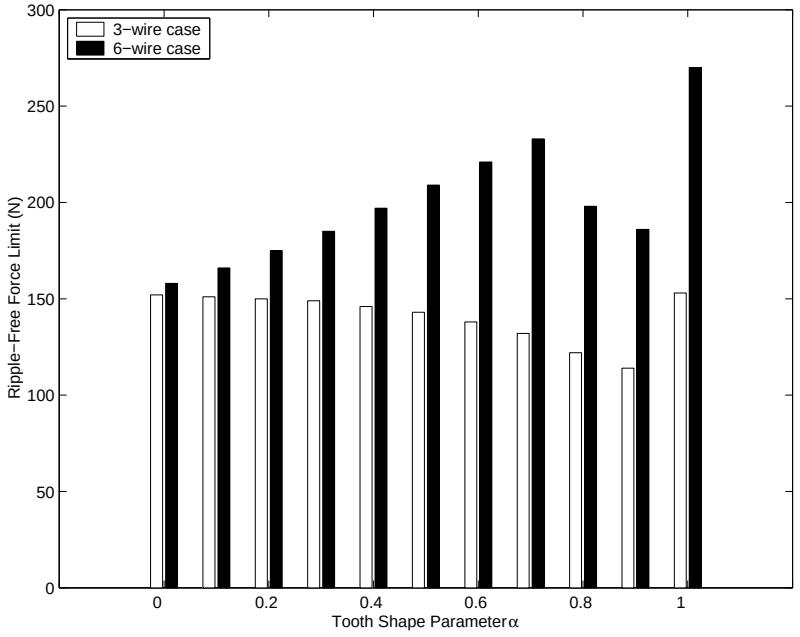

Figure 33: Ripple-free force limits (min over x of max f) versus α for 3-wire and 6-wire connections (including spatial harmonics).

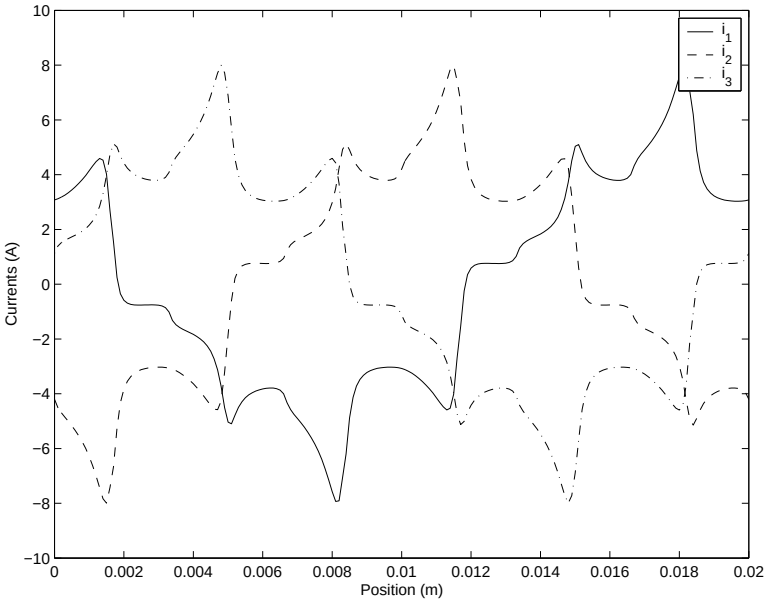

Figure 34: Currents for maximum ripple-free force (153 N) for 3-wire connection of $\alpha = 1$ motor (including spatial harmonics).

the 6-wire connection outperforms the 3-wire connection—in regards to ripple-free force range—by 76%.

3.2.4 Acceleration Capability of LVR Motors

This section expands on the instantaneous-force optimal commutation results of the previous sections in two major ways. First, the uncoupled motor is now included and compared to the coupled motor. Second, constrained optimization methods are used to investigate the acceleration capabilities of both magnetic configurations. The specific measure of performance emphasized here is the ratio of current-limited ripple-free force to moving mass or, equivalently, the maximum achievable fully controllable acceleration (the maximum average force available for accelerating a load is considered later). This focus is motivated by the robotic applications targeted in this research, e.g. component placement machines used in electronics assembly.

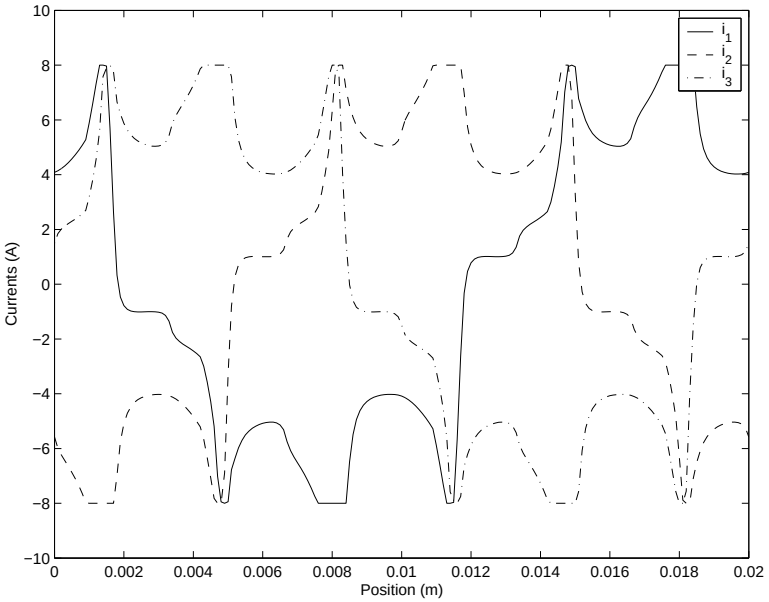

Figure 35: Currents for maximum ripple-free force (270 N) for 6-wire connection of $\alpha = 1$ motor (including spatial harmonics).

3.2.4.1 Force Limits

To determine force limits, the force maximization problem is solved. Based on the results of the previous section, a 6-wire connection between motor and inverter is assumed. Therefore, for each x, the ultimate force limits are found by solving the constrained optimization problems (125)–(126).

For the coupled motor, (125)–(126) is a quadratic programming problem with variables i_j and constraints $i_j \in [-i_{\max}, i_{\max}]$ for $j = 1, 2, 3$. For the uncoupled motor, (125)–(126) is a linear programming problem with variables i_j^2 and constraints $i_j^2 \in [0, i_{\max}^2]$ for $j = 1, 2, 3$. Solutions (f^*, i^*) to these quadratic and linear programming problems may be computed using the functions `quadprog` and `linprog` of the MATLAB Optimization Toolbox [90]. From these solutions, the following force limits

may be determined:

$$\hat{f}^* = \text{maximum } \{f^* : x \in [0, X]\} \tag{142}$$

$$\bar{f}^* = \text{average } \{f^* : x \in [0, X]\} \tag{143}$$

$$\check{f}^* = \text{minimum } \{f^* : x \in [0, X]\} \tag{144}$$

The spatial period of the excitation currents, X, is equal to $2p_t$ for coupled motors and p_t for uncoupled motors. These force limits quantify the force production capabilities of any given motor. Note that $\check{f}^*$ represents the ripple-free force limit.

3.2.4.2 Minimum Instantaneous Power Dissipation

Consider now the problem of finding magnitude-constrained currents that produce a given desired force and that further minimize the power dissipated in the winding resistances. For each position x and each desired force f^d satisfying $|f^d| \leq f_{\max}$, this problem takes the form (135)–(137), where the limits $f_{\max}$ and $i_{\max}$ are interrelated to ensure feasibility.

For coupled motors, (135)–(137) is a nonlinear programming problem with variables i_j and constraints $i_j \in [-i_{\max}, i_{\max}]$ for $j = 1, 2, 3$. For uncoupled motors, (135)–(137) is a linear programming problem with variables i_j^2 and constraints $i_j^2 \in [0, i_{\max}^2]$ for $j = 1, 2, 3$. These problems may be solved using either `fmincon` (for coupled motors) or `linprog` (for uncoupled motors) from the MATLAB Optimization Toolbox [90].

The problem statement (135)–(137) explicitly accounts for current limits. Suppose instead that current limits are implicitly accounted for as follows. For each x and each f^d satisfying $|f^d| \leq \tilde{f}_{\max}$, the problem

$$\text{minimize} \quad i^T i \tag{145}$$

$$\text{subject to} \quad \tfrac{1}{2} i^T \frac{dL}{dx} i = f^d \tag{146}$$

is solved to obtain the solution i^*, and this solution is subsequently magnitude-limited according to

$$\tilde{i}_j^* = \begin{cases} i_{\max} & , \; i_j^* > i_{\max} \\ i_j^* & , \; i_j^* \in [i_{\min}, i_{\max}] \\ i_{\min} & , \; i_j^* < i_{\min} \end{cases} \tag{147}$$

for $j = 1, 2, 3$ where $i_{\min} = -i_{\max}$ for coupled motors and $i_{\min} = 0$ for uncoupled motors. The limits $\tilde{f}_{\max}$ and $i_{\max}$ must be interrelated to ensure feasibility in the following sense: problem (145)–(146) always admits a solution i^* for arbitrarily large $\tilde{f}_{\max}$, but the magnitude-limited version of this solution $\tilde{i}^*$ does not provide the desired result $f = f^d$ unless $\tilde{i}^* = i^*$, and this latter condition is satisfied only if $\tilde{f}_{\max}$ is set small enough (in relation to $i_{\max}$) to ensure that current saturation does not occur.

The force limits identified in this section are related by

$$\tilde{f}_{\max} < f_{\max} = \check{f}^* < \bar{f}^* < \hat{f}^* \tag{148}$$

Each of these force limits may be symbolically obtained for the special case of sinusoidal inductance. For the coupled motor, sinusoidal inductance requires sinusoidal air gap reluctance. For the uncoupled motor, sinusoidal inductance requires sinusoidal air gap permeance. Although neither the reluctance nor the permeance can be expected to be truly sinusoidal, the assumption of sinusoidal inductance leads to the simplest possible models capturing all essential features of coupled and uncoupled motors. Each force limit may be expressed in the form

$$f_{\text{limit}} = k \Delta L \frac{\pi}{p_t} i_{\max}^2 \tag{149}$$

where ΔL denotes the magnitude of sinusoidal inductance variation and k is a constant of proportionality. Values of k are listed in Table 8. The benefit in using (135)–(137) instead of (145)–(147) is a boost in the ripple-free force range of 33% for coupled motors and 73% for uncoupled motors.

Table 8: Force Limit Parameters for Sinusoidal Magnetics

Limit	k_c	k_u
$\tilde{f}_{\max}$	$\frac{9}{8}$	$\frac{1}{4}$
$\check{f}^*$	$\frac{3}{2}$	$\frac{\sqrt{3}}{4}$
$\bar{f}^*$	$\frac{7}{4}$	$\frac{3}{2\pi}$
$\hat{f}^*$	2	$\frac{1}{2}$

3.2.4.3 Numerical Results

This section describes performance limits computed for coupled and uncoupled motors similar to those depicted in Figure 7. The numerical case study is organized on the basis of a family of closely related motors, half being coupled and half being uncoupled. Every motor considered has certain dimensions in common. The common dimensions which influence the magnetic circuit parameters are device depth, tooth pitch and air gap length. The common dimensions which influence only the moving mass are tooth length, pole length and back iron length. The motors are distinguished from one another by choices of the following variable parameters: n, m, α and N. The wire gauge, and hence the current limit, remains the same in all cases.

Table 9 provides the actual parameter values employed. Note that there are 20 motors in total, defined by permutations of magnetic configuration, n and α: 5 coupled motors with narrow teeth; 5 coupled motors with wide teeth; 5 uncoupled motors with narrow teeth; and 5 uncoupled motors with wide teeth. The 10 motors with narrow teeth run on a common narrow-tooth stator bar, whereas the 10 motors with wide teeth run on a common wide-tooth stator bar. The current limit was determined by the selection of AWG 21 wire, a 50% packing factor and a maximum current density of 20 A/mm^2.

As illustrations of (135)–(137), consider two motors, one coupled and one uncoupled, described by Table 9 with the choices $n = 3$, $m = 4$ and $\alpha = 1$. The coupled motor accommodates $N = 224$ turns distributed over 2 poles, whereas the uncoupled

Table 9: Parameters of 20 Coupled and Uncoupled LVR Motors

Parameter	Symbol	Value
Device depth	d	50 mm
Tooth pitch	p_t	10 mm
Air gap length	l_g	$\frac{1}{4}$ mm
Tooth length	l_t	5 mm
Pole length	l_p	10 mm
Back iron length	l_b	15 mm
Teeth per pole	n	2, 3, 4, 5, 6
Pole pitch integer	m	3, 4, 5, 6, 7
Tooth shape factor	α	0, 1
Turns per phase	N	224, 244, 364, 408
Current limit	$i_{\max}$	8.2 A

motor accommodates $N = 364$ turns distributed over 4 poles. The inductances and some representative optimal currents for these two motors are shown in Figures 36 and 37. The coupled motor operates at its ripple-free force limit $\check{f}_c^* = 357$ N under synchronous excitation with period $2p_t$, whereas the uncoupled motor operates at its ripple-free force limit $\check{f}_u^* = 700$ N under switched excitation with period p_t.

Figure 38 displays some typical comparative results relating to force-mass ratio, for the entire family of 20 motors. Each data point in the force-mass plane summarizes the ripple-free force limit of the motor and identifies its moving mass. The dashed lines identify groups of motors that differ only with respect to n; as expected, both force and mass increase with n. The influence of α is as follows: for the coupled motor, the wide tooth version exhibits both larger force and larger mass; for the uncoupled motor, the narrow tooth version exhibits the larger force and the wide tooth version exhibits the larger mass. For any fixed values of n and α, the uncoupled motor exhibits larger force and mass in comparison with the coupled motor.

Figure 38 may also be interpreted as a selection criterion for motors within this motor family. For example, if the given application requires a small ripple-free force

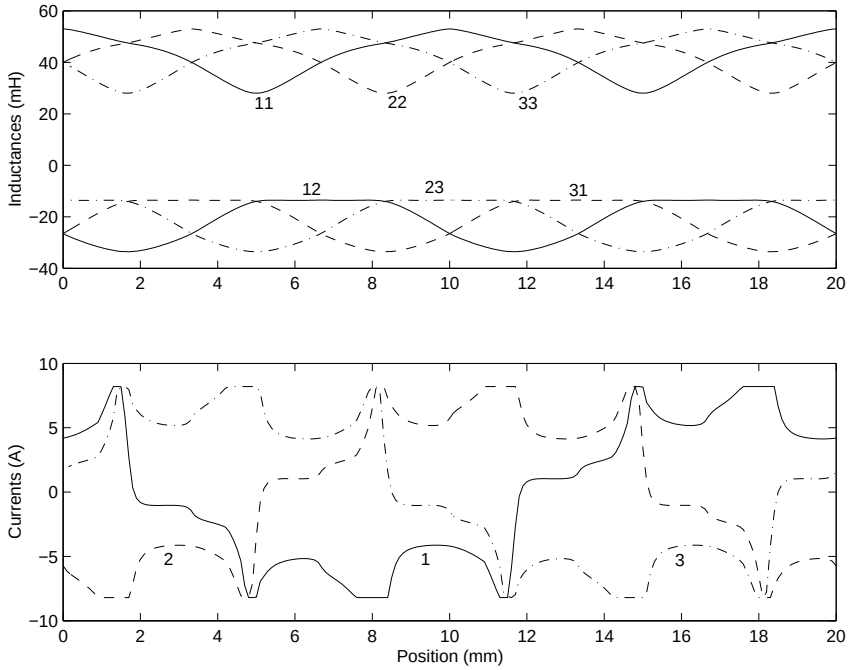

Figure 36: Inductances and optimal currents, coupled motor.

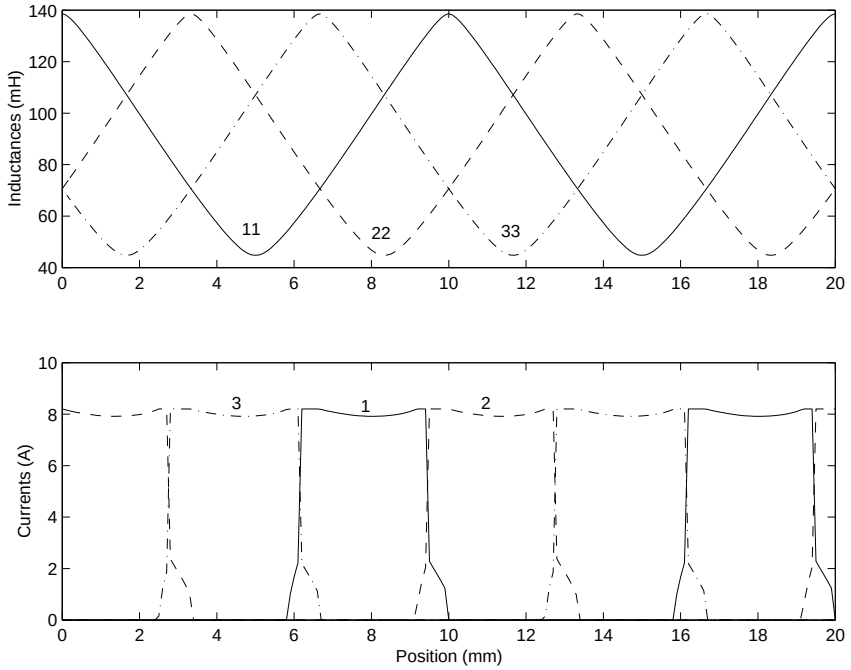

Figure 37: Inductances and optimal currents, uncoupled motor.

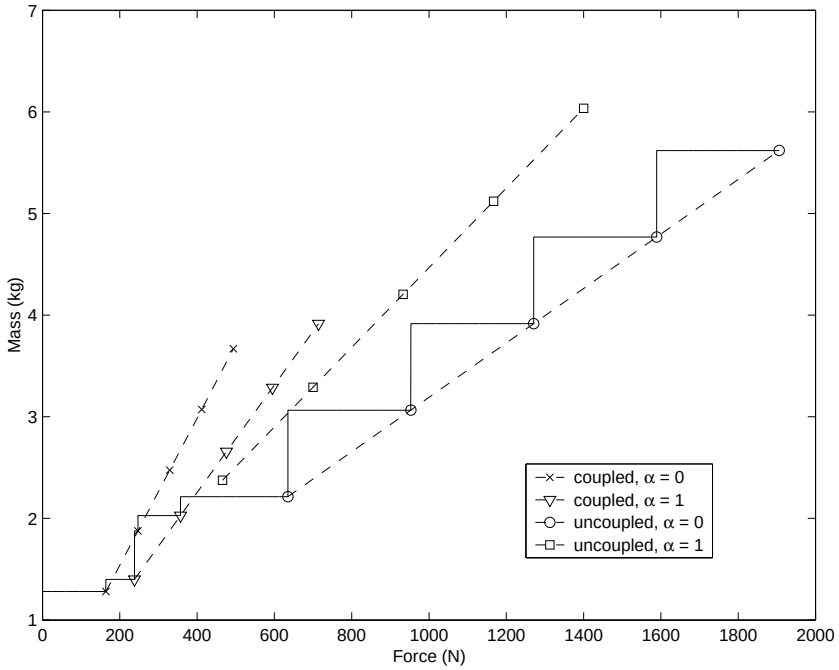

Figure 38: Mass versus force for the various designs.

limit no larger than 164 N, then the most suitable motor would be the coupled motor with $n = 2$ and $\alpha = 0$ since this is the lowest mass motor that can provide the desired force. If the force requirement is between 164 N and 238 N, then the most suitable motor would be the coupled motor with $n = 2$ and $\alpha = 1$. Continuing in this fashion, it becomes clear that one of the coupled motors will be preferred for all sufficiently small force requirements. However, at some critical force level, which turns out to be 357 N in this study, this selection method begins to prefer uncoupled motors over coupled motors. Moreover, the uncoupled motors with $\alpha = 0$ will always be preferred in the large force ranges exceeding 357 N since, for any fixed n, they provide the lower mass and higher force. This selection strategy is illustrated in the figure by the solid line, which identifies the lowest mass motor from within this motor family that is capable of producing any given ripple-free force level.

3.3 Average-Force Commutation

In the introduction to this chapter it has been mentioned that two formulations of optimal commutation are studied: instantaneous-force commutation and average-force commutation. In the most general formulation of instantaneous optimal commutation (Section 3.2.4), constrained optimization methods are used to determine optimal excitations that would (i) maximize instantaneous force or (ii) minimize instantaneous power dissipation while producing a desired instantaneous force. The optimizations are performed only at zero speed with constraints only on instantaneous current. The optimization problems are solved separately for each position of interest, each time returning a vector i of three numbers representing three phase currents. It is possible to compute average force and average power dissipation once optimization is carried out for position values covering a spatial period of excitation currents, but these average quantities are not part of problem formulation and do not influence optimal solutions.

This section is concerned with average-force optimal commutation where the objective is to determine the current waveforms that (i) maximize average force or (ii) minimize average power dissipation while producing a desired average force. As will become apparent in the remainder of this dissertation, consideration of average force changes not only the optimization formulation (optimization vector and constraint functions) but also the nature of the results and their application potential. Solving the first optimization problem provides force limits (force-speed characterization) which can be used in evaluating LVR motor positioning capability, whereas solving the second optimization problem provides the actual current waveforms to populate lookup tables for retrieval during dynamic simulation of positioning tasks. The optimization problems are solved simultaneously for all points in a spatial period of operation; voltage constraints are included and the solutions are obtained over a range of speed values thus facilitating force-speed characterization of the LVR motors.

The concept of force ripple is introduced and used in expanding the results to obtain ripple-parameterized force-speed characterization facilitating positioning capability evaluation based on the amount of force ripple allowed in commutation design. With the inclusion of force ripple control, the average-force optimal commutation comes in two formulations:

- Average-force optimal commutation without ripple specification (the variation of instantaneous force about the average value of force is not controlled)
- Average-force optimal commutation with ripple specification (the variation of instantaneous force about the average value of force is controlled)

3.3.1 Average-Force Commutation without Ripple Specification

Solutions to the two average-force optimal commutation problems are now pursued so as to produce optimal excitation currents that (i) maximize average force or (ii) minimize average power dissipation while producing a desired average force, but at this point no attempt is made to control the size of ripple in the force waveforms associated with these optimal excitation currents. First equations for average force, average power dissipation, voltage and flux density are given and then problem formulation is addressed to explain the distinctive features of the problems considered.

3.3.1.1 Average Force

The electromagnetic force of VR motors is a function of the phase currents and the translator position as can be seen from the analysis of Chapter 2. Unlike brushless dc motors, for example, VR motors do not have a force constant that makes it possible to determine the force at any translator position under a fixed current excitation (when the current flowing through one phase of a VR motor is kept constant over a spatial period of operation the force generated is not constant over that period). The waveform in Figure 39 depicts generically a maximized force waveform (motor excited

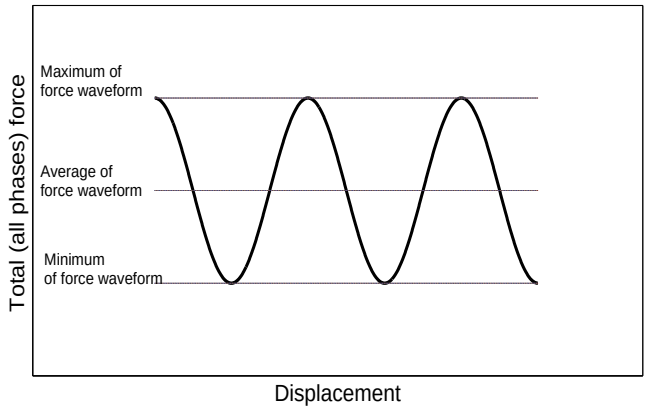

Figure 39: Illustration of VR motor force variation about an average maximal value.

to produce maximum force at all displacements). This waveform exhibits significant force ripple; in other words, the instantaneous value of force varies significantly from the average value. Over a spatial period X of excitation currents, equal to $2p_t$ for coupled motors and p_t for uncoupled motors, the average value of force is given by

$$f_{\text{avg}} = \frac{1}{X} \int_0^X f(x, i)\ dx \tag{150}$$

where $f(x, i)$ has been defined by (48), using the MCA method, and by (79), using the FEA method (the latter is used later in this chapter). Here i is assumed to be a given function of x and so the evaluation of f_{avg} using (150) produces a number.

3.3.1.2 Average Power Dissipation

One of the optimal commutation problems studied is concerned with excitation to provide a desired average force while producing minimum heat. Since the current waveform depends on desired force, the average power inherently also depends on desired force. Although it is not straightforward to relate the average power dissipation for this static problem to the dynamic behavior of the motor, it has in fact been shown ([53]) to be equivalent to the average power in the time domain under constant velocity operation (this measure of average power dissipation neglects iron losses, and hence is appropriate for applications in which copper losses dominate iron

losses). The average power dissipation P_{avg} over the spatial period X is defined by:

$$P_{\text{avg}} = \frac{R}{X} \int_0^X i^T i \; dx \tag{151}$$

Again, since i is assumed to be a given function of x, the evaluation of P_{avg} using (151) produces a number.

3.3.1.3 Phase Voltage

In order to produce force-speed characteristics it is necessary to account for a voltage limit and so it is also necessary to introduce idealized model voltage equations (non-linear equations are used in FEA assessment in Section 3.3.2). The phase voltages satisfy

$$v_j(x, i) = Ri_j + \dot{x} \left(\frac{dL_{j,:}(x)}{dx} i + L_{j,:}(x) \frac{di}{dx} \right) \tag{152}$$

where $L_{j,:}$ denotes the jth row of L, R denotes phase resistance and $\dot{x}$ denotes speed.

3.3.1.4 Flux Density

In order to be consistent with the modeling assumption of magnetic linearity, flux densities in the teeth must be limited (this requirement is dropped in the FEA assessment in Section 3.3.2). The flux density in the teeth of each pole is computed according to

$$B_j(x, i) = \frac{L_{j,:}(x) i}{N A_t}$$

where A_t denotes the cross section area of teeth for each pole.

3.3.1.5 Problem Formulation

As mentioned earlier, formulation changes from the instantaneous-force commutation case, which are made with the purpose of increasing control over the excitation design process and increasing the application potential of the results, are accompanied by increased complexity in various aspects of the optimization including the size of

the optimization vector, the objective function, the number and size of constraint functions and implementation details. The main distinction is that the constrained optimization problems for average-force commutation are solved, i.e. the optimal excitation currents are found (from one phase current since other phase currents are shifted versions of the computed current waveform) simultaneously for all points in a spatial period of excitation (in contrast the optimization vector z previously represented three phase currents, i.e. three numbers returned by the solver for a selected position value). The distinction just mentioned means that (without reformulation) the optimization vector z, representing one phase current, is infinite in dimension since it represents a continuous function of position. Similarly constraint functions (for voltage and flux density) are infinite in dimension.

Modified notation is now introduced to allow the optimization problems to fit the framework of problem (119)–(121). The optimization problem solutions are sought on a uniform mesh so that continuous functions of position are approximated by their values at discrete position values on the mesh

$$x_k = k\frac{X}{K},\ k \in \mathcal{K} = \{0, \ldots, K-1\} \tag{153}$$

where $k = K$ is excluded due to periodicity. Consider the phase current vector at a point on the mesh $i = [i_1, i_2, i_3]^T$ and let the symbol $\tilde{}$ denote approximate solution values in the sense that

$$\tilde{i}_{j,k} \approx i_j(x_k),\ j \in \mathcal{J},\ k \in \mathcal{K} \tag{154}$$

$$\tilde{i}_k \approx i(x_k),\ k \in \mathcal{K} \tag{155}$$

where $\mathcal{J} = \{1, 2, 3\}$. The approximate full current waveform $\tilde{I}$ is given by

$$\tilde{I} \approx \left[\begin{array}{ccc} i(x_0)^T & \cdots & i(x_{K-1})^T \end{array}\right]^T \tag{156}$$

Evaluation on the mesh, using $\tilde{i}_K \equiv \tilde{i}_0$ as needed, with derivatives approximated by

differences and integrals approximated by sums, leads to discretized functions

$$\tilde{v}_{j,k}(\tilde{i}) = R\tilde{i}_{j,k} + \dot{x}\left(\frac{dL_{j,:}(x_k)}{dx}\tilde{i}_k + L_{j,:}(x_k)\frac{\tilde{i}_{k+1} - \tilde{i}_k}{X/K}\right) \tag{157}$$

$$\tilde{B}_{j,k}(\tilde{i}) = \frac{L_{j,:}(x_k)\tilde{i}_k}{NA_t} \tag{158}$$

$$\tilde{f}_k = \frac{1}{2}\tilde{i}_k^T\frac{dL(x_k)}{dx}\tilde{i}_k \tag{159}$$

$$\tilde{f}_{\text{avg}} = \frac{1}{2K}\sum_{k=0}^{K-1}\tilde{f}_k \tag{160}$$

$$\tilde{P}_{\text{avg}} = \frac{R}{K}\sum_{k=0}^{K-1}\tilde{i}_k^T\tilde{i}_k \tag{161}$$

Because phase current waveforms are shifted versions of one and the same waveform, it is only necessary to solve for one phase current and so phase 1 current waveform I_1 which is approximated by

$$\tilde{I}_1 \approx \begin{bmatrix} i_1(x_0) & \cdots & i_1(x_{K-1}) \end{bmatrix}^T \tag{162}$$

is chosen as the optimization vector.

3.3.1.6 Discretized Maximum Average Force

The first optimization problem determines excitation currents that provide maximum average force. For any speed $\dot{x}$, the problem statement is

$$\text{maximize} \quad \tilde{f}_{\text{avg}} \tag{163}$$

$$\text{subject to} \quad |\tilde{i}_{1,k}| - i_{\max} \leq 0,\ k \in \mathcal{K} \tag{164}$$

$$|\tilde{v}_{1,k}| - v_{\max} \leq 0,\ k \in \mathcal{K} \tag{165}$$

$$|\tilde{B}_{1,k}| - B_{\max} \leq 0,\ k \in \mathcal{K} \tag{166}$$

Here, average force values computed during solver iterations provides the measure for the goodness of the solution (phase 1 current waveform). This problem fits the

general framework (119)–(121) where

$$z := \begin{bmatrix} i_1(x_0) & \cdots & i_1(x_{K-1}) \end{bmatrix}^T \tag{167}$$

$$g(z) := -\tilde{f}_{\text{avg}} \tag{168}$$

$$c_{1,\cdots,3K-3}(z) := \begin{bmatrix} |\tilde{i}_{1,k}| - i_{\max},\ k \in \mathcal{K} \\ |\tilde{v}_{1,k}| - v_{\max},\ k \in \mathcal{K} \\ |\tilde{B}_{1,k}| - B_{\max},\ k \in \mathcal{K} \end{bmatrix} \tag{169}$$

The solution of this problem takes the form $\tilde{I}_1^*$ from which the remaining phase currents may be constructed. If this problem is solved over a range of $\dot{x}$ values, the optimal performance may be summarized by a relation of the form $f_{\text{avg}}^*(\dot{x})$ or, equivalently, an optimal force-speed curve.

3.3.1.7 Discretized Minimum Average Power Dissipation

The second optimization problem determines excitation currents that provide a desired average force while producing minimum heat. For any speed $\dot{x}$, the problem statement is

$$\text{minimize} \quad \tilde{P}_{\text{avg}} \tag{170}$$

$$\text{subject to} \quad \tilde{f}_{\text{avg}} - f_{\text{avg}}^d = 0 \tag{171}$$

$$|\tilde{i}_{1,k}| - i_{\max} \leq 0,\ k \in \mathcal{K} \tag{172}$$

$$|\tilde{v}_{1,k}(\tilde{i})| - v_{\max} \leq 0,\ k \in \mathcal{K} \tag{173}$$

$$|\tilde{B}_{1,k}(\tilde{i})| - B_{\max} \leq 0,\ k \in \mathcal{K} \tag{174}$$

Here, average power dissipation values computed during solver iterations provides the measure for the goodness of the solution (phase 1 current waveform). Feasible values of f_{avg}^d, for any given $\dot{x}$, may be obtained from the optimal force-speed curves

described above. This problem fits the general framework (119)–(121) where

$$z := \left[\begin{array}{ccc} i_1(x_0) & \cdots & i_1(x_{K-1}) \end{array} \right]^T \tag{175}$$

$$g(z) := \tilde{P}_{\text{avg}} \tag{176}$$

$$h_1(z) := \tilde{f}_{\text{avg}} - f^d_{\text{avg}} \tag{177}$$

$$c_{1,\cdots,3K-3}(z) := \left[\begin{array}{c} |\tilde{i}_{1,k}| - i_{\max},\ k \in \mathcal{K} \\ |\tilde{v}_{1,k}| - v_{\max},\ k \in \mathcal{K} \\ |\tilde{B}_{1,k}| - B_{\max},\ k \in \mathcal{K} \end{array} \right] \tag{178}$$

The solution of this problem takes the form $\tilde{I}_1^*$ from which the remaining phase currents may be constructed and the corresponding minimized average power dissipation P^*_{avg} may be computed.

3.3.1.8 Implementation and Numerical Results

The discretized optimization problems are solved using function `fmincon` of the MATLAB Optimization Toolbox [90]. This is an iterative search method, so achieving reliable convergence requires that the unknown current values be appropriately initialized. Problem size is reduced by choosing K to be divisible by 3, so that the discrete approximations of all phase currents can be obtained from $\tilde{I}_1^*$ by circular shifting of the data.

Table 1 provides the actual parameter values employed to compute optimal excitation results for two motors (coupled and uncoupled) that run on the same stator bar. Both copper and steel contribute to the moving mass values. Using AWG 21 wire, the coupled motor accommodates $N = 224$ turns distributed over 2 poles, whereas the uncoupled motor accommodates $N = 364$ turns distributed over 4 poles. The moving steel of the coupled motor consists of one E-core on each side, whereas the moving steel of the uncoupled motor consists of three C-cores on each side. Accordingly, the moving mass values are $M = 2.03$ kg for the coupled motor and $M = 2.87$ kg for the uncoupled motor. Voltage limit used is 170 V.

3.3.1.9 Maximum Average Force

Results from solving problem (163)–(166) at various speeds are shown in Figure 40 after scaling by (unloaded) moving mass values. The uncoupled motor can produce larger average accelerations at any given speed. On the other hand, the coupled motor maintains a uniform average acceleration capability over a wider speed range.

The waveforms required for maximizing average acceleration are given in Figure 41 for the coupled motor and in Figure 42 for the uncoupled motor. For the zero-speed cases, only the flux density constraints are active. For the high-speed cases, the voltage constraints are clearly active. At all speeds, the instantaneous force deviates substantially from the average force.

3.3.1.10 Minimum Average Power Dissipation

Results from solving problem (170)–(174) at various speeds and desired average accelerations (unloaded) are shown in Table 10. Feasible values of desired average acceleration can be determined from Figure 40. The results reveal that, for a given desired average acceleration, the coupled motor has lower average power dissipation. This advantage is not readily predictable without the numerical study.

The waveforms required for minimizing average power dissipation while providing a desired average acceleration of 35 m/s^2 (unloaded) are shown in Figure 43 for the coupled motor and in Figure 44 for the uncoupled motor. For the zero-speed cases, only the flux density constraints are active. For the higher-speed cases, the voltage constraints are clearly active. At all speeds, the instantaneous force deviates substantially from the average force.

3.3.2 Uncoupled Motor Assessment via FEA Modeling

Accurate FEA-data based models have been derived in Chapter 2 to fully characterize uncoupled LVR motors. These models are now used in conjunction with the heat-minimizing optimal commutation formulation of Section 3.3.1 in order to assess

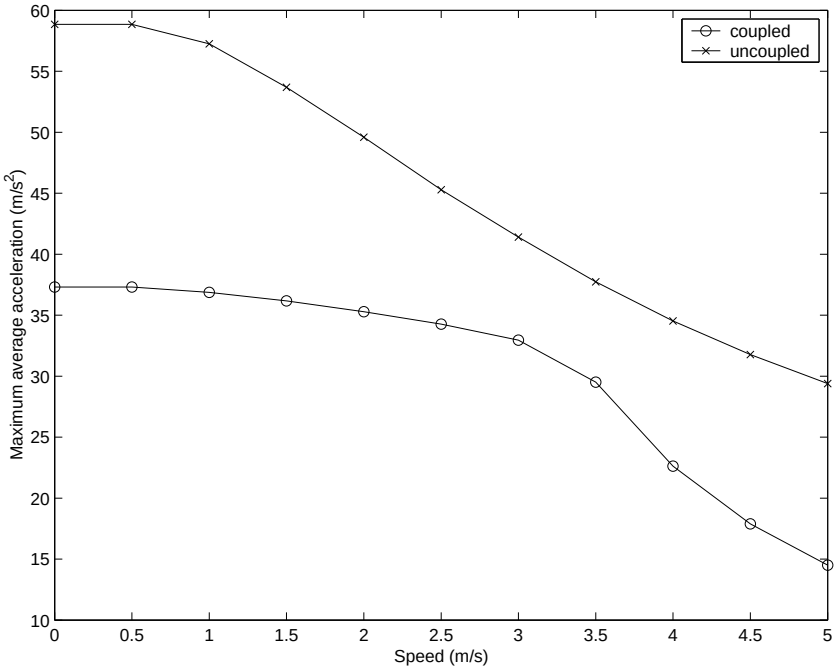

Figure 40: Maximum average acceleration versus speed.

Table 10: Comparative Minimum Power Dissipation (W)

$\bar{a}(\mathrm{m/s^2})$	$\dot{x}(\mathrm{m/s})$	Coupled	Uncoupled
5	0	2.09	3.33
15	0	6.29	9.94
25	0	11.25	16.77
35	0	17.86	24.05
≥ 45	0	not feasible	≥ 32.07
5	1	2.10	3.33
15	1	6.49	9.99
25	1	11.63	16.96
35	1	19.50	24.56
≥ 45	1	not feasible	≥ 33.89
5	2	2.19	3.34
15	2	7.21	10.39
25	2	13.13	18.34
35	2	21.48	28.6
≥ 45	2	not feasible	≥ 48.39

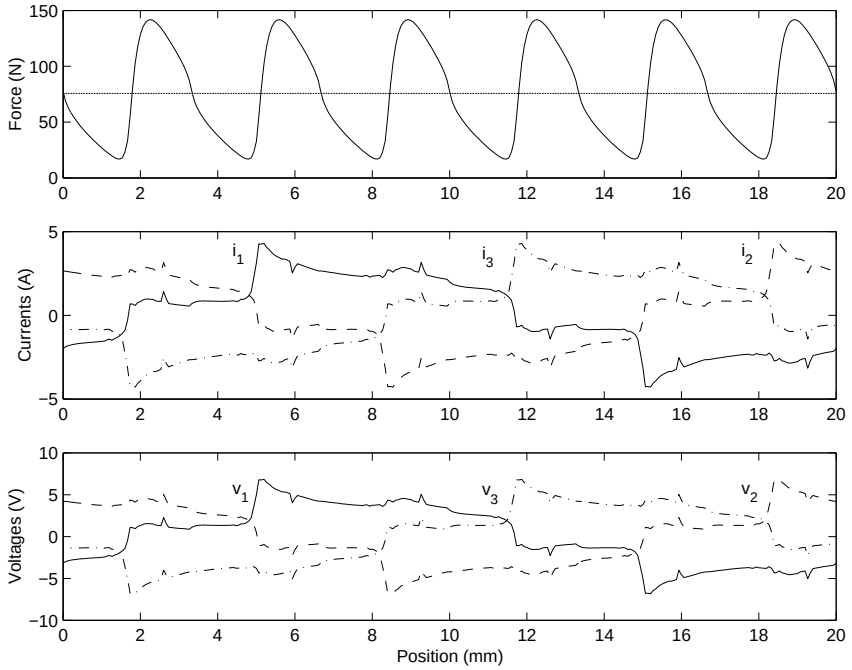

(a) $\dot{x} = 0$ m/s.

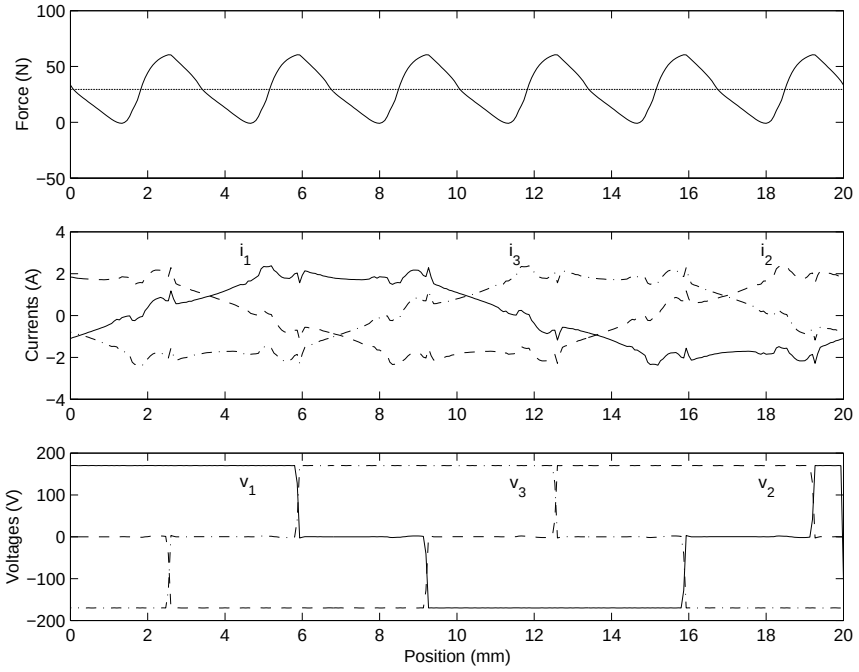

(b) $\dot{x} = 5$ m/s.

Figure 41: Waveforms for maximum average force (coupled motor).

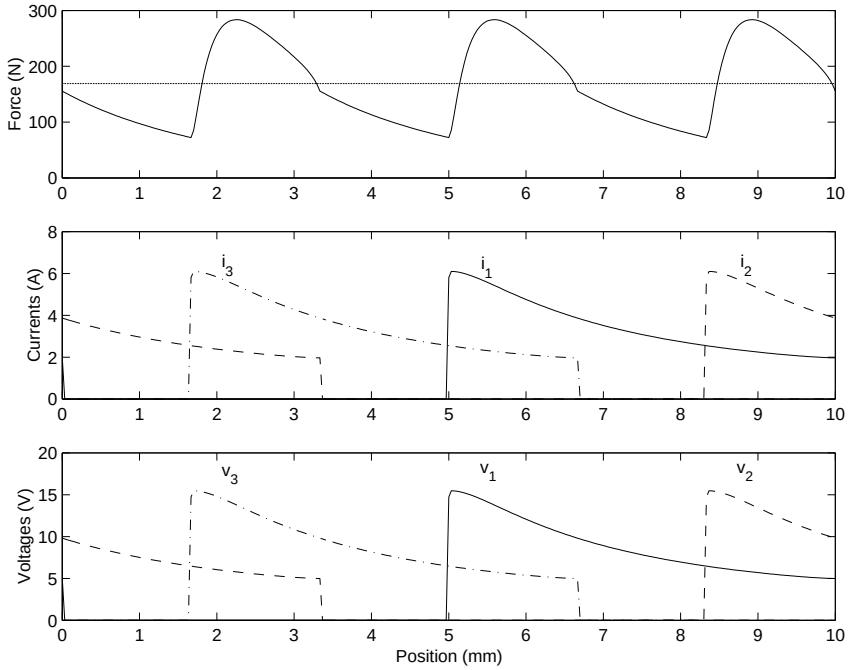

(a) $\dot{x} = 0$ m/s.

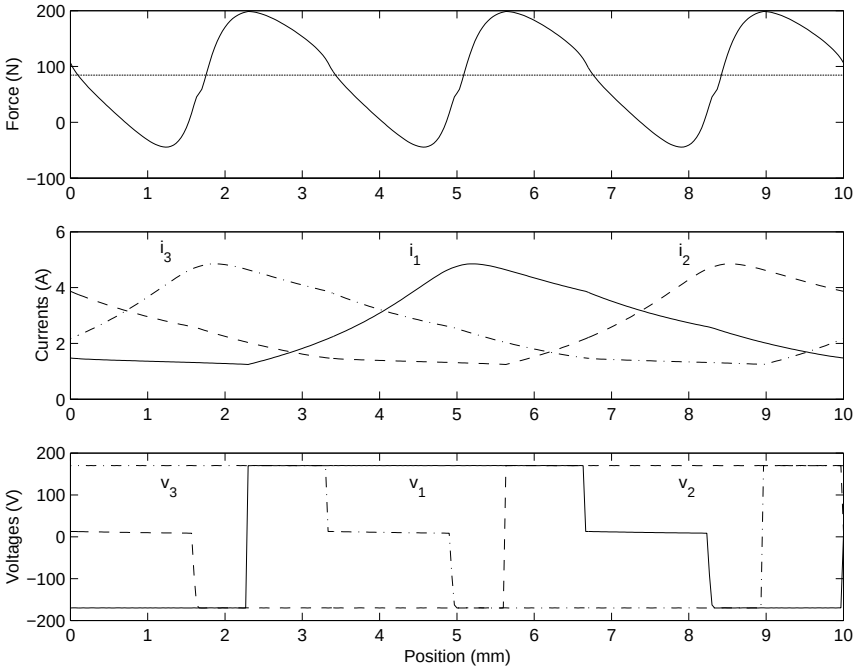

(b) $\dot{x} = 5$ m/s.

Figure 42: Waveforms for maximum average force (uncoupled motor).

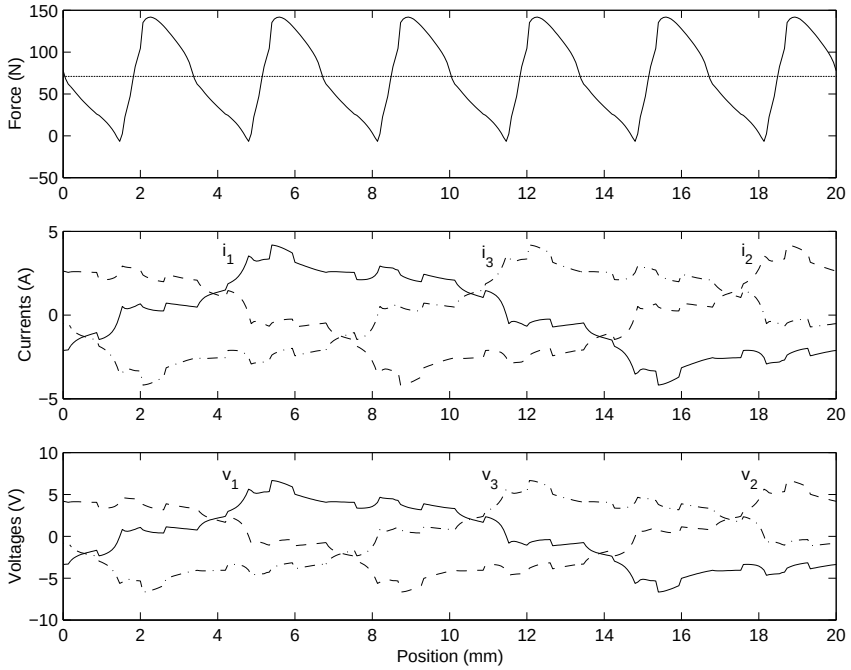

(a) $\dot{x} = 0$ m/s.

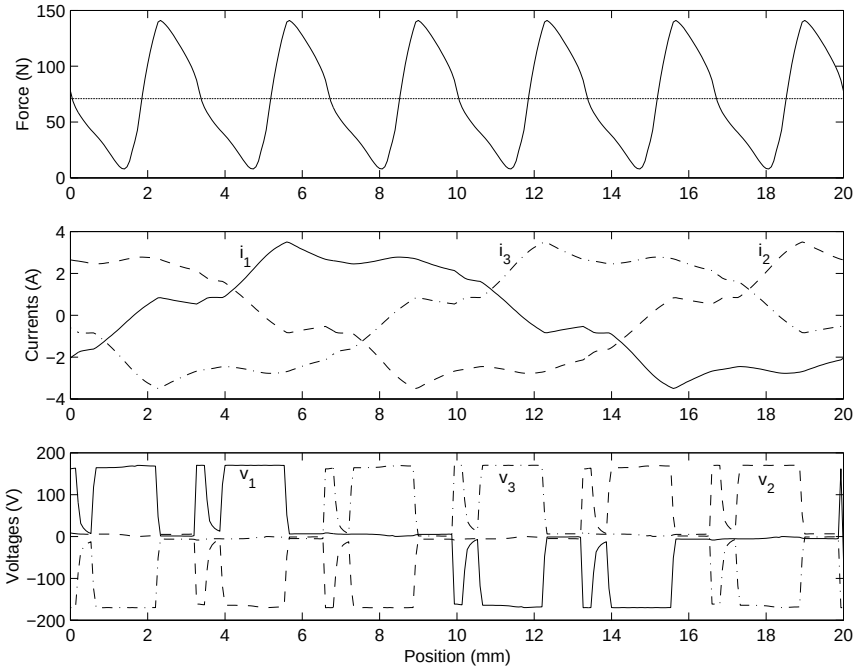

(b) $\dot{x} = 2$ m/s.

Figure 43: Waveforms for minimum average power dissipation at 35 m/s^2 average acceleration (coupled motor).

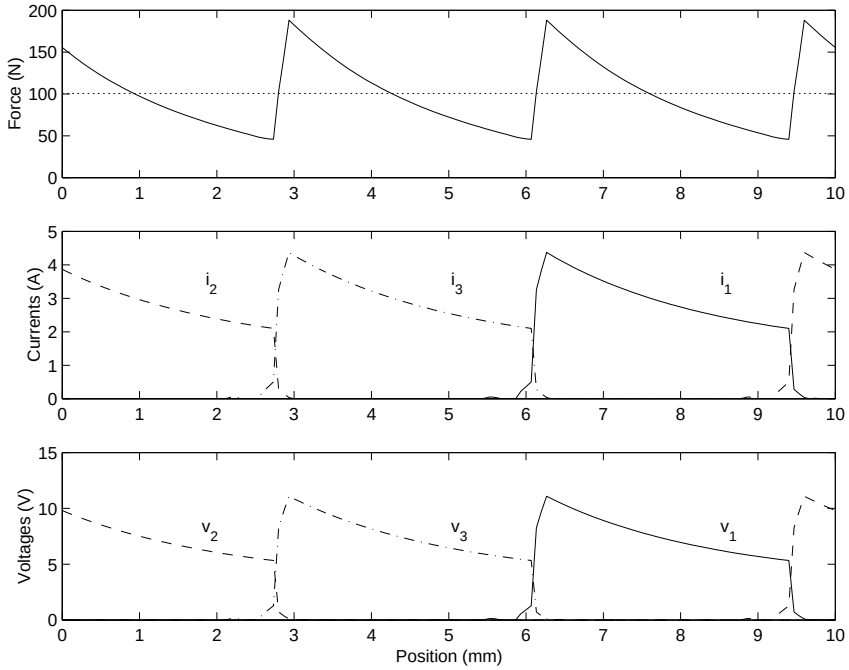

(a) $\dot{x} = 0$ m/s.

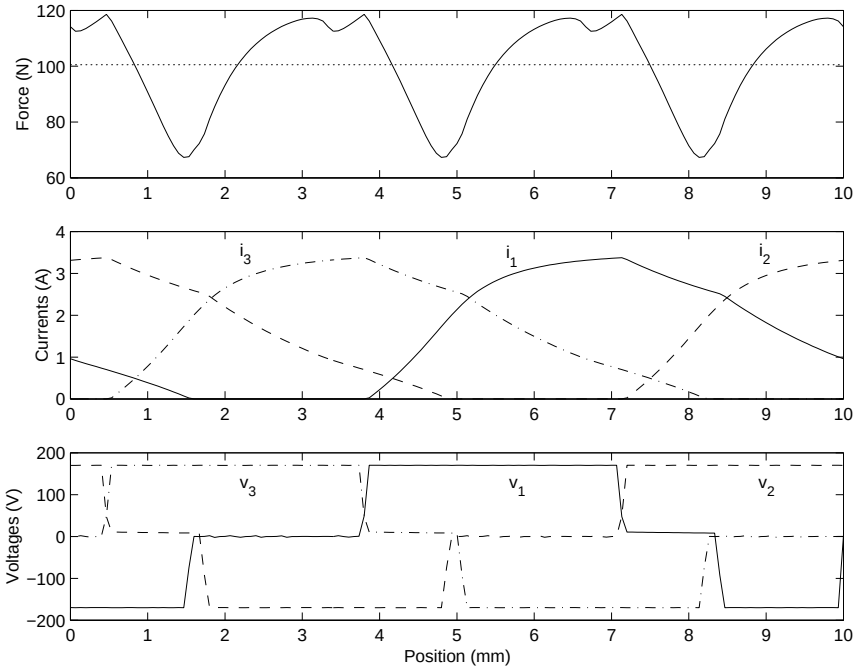

(b) $\dot{x} = 2$ m/s.

Figure 44: Waveforms for minimum average power dissipation at 35 m/s^2 average acceleration (uncoupled motor).

the acceleration performance capability of uncoupled LVR motors. The objective of the optimization is to produce current waveforms that minimize average power dissipation while producing a desired average force or a desired average force-to-mass ratio. Consideration of the ratio of current-limited average force to moving mass or, equivalently, the maximum achievable average acceleration is again motivated by the targeted manufacturing applications, focusing on the heat produced as a result of accelerating a load.

Incorporating the FEA-based modeling of Chapter 2 results in modifying the optimization problem given in (170)–(174) by removing flux density constraints and by modifying the underlying phase voltage computation to use the non-idealized functional expression for phase flux linkage λ_j which is defined by (73). The phase voltage expression in (152) is replaced by

$$v_j(x, i) = Ri_j + \dot{x}\left(\frac{d\lambda_j}{dx}\right) \tag{179}$$

Numerical results showing optimized excitation currents are presented for three motors (distinguished by tooth width). Table 1 provides the motor parameter values employed. The magnetic material is assumed to be M19 steel. Both copper and steel contribute to the moving mass values. Using AWG 21 wire, the three motors accommodate $N = 408$, 384 and 364 turns distributed over 4 poles. The moving steel consists of three C-cores on each side. Accordingly, the moving mass values are $M = 2.61$, 2.73 and 2.87 kg. The voltage limit is 170 V.

Results from solving problem (170)–(174) at various speeds and various desired average force-to-mass values are shown in Table 11. Since the motivation here is point-to-point positioning applications, the comparison is based not on a common desired average force, but on a common desired average force-to-mass ratio instead. As a consequence, the results will show the minimum amount of heat that must be generated in order to provide a desired acceleration for the various motors (without any payloads attached).

According to Table 11, for each motor separately and for a fixed speed, average power dissipation increases with desired average force. This increase is nonlinear (due to magnetic saturation and voltage limits) with a higher rate of increase as desired average force increases. For a fixed desired average force-to-mass value, there is an increase in average power dissipation with speed that is more apparent at higher speeds; the increase is higher for wider tooth widths. Comparing all motors at the same desired average force-to-mass value and at the same speed, average power dissipation increases with tooth width.

The waveforms required for minimizing average power dissipation while providing a desired average force-to-mass value of 35 m/s^2 (unloaded) are shown in Figure 45 for $\alpha = 0$, Figure 46 for $\alpha = 0.5$ and Figure 47 for $\alpha = 1$. The corresponding average force values required to achieve the desired average force-to-mass values are 91.35, 95.55 and 100.45 N, and they are indicated in the figures as well. For the higher-speed cases, the voltage constraints are clearly active. At all speeds, the instantaneous force deviates substantially from the average force. Overall the waveforms for motors with different tooth geometry bear similarities in shape, but there are some differences, e.g. the turn-on and turn-off positions of the phase currents are different, and so is the deviation of instantaneous force from the average value, which is higher for wider teeth.

At least for this group of motors, if the focus is on producing average acceleration rather than average force, then the narrow tooth motor outperforms the others with respect to optimization problem (170)–(174).

3.3.3 Average-Force Commutation with Ripple Specification

In the average-force commutation above, force ripple (the variation of instantaneous force about the average force value) is not controlled. When force ripple constraints are added, the solution space of the optimization problems expands as will become

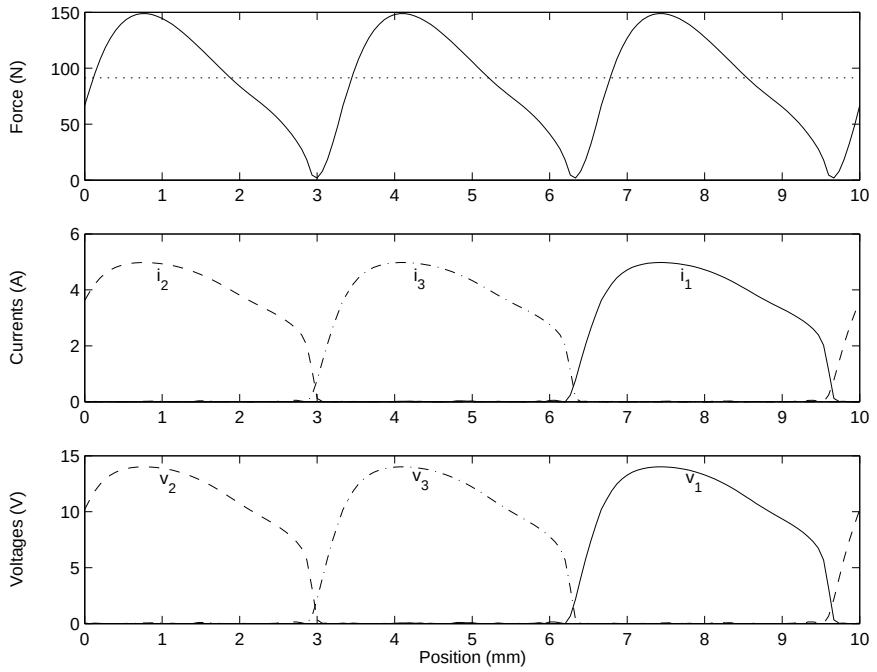

(a) $\dot{x} = 0$ m/s.

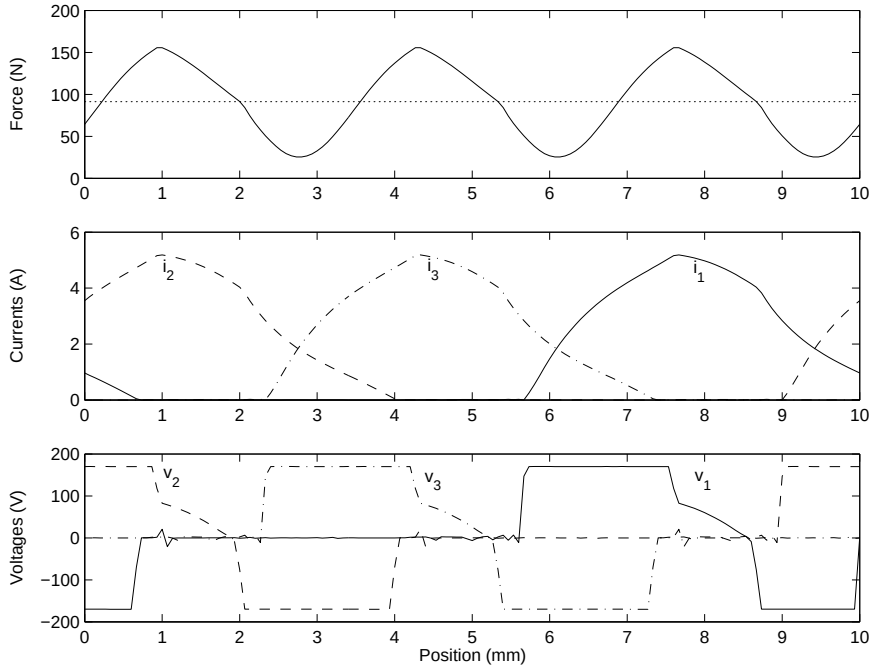

(b) $\dot{x} = 2$ m/s.

Figure 45: Waveforms for minimum average power dissipation at average force/mass of 35 m/s^2 ($\alpha = 0$).

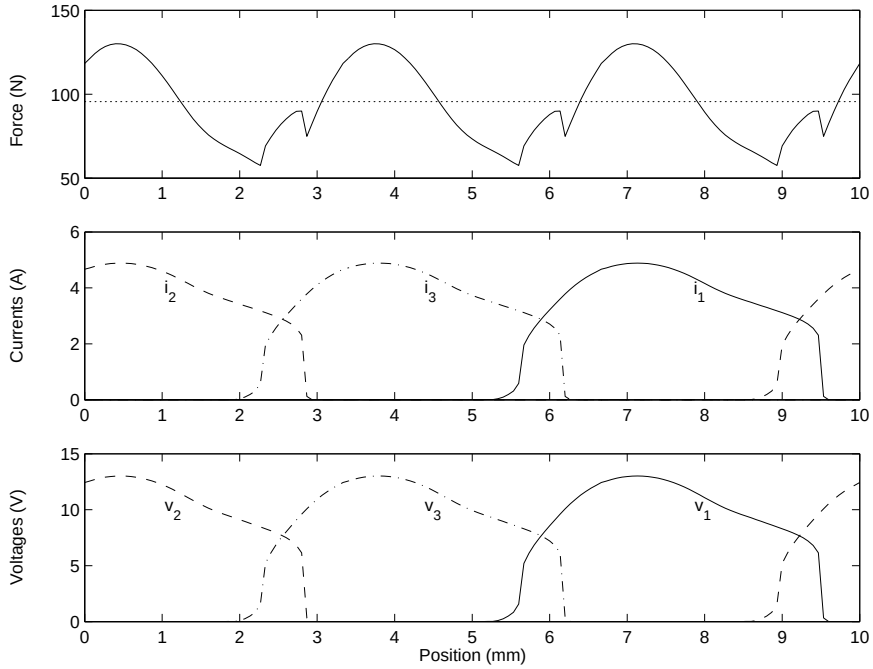

(a) $\dot{x} = 0$ m/s.

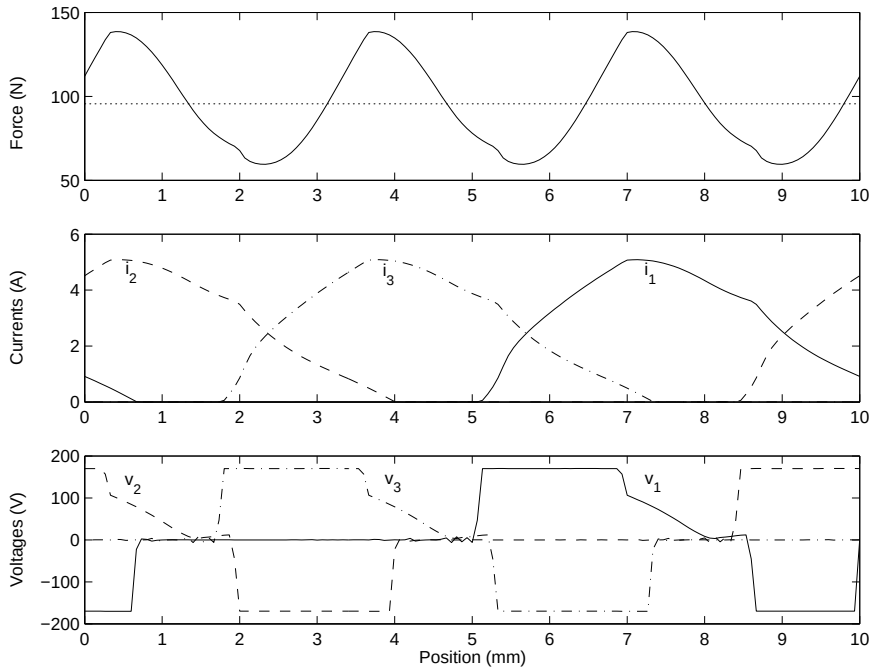

(b) $\dot{x} = 2$ m/s.

Figure 46: Waveforms for minimum average power dissipation at average force/mass of 35 m/s^2 ($\alpha = 0.5$).

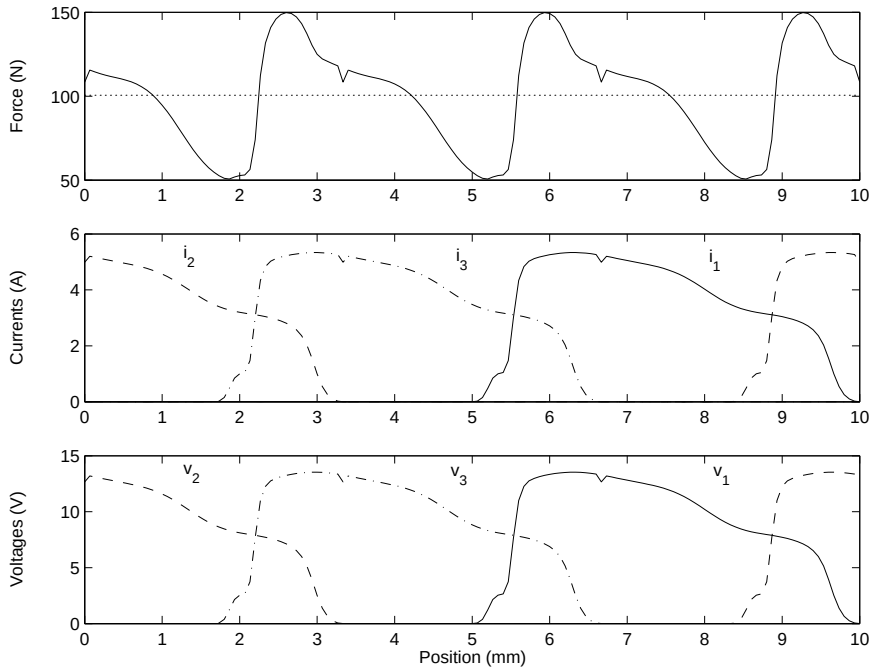

(a) $\dot{x} = 0$ m/s.

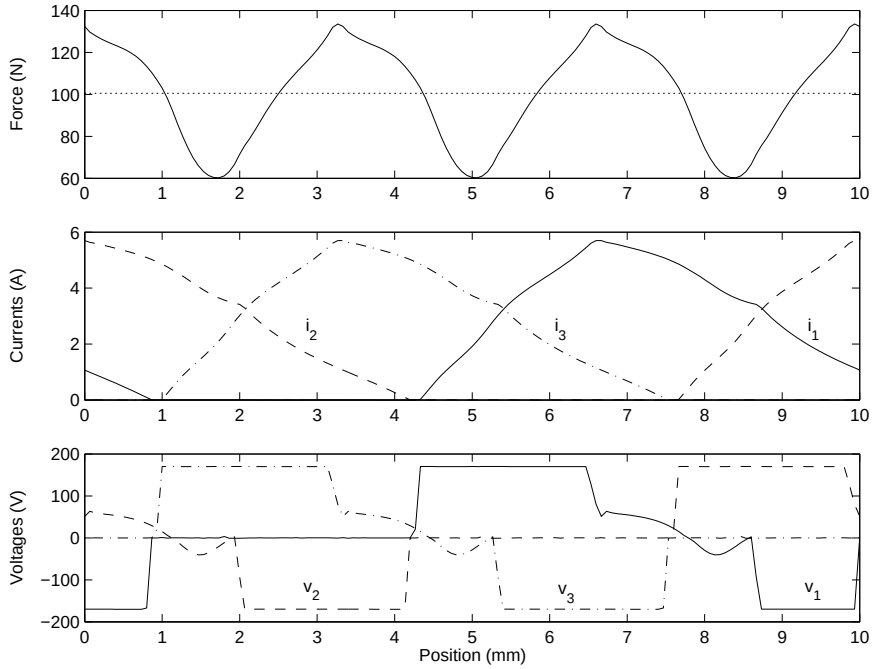

(b) $\dot{x} = 2$ m/s.

Figure 47: Waveforms for minimum average power dissipation at average force/mass of 35 m/s^2 ($\alpha = 1$).

Table 11: Comparative Minimum Average Power Dissipation (W)

force/mass (m/s^2)	$\dot{x}$ (m/s)	$\alpha = 0$	$\alpha = 0.5$	$\alpha = 1$
5	0	5.38	6.09	6.96
15	0	16.99	18.89	21.92
25	0	29.86	32.56	38.81
35	0	45.00	47.96	58.56
45	0	63.04	65.73	84.48
5	1	5.41	6.17	7.21
15	1	17.00	19.06	22.33
25	1	30.00	32.77	39.31
35	1	45.22	48.21	59.85
45	1	63.43	65.98	86.38
5	2	5.52	6.23	7.24
15	2	17.19	19.22	22.48
25	2	30.60	33.19	40.37
35	2	46.64	49.07	62.71
45	2	66.00	67.52	92.61

clear shortly. First force ripple is discussed.

In the context of positioning applications, force is an important factor to consider. However, an attribute of force production in variable reluctance motors is force ripple, and applications differ in their tolerance of this attribute with some requiring that it be eliminated. Qualitatively, force ripple can be described as the periodic variation of force production around a desired constant value; force variation about a desired average value is evident in all of force waveforms in Section 3.3.1 which were obtained as functions of current and displacement without any restriction on force ripple. The average value of a force waveform over a spatial period X of excitation currents is given by (150). Mathematically, the force ripple waveform is defined as

$$\rho(x, i) = f(x, i) - f_{\text{avg}} \tag{180}$$

and its size, $\|\rho(x, i)\|$, can be quantified by a suitable choice from among several

possible indices such as its peak-to-peak value and its p-norms over one spatial period:

$$\|\rho(x,i)\| \equiv \begin{cases} \max(\rho(x,i)) - \min(\rho(x,i)), \text{ peak-to-peak} \\ \left(\int_0^X |\rho(x,i)|^p \ dx\right)^{\frac{1}{p}}, \ p\text{-norm} \end{cases} \tag{181}$$

For $p = \infty$ the norm definition reduces to $\max(|\rho(x,i)|)$. The size of force ripple may theoretically take any value in the range $0 \leq \|\rho(x,i)\| \leq \infty$; the lower limit $\check{\rho}$ is 0, but realistically the upper limit $\hat{\rho}$ is finite and can be found from unconstrained ripple analysis. In summary, the range of force ripple is described by

$$0 = \check{\rho} \leq \|\rho(x,i)\| \leq \hat{\rho} < \infty \tag{182}$$

For meaningful comparison of the ripple sizes of different waveforms, it is appropriate to express ripple size in a given force waveform with respect to average force to obtain a normalized dimensionless ratio

$$\wp = \|\rho(x,i)\| / f_{\text{avg}} \tag{183}$$

It is of interest to investigate the shapes of the resulting waveforms with the different ripple size indices in order to determine if or how the added degree of freedom (the choice of ripple index) influences power dissipation, residual vibration and/or command tracking ability for motion control applications. In fact, preliminary investigation on LVR motor commutation showed obvious variation in the shape of force (and force-ripple) waveforms and the associated average power dissipation based on the index selected for controlling force ripple in the motor force, leading to the choice of the 1-norm for numerical results used in this research since it produced currents with the least average power dissipation.

The average-force optimal commutation objectives are now restated to include force ripple specification, and the following two problems are addressed:

1. maximum ripple-specified average force production resulting in force-speed characteristics parametrized by force ripple

2. minimum average power dissipation while producing a desired ripple-specified average force

Without ripple specification, each problem as solved in the previous section would provide one unique solution (the solution corresponding to unconstrained force ripple), but when this concept is applied, it becomes possible to determine VR motor excitation to (i) produce force waveforms without any restrictions on force ripple, (ii) to produce smooth force with zero ripple and (iii) to produce force waveforms with any of an infinite number of possible ripple sizes between these two extremes (but only a few choices are necessary for obtaining practical results).

The maximum value $\hat{\wp}$ of force ripple size in ripple waveform corresponds to an optimized force with no constraints on ripple size. In order to prepare for subsequent formulation to control the size of force ripple, the following notation is introduced

$$\wp_{\max} = \beta\hat{\wp},\ \beta \in [0,1] \tag{184}$$

where $\wp_{\max} \leq \hat{\wp}$ is a limit imposed on the force ripple size when computing optimal excitation; implicitly the force waveform is associated with a speed of operation. Mathematical formulation and solution of the optimization problems are presented next.

3.3.3.1 Problem Formulation

The major difference from the formulation in Section 3.3.1.5 is the imposition of a limit on force ripple. As in that section, the optimization vector and constraint functions are infinite in dimension; therefore, the optimization problems are discretized and the solutions are sought on a uniform mesh so that continuous functions of position are approximated by their values at discrete position values on the mesh (153). Discretization is the same as shown in Section 3.3.1.5 except for additional notation needed in order to impose ripple constraints. Approximate discrete points of the

ripple waveform in (180) are approximated by $\tilde{\rho}_k$:

$$\tilde{\rho}_k = \tilde{f}_k - \tilde{f}_{\text{avg}}$$

where $\tilde{f}_{\text{avg}}$ and $\tilde{f}_k$ are defined by (159) and (160). The full force ripple waveform $\tilde{\rho}$ is given by

$$\tilde{\rho} = \begin{bmatrix} \rho(x_0) & \cdots & \rho(x_{K-1}) \end{bmatrix}^T$$

Finally, the size of force ripple is approximated by $\tilde{\wp}$:

$$\tilde{\wp} = \|\tilde{\rho}\| / \tilde{f}_{\text{avg}}$$

In addition to imposing a constraint on force ripple, explicit current constraints are removed. Power converter instantaneous limits on current are usually too high to be active constraints (over-current protective devices are assumed to be used); temperature rise limits can be stated as average power dissipation limits, but for the purposes of subsequent positioning performance assessment, average power dissipation is viewed as a performance cost and is computed post simulation for each positioning task. All other variables in the optimization problem statements remain the same as in Section 3.3.1.5. It is now possible to proceed with discretized problem formulation.

3.3.3.2 Discretized Maximum Average Force

This optimization problem determines the motor performance limits as defined by ripple-specified maximum average force. For any speed $\dot{x}$, the problem is stated as

$$\text{maximize} \quad \tilde{f}_{\text{avg}} \tag{185}$$

$$\text{subject to} \quad \tilde{\wp} - \wp_{\max} \leq 0 \tag{186}$$

$$|\tilde{v}_{j,k}(\tilde{\imath})| - v_{\max} \leq 0,\ j \in \mathcal{J},\ k \in \mathcal{K} \tag{187}$$

$$|\tilde{B}_{j,k}(\tilde{\imath})| - B_{\max} \leq 0,\ j \in \mathcal{J},\ k \in \mathcal{K} \tag{188}$$

This problem fits the general framework (119)–(121) where

$$z := \begin{bmatrix} i_1(x_0) & \cdots & i_1(x_{K-1}) \end{bmatrix}^T \tag{189}$$

$$g(z) := \tilde{f}_{\text{avg}} \tag{190}$$

$$c_{1,\cdots,2K-1}(z) := \begin{bmatrix} \tilde{\wp} - \wp_{\max} \\ |\tilde{v}_{1,k}| - v_{\max},\ k \in \mathcal{K} \\ |\tilde{B}_{1,k}| - B_{\max},\ k \in \mathcal{K} \end{bmatrix} \tag{191}$$

The solution of this problem takes the form $\tilde{I}_1^*$ from which the remaining phase currents may be constructed. If this problem is solved over a range of $\dot{x}$ values for each ripple constraint $\wp_{\max}$, the optimal performance can be summarized by a relation of the form $f_{\text{avg}}^*(\dot{x}, \beta)$; equivalently optimal force-speed curves, parameterized by $\wp_{\max}$, can be produced. The simulation examples of Chapter 4 use $f_{\text{avg}}^*(\dot{x}, \beta = 0)$ and $f_{\text{avg}}^*(\dot{x}, \beta = 1)$, in determining feasible position trajectories and actuator saturation limits for the purpose of comparing positioning performance when these two ripple extremes are used in commutation design.

3.3.3.3 Discretized Minimum Average Power Dissipation

The second optimization problem determines excitation currents that provide a desired ripple-specified average force while producing minimum heat. For any speed $\dot{x}$, the problem is stated as

$$\text{minimize} \quad \tilde{P}_{\text{avg}} \tag{192}$$

$$\text{subject to} \quad \tilde{f}_{\text{avg}} - f_{\text{avg}}^d = 0 \tag{193}$$

$$\tilde{\wp} - \wp_{\max} \leq 0 \tag{194}$$

$$|\tilde{v}_{j,k}| - v_{\max} \leq 0,\ j \in \mathcal{J},\ k \in \mathcal{K} \tag{195}$$

$$|\tilde{B}_{j,k}| - B_{\max} \leq 0,\ j \in \mathcal{J},\ k \in \mathcal{K} \tag{196}$$

This problem fits the general framework (119)–(121) where

$$z := \begin{bmatrix} i_1(x_0) & \cdots & i_1(x_{K-1}) \end{bmatrix}^T \tag{197}$$

$$g(z) := \tilde{P}_{\text{avg}} \tag{198}$$

$$h_1(z) := \tilde{f}_{\text{avg}} - f^d_{\text{avg}} \tag{199}$$

$$c_{1,\cdots,2K-1}(z) := \begin{bmatrix} \tilde{\wp} - \wp_{\max} \\ |\tilde{v}_{1,k}| - v_{\max},\ k \in \mathcal{K} \\ |\tilde{B}_{1,k}| - B_{\max},\ k \in \mathcal{K} \end{bmatrix} \tag{200}$$

The solution of this problem takes the form $\tilde{I}^*_1$ from which the remaining phase currents may be constructed and the corresponding optimal dissipation P^*_{avg} may be computed. Feasible values of f^d_{avg}, for any given $\dot{x}$ and $\wp_{\max}$, may be obtained from force-speed curves obtained by solving the force maximization problem above. When force ripple is limited to zero, a smooth force waveform results whose average and instantaneous values are identical (within numerical solver tolerance). When non-zero force ripple is tolerable, different force waveforms can be obtained depending on the index chosen in quantifying ripple.

3.3.3.4 Implementation and Numerical Results

The discretized optimization problems are solved using function `fmincon` of the MATLAB Optimization Toolbox which requires that the unknown current values be appropriately initialized. Again, problem size is reduced by choosing K to be divisible by 3, so that the discrete approximations of all phase currents can be obtained from $\tilde{I}^*_1$ by circular shifting of the data. In the numerical results below, the 1-norm for ripple index is chosen. Optimal excitation results computed for the coupled and uncoupled motors with the parameter values in Table 1 (with $\alpha = 1$ and $v_{\max} = 270$ V) are presented below.

Results from solving the force maximizing problem (185)–(188) at various speeds for several values of desired force ripple $\wp_{\max}$ were used to produce the force-speed

curves in Figure 48 (coupled motor) and Figure 49 (uncoupled motor). First the problem was solved without constraints on ripple, producing the top curve in each figure. Each point of the top curve (representing maximum average force at a corresponding speed) is associated with a force-displacement waveform exhibiting the largest ripple possible. Ripple constraints for subsequent problem solutions at that speed are specified as percentages of that maximum value. As expected with any motor, each curve exhibits decreased achievable force with speed. Across all curves, and for each speed value, it is seen that the maximum achievable force decreases as maximum ripple value decreases.

The force-speed curves are useful in determining feasible average force values. For example, ripple-unconstrained force is achievable at any desired value that falls under the top curve and smooth force (zero-ripple) can be achieved for any value that falls under the bottom curve. Similar logic can be applied for any intermediate ripple value.

The heat minimizing problem (192)–(196) is solved for fixed speed and desired average force values. The problem is solved at the extremes of ripple (with unconstrained ripple and with zero ripple). Example waveforms required for minimizing average power dissipation while providing a desired force value are shown in Figures 50–51 for the coupled motor and in Figures 52–53 for the uncoupled motor. The synchronous-motor-like behavior of the coupled motor is evident in the three-phases-on excitation while the "switched" nature of the uncoupled motor is evident in the one-phase- or two-phases-on excitation.

3.3.4 Influence of Ripple on Average Power Dissipation

Average power dissipation values associated with a fixed desired average force, a fixed speed and values of $\beta \in [0, 1]$ are obtained for the uncoupled motor from the optimization results above and their values as percentages of the highest power dissipation

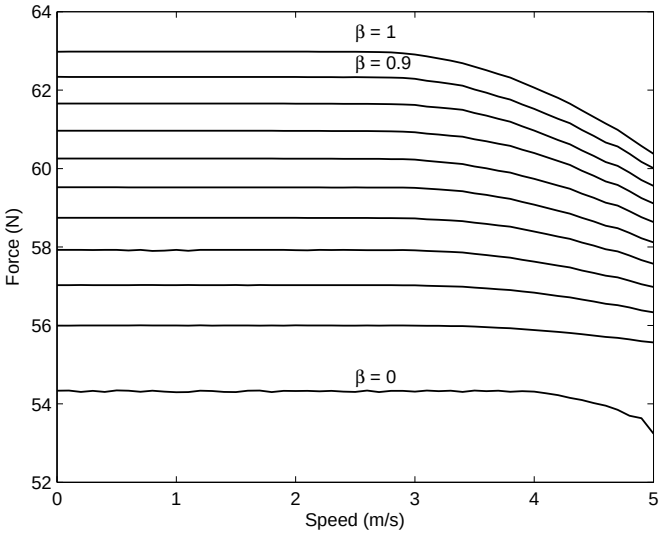

Figure 48: Force-speed characteristics parameterized by ripple size (coupled motor).

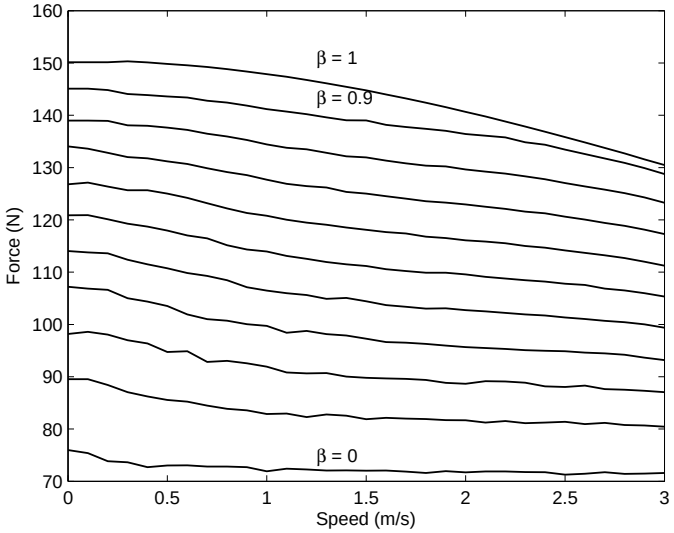

Figure 49: Force-speed characteristics parameterized by ripple size (uncoupled motor).

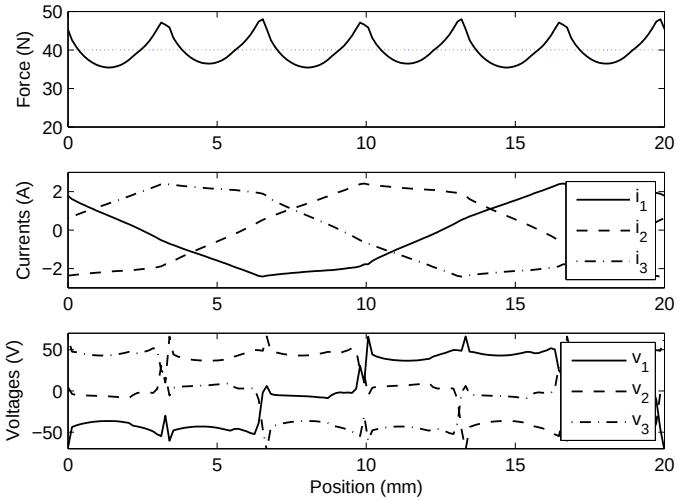

(a) $\beta = 1$.

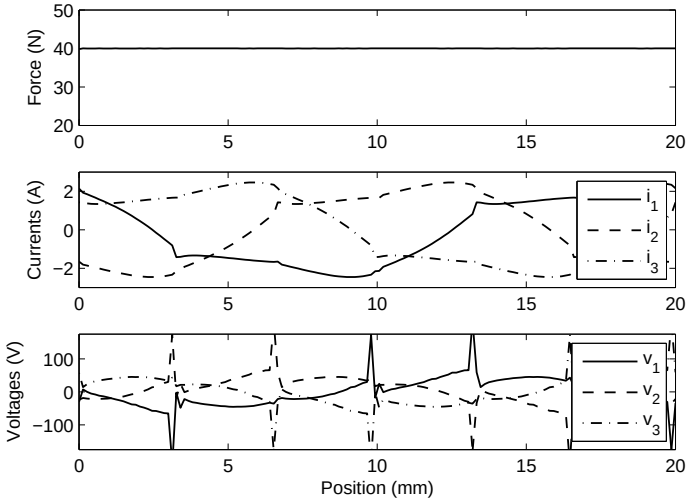

(b) $\beta = 0$.

Figure 50: Waveforms for minimum average power dissipation for a desired average force of 40 N at 1 m/s (coupled motor).

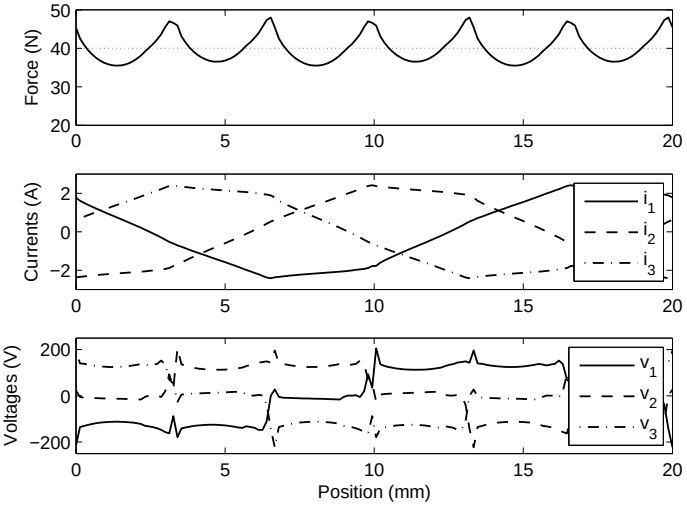

(a) $\beta = 1$.

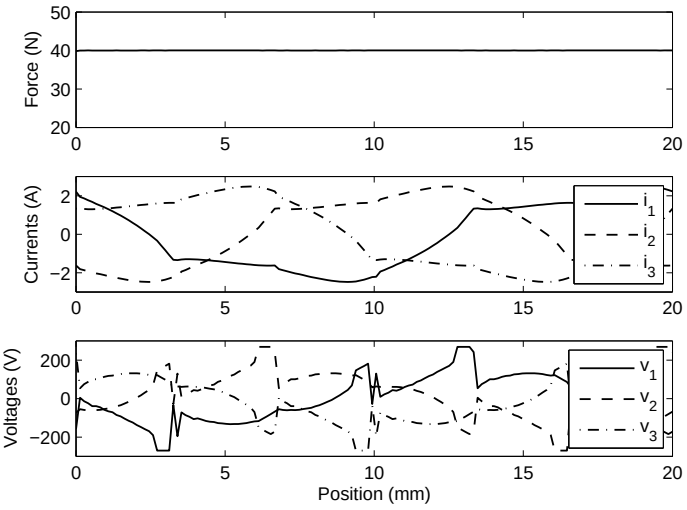

(b) $\beta = 0$.

Figure 51: Waveforms for minimum average power dissipation for a desired average force of 40 N at 3 m/s (coupled motor).

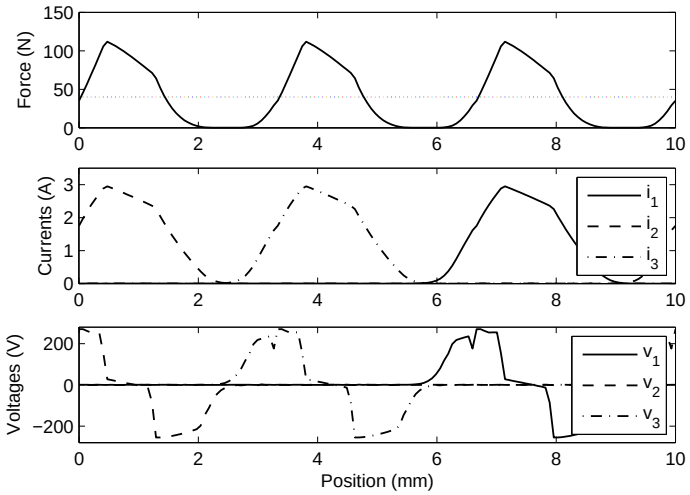

(a) $\beta = 1$.

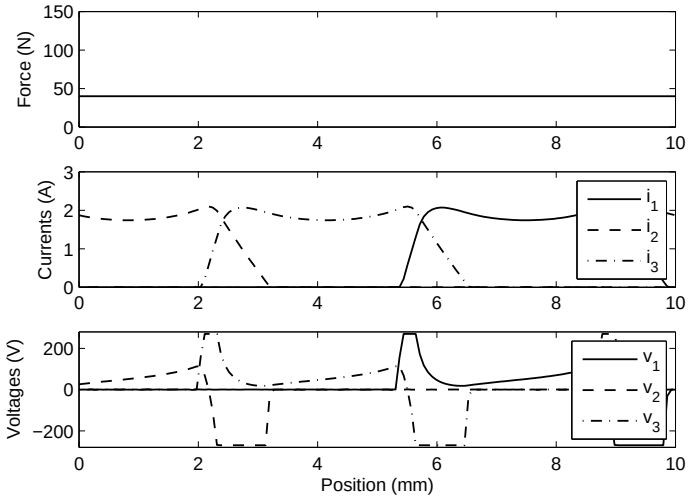

(b) $\beta = 0$.

Figure 52: Waveforms for minimum average power dissipation for a desired average force of 40 N at 1 m/s (uncoupled motor).

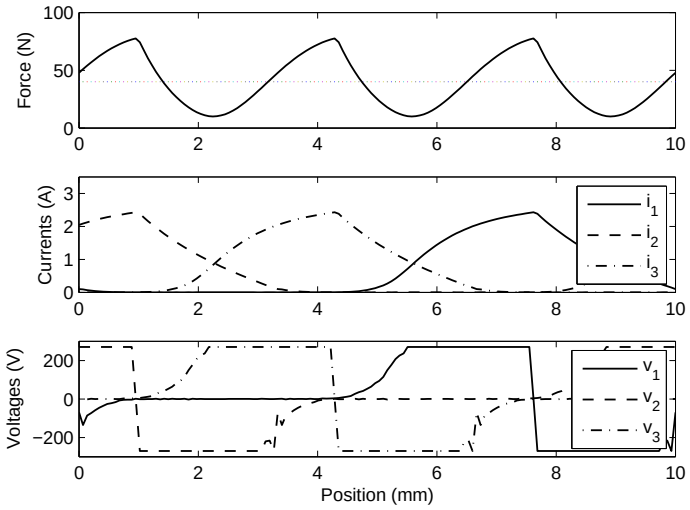

(a) $\beta = 1$.

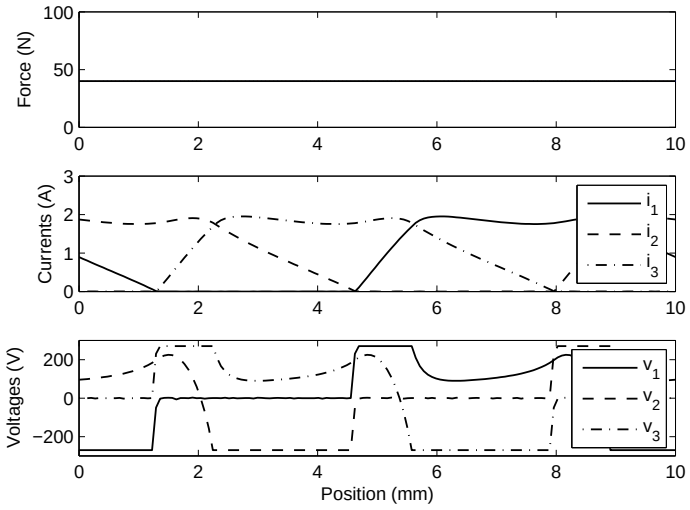

(b) $\beta = 0$.

Figure 53: Waveforms for minimum average power dissipation for a desired average force of 40 N at 3 m/s (uncoupled motor).

(that of the no-ripple case) are plotted versus ripple size in Figure 54. The figure shows that average power dissipation decreases with increased ripple. This can be explained by the fact that more ripple corresponds to more optimization freedom over a spatial period of operation making it possible to exploit regions of high inductance slope (regions of better force production per ampere); these regions then contribute proportionately more to the desired average force than regions of lower inductance slope. For the range of speed covered in the numerical results for both motors, the coupled motor exhibits less significant variation in force production and the associated average power dissipation.

It has been shown in [53] that spatial average power dissipation is equivalent to the average power dissipation in the time domain under constant velocity operation. That equivalence is important because it is also shown (assuming motor has constant thermal resistance) to be directly related to temperature rise in repetitive motion applications. However, it is still necessary to perform position control simulations (Chapter 4) to determine if the trend of improved power dissipation with ripple in the static sense is enough to offset, under dynamic operation, higher power dissipation from faster positioning (higher ripple content, higher force and higher currents).

3.4 Conclusion

Motivated by manufacturing applications, this chapter formulated and solved optimal commutation problems for two LVR motor configurations resulting in a multitude of contributions. Distinct features of the coupled motor have been presented including the advantage of "synchronous" rather than "switched" excitation and illustration of the motor's internal force production mechanism and how that is influenced by air gap geometry and the converter connection. The coupled and uncoupled configurations are compared with focus on the heat produced as a result of accelerating a load. Uncoupled motor performance assessment is also presented using accurate FEA-data

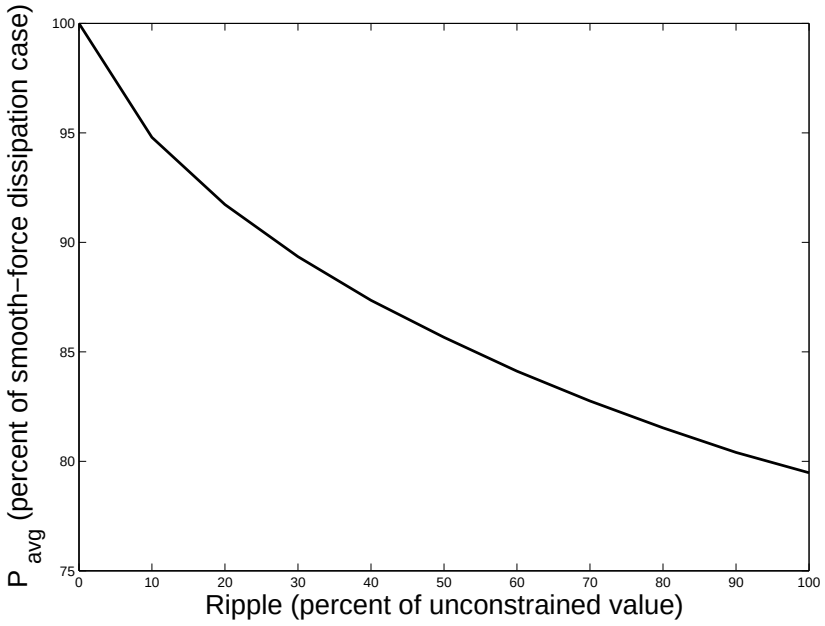

Figure 54: Typical average power dissipation trend vs ripple for a fixed f_{avg}.

based modeling.

This chapter defined force ripple and identified possible ways to measure its size. The mathematical formulation given applies to linear (including or excluding spatial harmonics) and non-linear models of force. Force ripple in VR motors is a prominent factor in excitation design and in force characteristics; consequently it impacts their positioning performance and is central in this dissertation.

In the most general case, optimal commutation formulation is extended to include force ripple specification. The results of solving the ripple-specified force-maximizing and heat-minimizing optimal commutation problems, demonstrate that relaxing force ripple constraints is favorable in both optimization problems when considered separately. For the purposes of positioning assessment, the first optimization provides force limits and hence possible positioning trajectories and associated possible nominal travel times while the second optimization provides the actual current waveforms to populate lookup tables for retrieval during dynamic simulation of positioning tasks. While both optimization problems favor relaxed force ripple and both are desirable

in positioning applications, they are antagonistic (faster operation requires higher forces, higher currents and more heat); trade-offs are expected to exist in seeking positioning solutions. This will be considered further in Chapter 4.

The results of this chapter represent improvements in optimal commutation as it relates to the point-to-point positioning problem. Common optimal commutation goals in the literature include maximizing force and minimizing power dissipation (from copper losses) or minimizing force ripple while producing a given force value. A large body of research on excitation to minimize ripple so as to produce smooth force or torque dominates the literature ([49]-[58]). With few exceptions, in all published research on optimum excitation of linear and rotary VR motors, assumptions are made a priori on the positions (or angular positions) for turning a phase on or off (based on the slope of the inductance curve and the desired direction of force) and on the number of phases that can be excited simultaneously. Multiple-phase excitation is studied, but still under the turn-on turn-off assumptions in [59] where two-phase excitation is found to result in reduced peaks and reduced rates of change of currents resulting in reduced ripple and reduced normal force (more important for single sided motors where normal force is not balanced).

Minimization of average power dissipation has been examined in [60] and [61] without a priori assumptions for rotary variable reluctance motors and the results apply to the uncoupled motor (Figure 7 (b)). Both maximization of force production and minimization of copper losses without a priori assumptions are reported in [62]; however, the formulation of these problems assumes current sources as controls without any consideration of voltage limits. The optimal commutation in this research is determined without any a priori assumption and in a general framework that is not limited to use with the idealized models.

This research differs from these publications and other published research in redefining the commutation problems to include force ripple specification. Covering the

complete range of force-ripple values from no ripple (smooth force) to unconstrained ripple, gives rise to additional choices of motion trajectories and the excitation currents necessary for tracking them.

CHAPTER 4

POINT-TO-POINT POSITIONING CONTROL ASSESSMENT

4.1 Introduction

The purpose of this chapter is to demonstrate improvement in actuator performance, measured by settling time, in single-axis point-to-point positioning applications and to describe the framework that has been developed for that purpose. This framework then remains as a tool to be used for finding and assessing positioning task solutions. The development of the control system design and simulation software are described, and the settling time results from several positioning simulations are presented and compared to predictions. In order to examine the trade-off between fast operation and cool operation, the associated average power dissipation results are also shown. The implementation of the framework presented here employes idealized LVR motor models and associated optimal commutation results. First, to aid in the presentation, a brief description of the physical limitations relevant to point-to-point motion control is presented.

4.1.1 Physical Limitations in Point-to-Point Positioning

It is necessary, in order to ensure the feasibility of positioning solutions, to account for physical limitations in motion control design. Consider, for example, the issue of trajectory generation: the optimal motion trajectory that minimizes the cycle time for point-to-point positioning implies that productivity would be maximized if each move is performed at the maximum possible acceleration for half the motion time and at the maximum possible deceleration for the other half, but obviously, this cannot

practically be achieved. To address this, minimum-time s-curve trajectories, which account for physical limitations on positioning, provide the reference commands in the point-to-point positioning control system. Positioning performance limitations are discussed next, and parts of the control system they influence are indicated. For context, the major parts of the control system are shown in Figure 55.

4.1.1.1 Temperature Limit

Motor capability is ultimately determined by temperature limits. A motor used for periodic motion is associated with periodic currents whose RMS values determine average power dissipation and temperature rise. Temperature rise has to be limited to protect coil insulation. The constraints on temperature rise and the steady state temperature for periodic motion when considering copper losses have been shown in [53] to be equivalent to constraints on average power dissipation. For the purposes of this research, the control system employs the heat-minimizing excitation currents (Chapter 3) to impose commanded forces. Post processing of dynamic system simulation results, with the knowledge of the current waveforms, is used to evaluate average power dissipation according to (151) for trade-off analysis.

There are other sources of heat that have not been considered. Power dissipation associated with friction is not computed (but friction forces are included in simulations); core (hysteresis and eddy current) losses have not been modeled. In low speed operation of VR motors, copper losses dominate while in high speed operation, core losses dominate. In [40], eddy current losses are found to dominate core losses in the LVR motor and were reduced (as is generally the case) by using lamination whereas hysteresis losses were found negligible except with a very small air gap. Eddy currents are also mitigated [15] because of the longitudinal (as opposed to transverse) flux design (see Section 1.2.5 for a definition of these terms). Inclusion of all heat sources would enhance the results of this research by computing more precisely the penalty

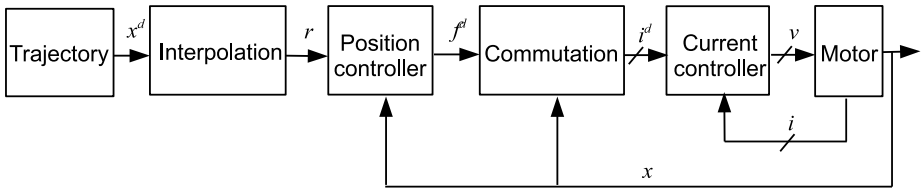

Figure 55: Control system main components.

for improved performance; however, the primary result pertaining to higher ripple, higher force production and associated faster positioning capability is unaffected.

It is also reasonable to expect that the impact on the final outcome of this research from not having an accurate numerical value for these additional losses is less significant compared to copper losses because major factors influencing these additional losses remain unchanged between any two compared scenarios; the magnetic material used, the flux saturation density, where localized magnetic saturation occurs (at the teeth) and friction modeling all remain the same.

4.1.1.2 Voltage and Current Limits

The converter that drives the motor imposes a phase voltage limit. This limit influences the motor's maximum achievable force and the shape of excitation waveforms needed for producing any feasible force value; therefore, it has been taken into consideration in computing the force-speed capability curves and the heat-minimizing current waveforms presented in Chapter 3. Through its influence on force-speed characterization, voltage limit influences parameters (namely maximum acceleration and maximum speed) needed in position reference signal generation; through its influence on excitation design, it influences current computation in response to commanded forces during controlled operation and average power dissipation computation for each positioning task.

The converter that drives the motor imposes a phase current limit, but this limit is usually very high and can be handled through converter over-current protection devices. The motor coils also impose limits on the heat which can be interpreted as

a limit on instantaneous phase current values. However, imposing RMS or average power dissipation limits (or as in this research monitoring and recording them as a performance cost) is preferred to relying on instantaneous current because the optimization freedom added by considering the whole periodic waveform can be exploited to allow higher average force production.

4.1.1.3 Speed, Acceleration and Jerk Limits

The time-optimal s-curve model [1] used in generation a position trajectory for a given travel distance ξ requires, as input parameters, a maximum speed $S_{\max}$, a maximum acceleration $A_{\max}$ and a maximum jerk (time derivative of acceleration) $J_{\max}$. These limits may be determined by the most restrictive of several possible factors. For example, limits on jerk (which is qualitatively indicative of motion smoothness) may stem from mechanical considerations (such as vibration or wear-and-tear), the sensitivity of payload to jerk or other concerns related to the time rate of change of force.

Positioning tasks require actuators to provide the force necessary for tracking the trajectory, and so it is necessary to ensure that the force-speed capability of the selected actuator and the trajectory input parameters are appropriately related. Given any requirements, such as space considerations and cost (power dissipation is examined post simulation in this research), an actuator with the highest possible force (acceleration) capability that meets these requirements is most attractive for fastest positioning. Therefore, a limit on acceleration specified by the application represents a limit on actuator force capability requirements and influences the choice of actuator (selected actuator should not be over-sized for the task). The LVR motors characterized in Chapter 3 are used for the example positioning tasks presented in this chapter. The manner in which position control, actuator force-seed capability and trajectory generation parameters are related for the purposes of this research is

explained in Section 4.3.

4.1.1.4 Cycle Time and Power Dissipation Limits

The application specification may include a limit on cycle time (equivalently a limit on settling time) based on productivity goals and/or a limit on temperature rise (equivalently a limit on average power dissipation) possibly for additional reasons beside the integrity of motor coils. For the purposes of this research, these limits are considered post simulation criteria that may be used to influence the final choice of a positioning solution (motor, excitation and control combination).

4.1.1.5 Structure Vibration Reduction

Additional limitations on the achievable positioning performance may be imposed specifically because of the need to suppress residual vibration; for example positioning trajectories may need to be modified (via command shaping); controller gains may need to be reduced and additional cost may be incurred (to structurally stiffen and dampen positioning system structures). Vibration is not investigated in this research, but encouraging insight that motivates further numerical and/or experimental studies to quantify and address the influence on structure vibration of the proposed non-conventional high-ripple excitation strategy has been gained from the select publications discussed briefly in the introductory chapter.

Measures to suppress vibrations in a coupled LVR motor that are compatible with the high-force-ripple strategy in this research are reported in [66]. First, control bandwidth is reduced only towards the end of motion (resonance frequencies are found to be within the control bandwidth that is desired for fast positioning). It is noted at the same time that residual vibration is likely easier to eliminate once a move is completed (it is difficult to achieve rapid motion without deflection and vibration even with sophisticated control [67]). This suggests that exploiting the freedom from strict

trajectory tracking before reaching the target position in generating faster trajectories (by using higher force ripple and hence higher force limits) may be combined with vibration reduction strategies that would preserve the predicted performance improvements. Second, only the magnitude of the normal force at the completion of motion is critical for improved stiffness and is addressed through switched excitation that provides the desired normal and lateral force with no restrictions on the ripple content of the lateral force. Third, the passive anti-vibration method used does not contradict the high-force-ripple commutation strategy of this research (the method reported involves bearings that are mounted on the translator via mechanical dampers and contact the stator so that stator vibrations are transmitted to the bearings and dissipated in the dampers).

Successful implementation of command shaping (i.e. the use of trajectories that will not excite the resonances of system structures) in [68] and [69] to achieve vibration suppression by modifying optimal or sub-optimal position reference trajectories like those in this research provides more insight. These publications do not implicate force ripple in the applied motive force in generating vibrations; in fact, when optimal or sub-optimal trajectories are modified (by changing the harmonic spectrum of the force command) for the purpose of suppressing residual vibration, the resulting commands do not preserve the constant (flat) segments at maximum positive or negative force but rather appear as if an oscillatory disturbance force has been intentionally added to them! This suggests that force ripple (or oscillations about commanded force values) is not categorically detrimental; it further suggests that command shaping may be incorporated during optimal static commutation by including vibration suppression objectives or constraints (targeting resonance frequencies expected for the closed loop system). Preliminary research on LVR motor commutation showed obvious variation in the shape of force (and force-ripple) waveforms based on the index selected for controlling force ripple in the motor force. Finally, position control design

and command shaping may be addressed concurrently (one method is discussed in [70]) in search for minimum settling times.

4.2 Framework for Positioning Control Assessment

The framework that has been developed for demonstrating improvement in positioning performance and offering a prescription for finding and assessing positioning task solutions is now described. The objective is to facilitate the evaluation of multiple scenarios of a point-to-point positioning task in order to provide the data necessary to assess positioning performance and ascertain the possibility of predicted improvements in performance with higher ripple (and hence higher force). The framework, which is depicted graphically in Figure 56, integrates the major (interdependent) factors influencing point-to-point positioning:

- Actuator ripple-specified characterization and optimal static commutation
  - Determination of achievable force based on ripple-specified optimal force-speed capability (used in identifying feasible trajectories as well as actuator saturation limits used in position control simulations)
  - Computation of ripple-specified heat-minimizing phase currents (to be recalled by the control system indexed by position and desired force)
- Position control design and simulation
  - Determination of feasible position trajectories (based on ripple-specified optimal capability and task specifications)
  - Commutation (transforming position-controller force commands into phase current commands using lookup tables populated by heat-minimizing phase currents)
  - Position control performance assessment via feedback control system simulations and comparison to predictions

– Examining trade-offs

In general, a positioning solution comprises an actuator of appropriate force capability, a motion trajectory, a control system and a power electronic converter (and implicitly meets other requirements such as cost, space or environmental limitations). In this research, actuator and force capability choices are limited to the coupled and uncoupled motors and their force-speed curves generated in Chapter 3. Potential positioning solutions are identified by generating a set of minimum-time feasible trajectories based on the available force and task specifications (and other underlying limitations), and are evaluated via closed loop control simulations that produce actual settling times and associated average power dissipation. The existence of multiple solutions (associated with multiple minimum-time s-curve trajectories) permits comparisons to ascertain the claims made in this research, but in addition it serves the general purpose of selecting (or discarding) a solution based on a specified upper bound on cycle time (equivalently on settling time τ_s) and/or an upper bound on temperature rise (equivalently on average power dissipation P):

$$\begin{aligned} \tau_s &\leq T^d \\ P &\leq P^d \end{aligned}$$

Numerical studies are designed such that these bounds may be examined post simulation. Implementation of this framework has been achieved using code written in MATLAB and summarized as the four-task algorithm depicted in pseudo code in Figure 57. The implementation in this chapter employes the idealized models (ignoring magnetic saturation and spatial harmonics) of LVR motors and the associated optimal commutation results. However, the general framework is not limited to the motors and models chosen in this dissertation or linear motors only.

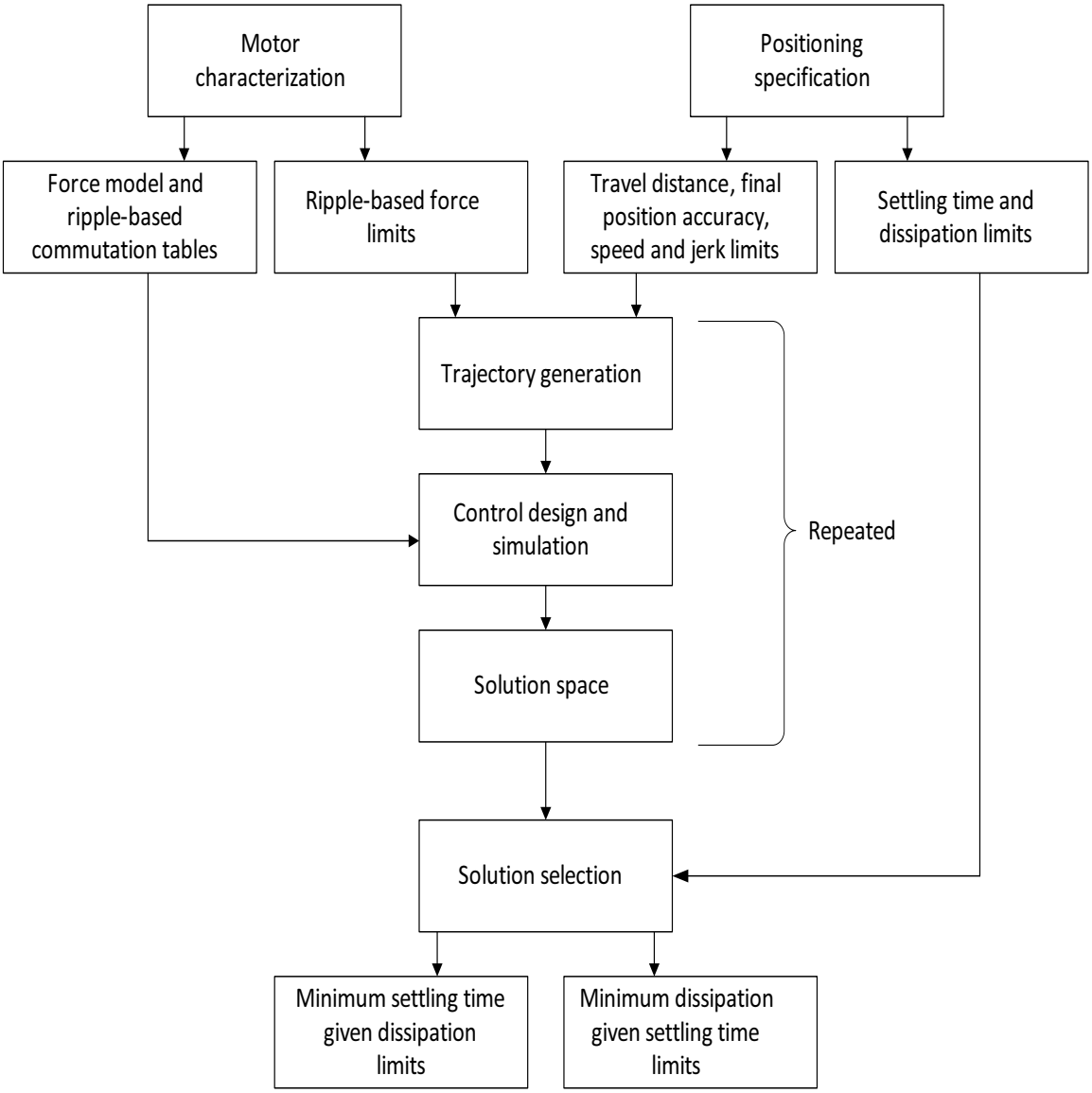

Figure 56: Framework for point-to-point positioning solution selection.

4.3 Feasible Trajectories and Nominal Travel Times

Point-to-point positioning has been introduced in Chapter 1. It has been mentioned that in applications such as circuit board assembly, it is possible to plan multi-axis motion separately for each axis thus simplifying the control problem. The principal positioning task then is for an actuator to move a single mass M in a single axis from a starting position x_i to a final position x_f as fast as possible, yet meet final-position error tolerance Δx (recall Figure 6); in summary

$$\text{Principal Task Specifications:} \quad \begin{cases} \text{Moving Mass} & = M \\ x_f - x_i & = \xi \\ |x(t)_{t \geq t_s} - x_f| & \leq \Delta x \end{cases} \tag{201}$$

When the desired positioning points are known a priori, and the workspace is clear of obstacles, optimized (fastest) motion trajectories can be stored and executed repeatedly in a predetermined sequence. Minimum-time s-curve trajectories are pursued in order to provide the fastest motion commands subject to realistic motion constraints. The parameters needed in generating an s-curve trajectory (first introduced in Chapter 1) are specified in terms of the travel distance ξ and the limits of trajectory speed $S_{\max}$, acceleration $A_{\max}$ and jerk $J_{\max}$:

$$\text{Minimum-Time S-Curve Specifications:} \quad \begin{cases} x_f - x_i & = & \xi \\ |\dot{x}| & \leq & S_{\max} \\ |\ddot{x}| & \leq & A_{\max} \\ |\dddot{x}| & \leq & J_{\max} \end{cases} \tag{202}$$

The trajectory parameter limits are dictated by the application task (201) and by the actuator. Focusing on the LVR motor as the actuator of choice, the force (acceleration) capability is defined by the ripple-parameterized force-speed curves derived

in Chapter 3. Namely, the solutions to the force maximizing commutation problem (185)–(188) provide matched (force capability limit, speed) pairs for use in trajectory generation. These solutions are summarized by relations of the form $f^*_{\text{avg}}(\dot{x}, \beta)$ or alternatively by the ripple-specified force-speed curves in Figure 48 (coupled motor) and Figure 49 (uncoupled motor). The manner in which a (force capability limit, speed) pair is determined is explained next with the help of Figure 58 in which a generic optimal force-speed curve is shown.

4.3.1 Operation Limits

Assume that for some positioning task scenario the maximum speed parameter $S_{\max}$ has been fixed by the application, and consider an actuator choice (specifically, an optimal force-speed curve of the chosen motor with a chosen ripple size $\beta = \beta^*$). The optimal force-speed curve is examined to determine a subregion to which motor operation is limited (negative forces included but not shown in Figure 58). The force value f^*_{avg} that corresponds to $\dot{x} = S_{\max}$ is the highest force value achievable at the maximum trajectory speed (and also achievable at all lower speed values along the trajectory) and represents the maximum force to be commanded of the motor. This means that, although actuators generally have increasing force capability with decreasing speed, motor operation conforms to adopting minimum-time s-curve trajectories (gradual acceleration to $A_{\max}$, or equivalently $f^*_{\text{avg}}(\dot{x} = S_{\max}, \beta = \beta^*)$, at the trajectory's maximum speed before gradual deceleration in a similar manner), thus excluding points on the capability curve that corresponds to either higher speed magnitudes than $S_{\max}$ or force values that are not available at all speeds along the trajectory.

Recalling Figures 48 and 49, it can be seen that a single value of $S_{\max}$ may be matched with multiple average force capability limits $f^*_{\text{avg}}(\dot{x} = S_{\max}, \beta \in [0, 1])$, distinguished by ripple size. Once ripple size is also fixed to some value β^*, the force

limit F for trajectory generation can be set to a value within the motor capability limit ($F \leq f^*_{\text{avg}}(\dot{x} = S_{\max}, \beta = \beta^*)$), but for the fastest trajectory the logical choices for force and acceleration limits are

$$F = f^*_{\text{avg}}(\dot{x} = S_{\max}, \beta = \beta^*) \tag{203}$$

$$A_{\max} = F/M \tag{204}$$

Note that for any positioning scenario, the same F value is used in specifying both $A_{\max}$ for trajectory generation and the actuator's saturation limit (denoted $U_{\max}$ in control design) for position control purposes. It is assumed that no lower limit on acceleration is imposed; there is no loss of generality because if some application requires a limit on acceleration that is lower than suggested in (204) then $A_{\max}$ must be set to the lower limit for trajectory generation and the motor can either be replaced, operated according to a different capability curve or operated with an artificially lowered saturation limit. In implementation and as indicated in the software description of the following section, the force limit is modified to account for (approximated) friction and the mass is modified to account for the payload. A choice of $J_{\max}$, which is taken as a given parameter dictated by the application, completes trajectory specification.

4.3.2 Trajectory Space

A feasible-trajectory space can be generated, for a given positioning task, from permutations of interdependently feasible values of the parameters in (202). Each permutation when input into a minimum-time s-curve model [1] results in a feasible trajectory featuring a selected force-speed curve and trajectory parameters that are related as just described. The required steps are summarized by Task 2 in Figure 57. The corresponding nominal travel times are then found using (14). The resulting trajectories are saved for use by the control system (giving the position reference) and the nominal travel times are saved for later comparison to actual settling times.

It is of interest to note that setting trajectory force limit to the actuator's force

limit F implies that force values up to F may be commanded by the control system during dynamic operation in order to enforce position reference tracking, but (by excitation design), the currents computed to produce any force value produce that force value on average. This implies that even when the force command issued by the control system is held constant, that command is transformed into current commands that (except for the ideal case of 0 ripple and perfect control) are not designed to produce constant force; therefore it is expected to see ripple in the output force waveforms.

An example is now given showing the generation of a feasible trajectory space. The example helps visualize the size of the problem space (trajectory space) and the size of the associated solution space (to be computed from complete control system simulations). Let it be assumed that the various motion variables are limited to those shown in Table 12 where the two available actuators have been modeled and characterized in Chapters 2–3. According to the force-speed curves (Figures 48 and 49), each motor provides 11 levels of force capability distinguished by the ripple size parameter β, at any specified speed; the choice of 11 levels is for computational convenience. This means that, for each possible speed limit value, up to 22 trajectories can be generated for simulation and analysis.

Table 13 shows the feasible-trajectory space for the motion variables listed in Table 12 and the motors defined in Table 1 with $\beta = 0, 1$ (the positioning task is defined by $\xi = 500$ mm, $J_{\max} = 1000$ m/s^3, $\Delta x = 10\,\mu$m, and a payload of 10 kg). Graphical depictions of the trajectories are shown in Figures 59–62. In Table 13 the column labeled p is a scenario identifier referenced later in Section 4.6 when comparing actual settling times to nominal (predicted) values. Note that the nominal travel time ($\tau_n = t_f - t_i$) of a trajectory is different from the actual settling time ($\tau_s = t_s - t_i$), but it represents a lower bound on settling time (one that would be achieved with perfect control); an additional interval of active settling time ($\tau_a = t_s - t_f$) is inevitable under

% This algorithm is implemented with both coupled and uncoupled motors
% Task 1: motor characterization
for various values of β
  for various values of $\dot{x}$
    F=solve the optimal commutation problem (185)–(188)
    store F
  end
end

% Task 2: Feasible trajectories for positioning task: $\xi, J_{\max}, S_{\max}, M$
for select values of β
  for select values of $S \leq S_{\max}$ and $J \leq J_{\max}$
    FileName='TrajectoryID'
    $F = f^*_{\text{avg}}(S, \beta)-$ max(static, coulomb, viscous friction)
    M = MotorMass + Payload
    $x^d(t)$ = Generate Trajectory (ξ, J, S, F, M)
    $\tau_n = t_f - t_i$
    save($x^d(t), \tau_n$, FileName)
  end
end

% Task 3: Current waveforms for mesh of ripple-specified force values
for selected $\dot{x}$ and β
  FileName='TableOfCurrents' % to add to currents database directory
  for $F = 0 : \text{step} : f^*_{\text{avg}}(\dot{x}, \beta)$
    (I_1, I_2, I_3, $\mathcal{X}$, F) = solve (192)–(196)
    append(I_1, I_2, I_3, $\mathcal{X}$, F, FileName)
  end
end

% Task 4: position control results and performance data
for various feasible trajectories
  simulate controlled positioning
  store settling time τ_s and average power dissipation P
end

Figure 57: Four-task algorithm for implementing the framework of Figure 56.

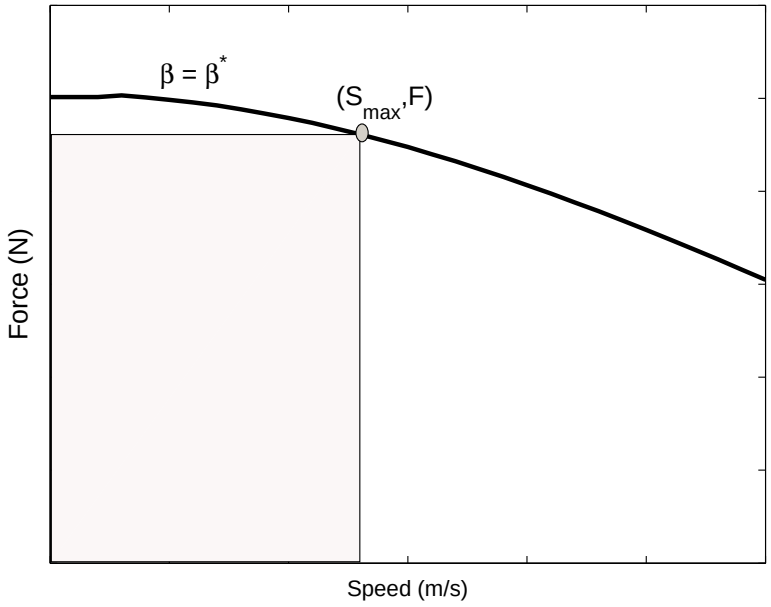

Figure 58: Motor operation limits.

realistic control. If more permutations on jerk and speed within their specified limits are considered, then the number of feasible trajectories increases accordingly.

4.3.2.1 Redundant Trajectories

It is possible because of the interdependence of s-curve parameters (travel distance, and maximum values of jerk, acceleration and speed) that multiple permutations on these parameters produce redundant (identical) trajectories. For example, the achievable trajectory speed (influenced by the remaining s-curve parameters) may be lower than the specified limit (as allowed by the application); in this case no new (unique) trajectories will result by inputting higher speeds than achievable while the remaining parameters are kept the same.

4.4 Heat-Minimizing Phase Current Waveforms

During point-to-point control operations the control system requires a certain amount of force from the motor. Consequently a determination of phase current values to

Table 12: Motion Variables for Feasible Trajectory Generation

Motion Variable	Possible Choices
β	$1, 0.9, 0.8, \ldots 0$
$J_{\max}$ (m/s^3)	1000
$S_{\max}$ (m/s)	1,2,3
M (kg)	10
ξ (mm)	500

produce that force is required. The solutions to the heat-minimizing commutation problem (192)–(196) for a desired average force value produce heat-minimizing current waveforms (I_1, I_2, I_3) covering the spatial period of excitation X where $X = p_t$ for the uncoupled motor and $X = 2p_t$ for the coupled motor. A corresponding set of displacement values covering a period of excitation is also saved (recall that force is a function of current and displacement). Each phase current waveform is an array of current values that correspond (one-to-one) to the values in an array of displacement values $x : 0 \leq x \leq X\}$. A database of excitation waveforms is built by computing such waveforms for a mesh of average force values within motor's force capability, but since motor capability is a function of speed and ripple, each set of waveforms is stored and tagged with a speed value and a ripple value. During operation, all current waveforms in a lookup table are based on maximum trajectory speed assumption to ensure voltage constraints are not violated; pursuing cooler operation by exploiting the available voltage at lower speed is conceivable, but would require storing excitation currents with a speed index in addition to force and position indices.

Database generation steps are summarized by Task 3 in Figure 57. Current waveforms for only positive force values are stored because simple logic can be employed in deriving current values associated with the production of a negative average force. The database would be used for dynamic operation as explained below.

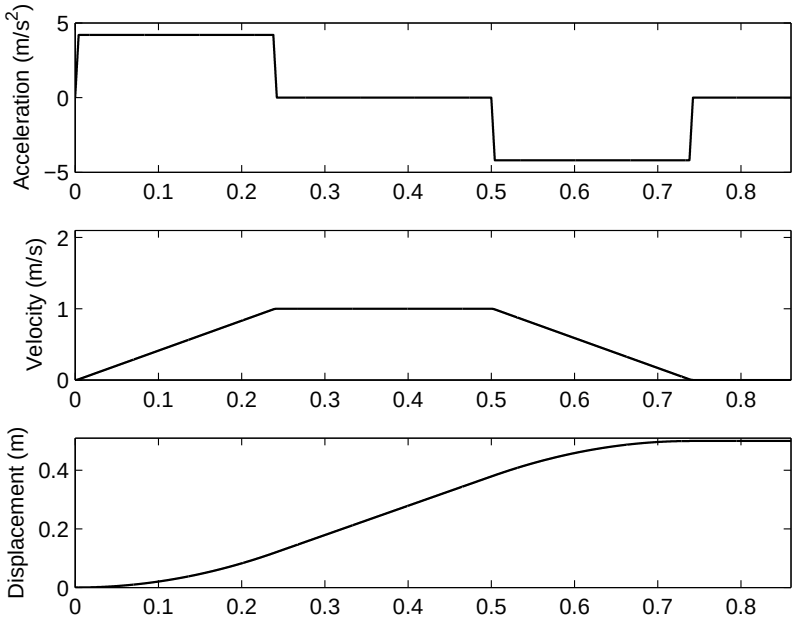

(a) No ripple.

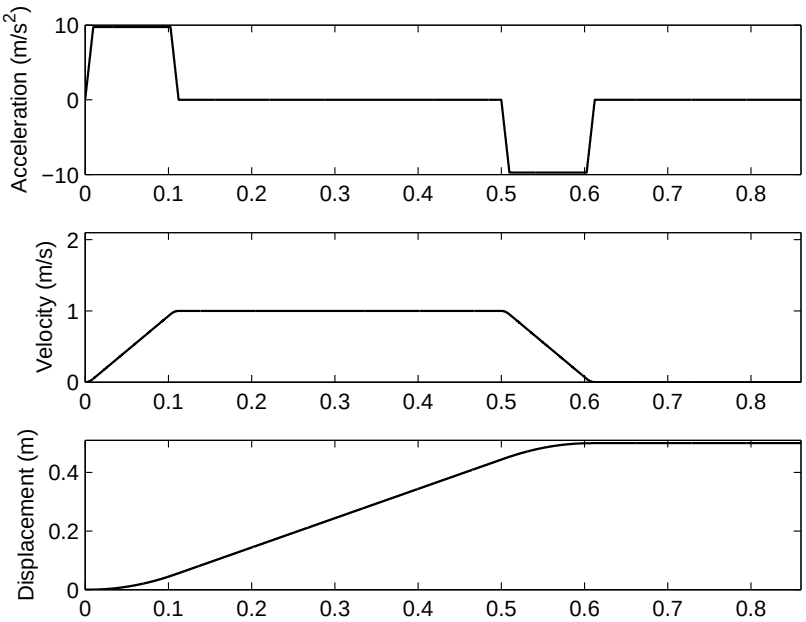

(b) High ripple.

Figure 59: Position trajectories using the uncoupled LVR motor with $\dot{x}_{\max} = 1$ m/s.

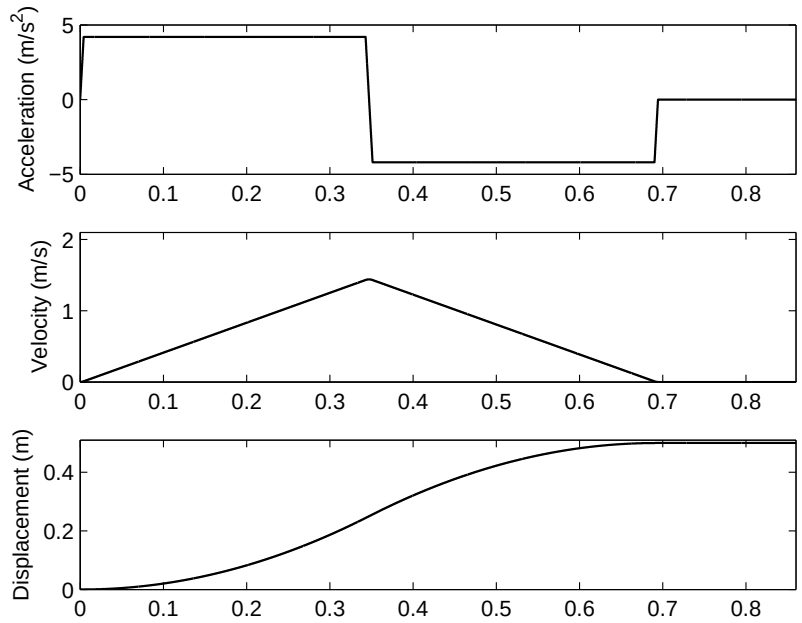

(a) No ripple.

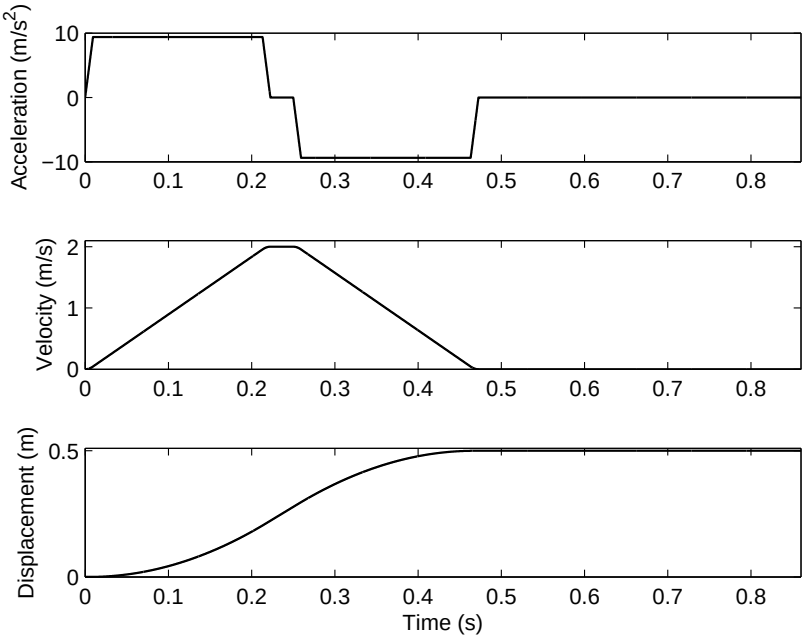

(b) High ripple.

Figure 60: Position trajectories using the uncoupled LVR motor with $\dot{x}_{\max} = 2$ m/s.

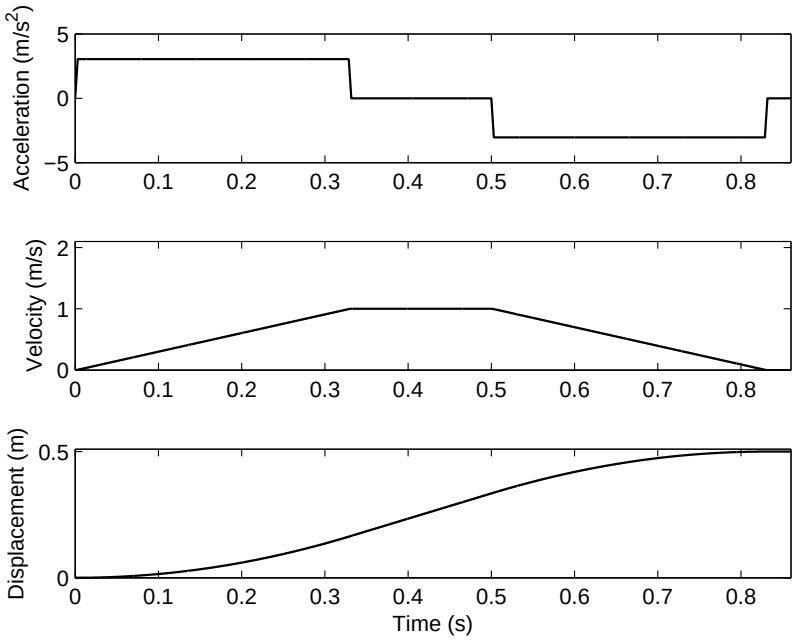

(a) No ripple.

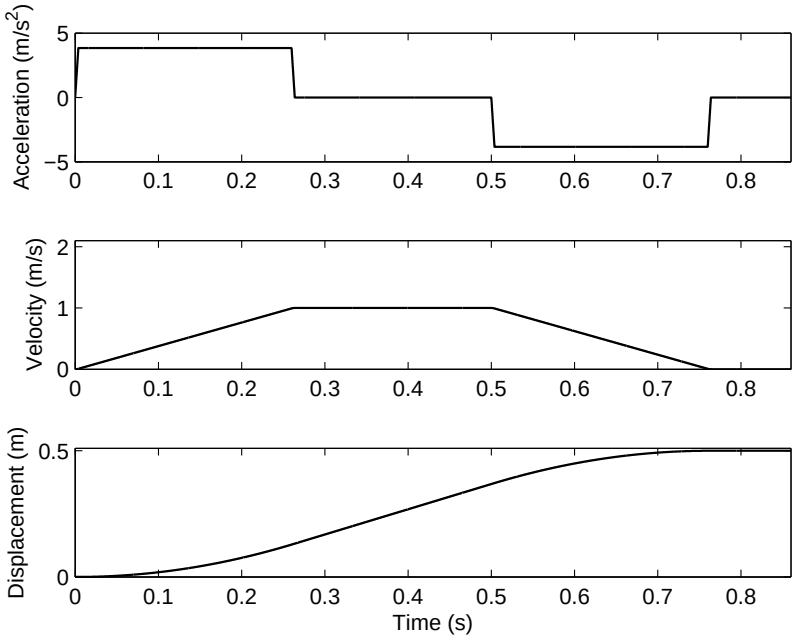

(b) High ripple.

Figure 61: Position trajectories using the coupled LVR motor with $\dot{x}_{\max} = 1$ m/s.

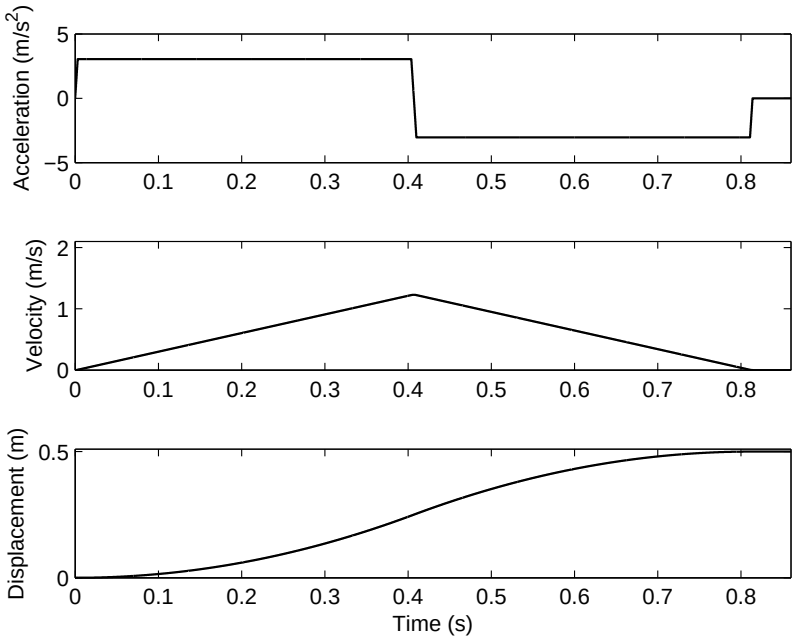

(a) No ripple.

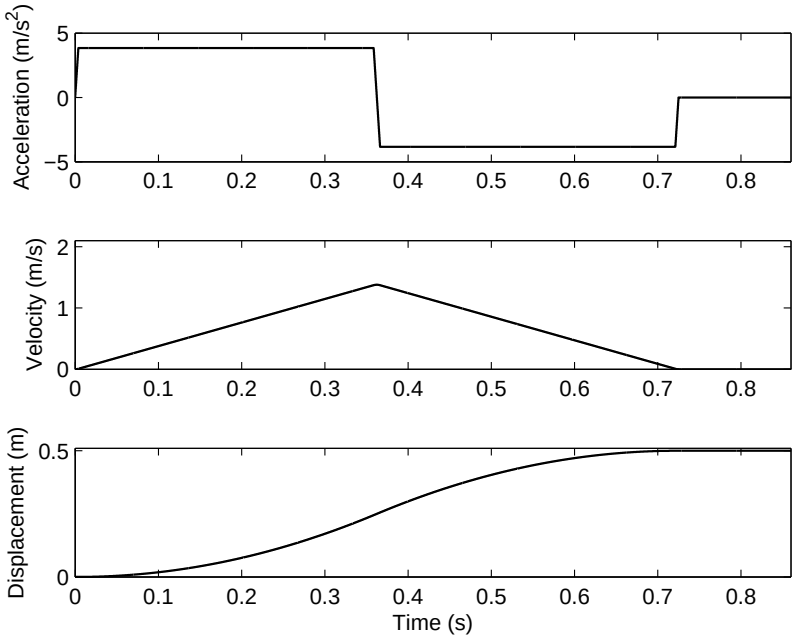

(b) High ripple.

Figure 62: Position trajectories using the coupled LVR motor with $\dot{x}_{\max} = 2$ m/s.

4.4.1 Force-Position-Current Lookup Tables

The modeling sections in Chapter 2 showed single valued force functions with current and position as independent variables; however, the reverse problem (the determination of phase current values to produce a commanded force) is much harder. There are no analytical expressions to find phase currents as functions of force and position. A convenient way to overcome this difficulty is to approximate the needed phase j current function by a table consisting of a finite number of phase j current values covering a spatial period of excitation arranged as illustrated by Figure 63 so that the row and column numbers indicate position and average force values (implicitly each table corresponds to a speed value and a ripple value used in current computation). The finite number of table entries is determined by the densities of the position and force grids; naturally, there has to be a compromise between accuracy (denser is better) and computational effort (sparser is better).

Suppose that during operation the magnitude of the desired force at position x is $|u|$; then the phase currents i_j^p that produce a positive force of magnitude $|u|$ and the phase currents i_j^n that produce a negative force of magnitude $|u|$ are found using

$$i_{1,2,3}^p = \text{interp}(\text{TableOfCurrents}(I_1, I_2, I_3, |u|, x_p, \text{method} = 'linear') \quad (205)$$

$$i_{1,2,3}^n = \text{interp}(\text{TableOfCurrents}(I_1, I_3, I_2, |u|, x_n, \text{method} = 'linear') \quad (206)$$

where

$$x_p = \text{mod}(x, X) \quad (207)$$

$$x_n = X - x_p \quad (208)$$

where, as defined before, the spatial period of excitation is given by $X = p_t$ for the uncoupled motor and $X = 2p_t$ for the coupled motor. In the context of position control design, this mapping from desired force and position to desired phase currents constitutes the commutation subsystem that produces reference commands for

a current controller. Position control is achieved by closing a control loop around the commutation subsystem.

4.5 Control System for Point-to-Point Positioning

Figure 64 shows the control system in more detail. Modeling details, description of the different components, control design and implementation are addressed next.

4.5.1 Design and Simulation Models

Position control design in this chapter employs a linear plant model that captures basic plant behavior while simplifying control design. The input labeled w in Figure 64 represents disturbance forces consisting of nonlinear friction forces (see Section 4.5.6) that are included in the simulation of plant physics, but are not included in the control design model (only viscous friction is included in the design model). There are additional phenomena taken into consideration in the position control simulations of this chapter, such as saturation effects and quantization effects.

4.5.2 Position Reference

Underlying the control structure (Figure 64) is a common practice [51] of planning motion before designing a control system for it, i.e. a motion trajectory (or a model to compute it online) exists and provides the position reference r at any time during dynamic operation. This is part of a modular approach to solving point-to-point positioning problems while observing the interdependence of the different parts of the solution. Generating a trajectory $x^d(t)$ has been discussed in Section 4.3; the position reference during simulation is given by

$$r(t) := x^d(t) \tag{209}$$

4.5.3 Dynamic Model

The idealized flux and force models used in this chapter have been presented in Chapter 2. Once flux linkage and force models are known, the dynamic model can be established including the dynamics of both the mechanical and the electrical subsystems. Starting with the electrical subsystem, the three phase voltages are given by

$$v_j = Ri_j + \frac{d\lambda_j}{dt} \quad , j = 1, 2, 3 \tag{210}$$

where R, the resistance, is assumed the same for all three phases. The flux linkages, currents, and voltages can be compactly written in vector form

$$\lambda = \begin{bmatrix} \lambda_1 \\ \lambda_2 \\ \lambda_3 \end{bmatrix}, i = \begin{bmatrix} i_1 \\ i_2 \\ i_3 \end{bmatrix}, v = \begin{bmatrix} v_1 \\ v_2 \\ v_3 \end{bmatrix} \tag{211}$$

The mechanical system dynamics, described by Newton's Law, complete the dynamic model:

$$\frac{dx}{dt} = \dot{x} \tag{212}$$

$$\frac{d\dot{x}}{dt} = M^{-1}\left(f(x,i) - f_f(x,\dot{x})\right) \tag{213}$$

$$\frac{di}{dt} = \frac{\partial\lambda(x,i)}{\partial i}^{-1}(x,i)\left(v - Ri - \frac{\partial\lambda(x,i)}{\partial x}(x,i)\dot{x}\right) \tag{214}$$

where x represents the position, M the total moving mass, $\dot{x}$ the velocity, i the phase currents, v the phase voltages, λ the flux linkages (the partial derivatives of flux with respect to currents are incremental inductance functions and with respect to position are back-emf functions), f the motor's force and f_f viscous friction force (additional friction force components are treated as disturbance forces, seen as the input labeled w in Figure 64 and are included in system simulation).

Table 13: Feasible Trajectory Tabulation, Task: $\xi = 500$ mm, $J_{\max} = 1000$ m/s^3, Load = 10 kg

p	Motor	β	$S \leq S_{\max}$ (m/s)	$F \leq f^*_{\text{avg}}(S, \beta)$ (N)	File Name	τ_n (s)
1	Uncoupled	1	1	145	U_1_1_U.dat	0.61223
2	Uncoupled	1	2	140	U_1_2_U.dat	0.47248
3	Uncoupled	1	3	130	U_1_3_U.dat	0.47248
4	Uncoupled	0	1	70	U_0_1_U.dat	0.74227
5	Uncoupled	0	2	70	U_0_2_U.dat	0.69426
6	Uncoupled	0	3	70	U_0_3_U.dat	0.69426
7	Coupled	1	1	60	C_1_1_C.dat	0.76385
8	Coupled	1	2	60	C_1_2_C.dat	0.72497
9	Coupled	1	3	60	C_1_3_C.dat	0.72497
10	Coupled	0	1	50	C_0_1_C.dat	0.83174
11	Coupled	0	2	50	C_0_2_C.dat	0.81386
12	Coupled	0	3	50	C_0_3_C.dat	0.81386

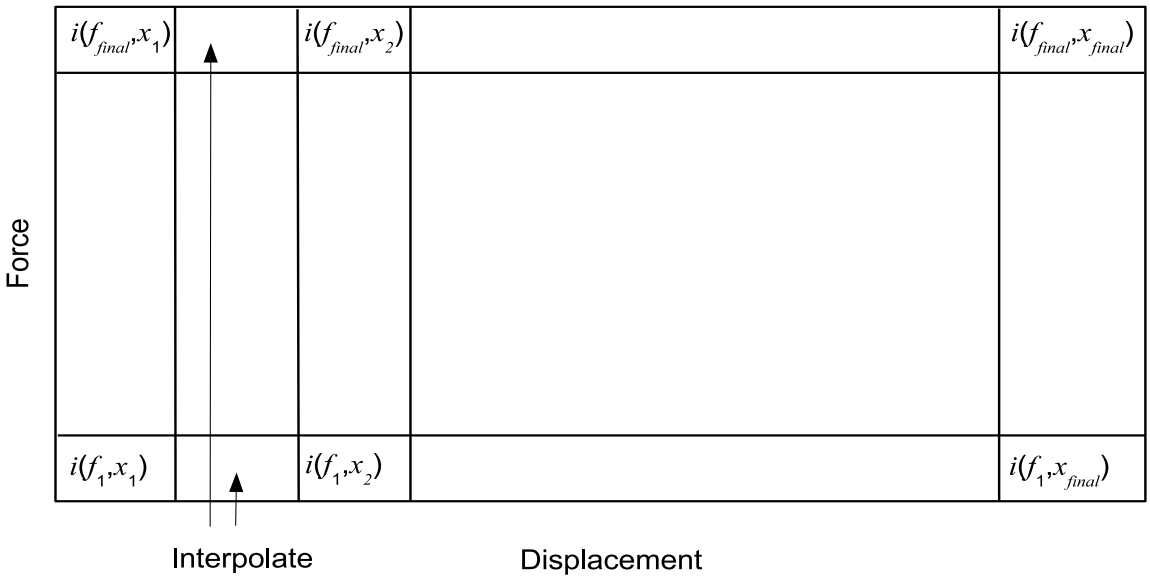

Figure 63: Phase current lookup table populated from heat-minimizing-current database.

4.5.4 Position Control Design

Position control is achieved using state space integral control [91] and is implemented in the context of the overall control system structure shown in Figure 64. The implementation of this control system structure relies on a two-time-scale philosophy with a fast time frame for electrical dynamics and a much slower time frame for mechanical dynamics: it is assumed that position remains constant during the time frame of current response. This allows the design of the feedback position control to be independent of the electrical dynamics. An additional simplification of control design concerns disturbance forces. In particular additional (non linear) friction forces (that are considered in system simulation) are not included during control design. The physics-based plant model used for position control design will therefore be the mechanical subsystem (212)-(213).

The plant is a second order linear time invariant system with input u, representing the commanded actuator force, output y, representing the actual position, state vector $\mathtt{x}$, and constant coefficient matrices A, B, and C. The plant state vector components are position, $\mathtt{x}_1$, and speed, $\mathtt{x}_2$. The coefficient matrices are based on the physics-based plant model.

The control objective is to regulate the plant through the command u in order to provide reference-position following as well as internal stability and disturbance rejection. As can be seen by consulting the figure, the command u is a function of the integral of position error, controller gains (K_1 and K_2) and state estimates $\hat{\mathtt{x}}_1$ and $\hat{\mathtt{x}}_2$; speed could also be obtained by differentiating position in these examples (using state estimation becomes more important when amplification of sensor noise through differentiation is intolerable). The estimator used for computing $\hat{\mathtt{x}}_1$ and $\hat{\mathtt{x}}_2$ employs the plant model and a feedback gain L, and is shown in Figure 65 [91]. In summary,

the plant equation is

$$\dot{\mathtt{x}}(t) = A\mathtt{x}(t) + Bu(t) \tag{215}$$

$$y(t) = C\mathtt{x}(t) \tag{216}$$

and the estimator equation is

$$\dot{\hat{\mathtt{x}}}(t) = A\hat{\mathtt{x}}(t) + Bu(t) - L\left(C\hat{\mathtt{x}}(t) - y(t)\right) \tag{217}$$

The control signal input to the plant is given by

$$u(t) = -K_1\hat{\mathtt{x}}(t) - K_2\sigma(t) \tag{218}$$

where $\sigma(t)$, the position error integral, is defined by

$$\dot{\sigma}(t) = y(t) - r(t) \tag{219}$$

To obtain the coefficient matrices for control design purposes, the friction term in (213) is taken to be $F_v\dot{x}$ where F_v is the viscous friction coefficient (additional friction forces are treated as disturbance forces and included in system simulation). For notational convenience, let $a = \frac{F_v}{M}$ and $b = \frac{1}{M}$:

$$A = \begin{bmatrix} 0 & 1 \\ 0 & -a \end{bmatrix}, B = \begin{bmatrix} 0 \\ b \end{bmatrix}, C = \begin{bmatrix} 1 & 0 \end{bmatrix} \tag{220}$$

The control design parameters are the gains K_1, K_2 and L and are to be determined from the closed loop eigenvalues that satisfy desired transient response.

The control law and estimator states can be substituted into state equations to model the overall system. The states of the overall system are the original states, their estimates and the integrator output. However, when the estimator states are replaced by estimator errors, the overall system equations can eventually be partitioned to describe a regulator subsystem and an estimator subsystem for convenient computation of the closed-loop system eigenvalues. The estimator error $\varepsilon(t)$ is described

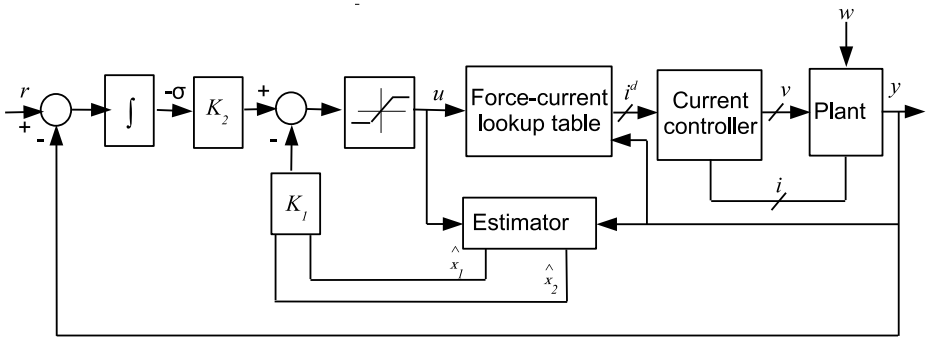

Figure 64: Control system.

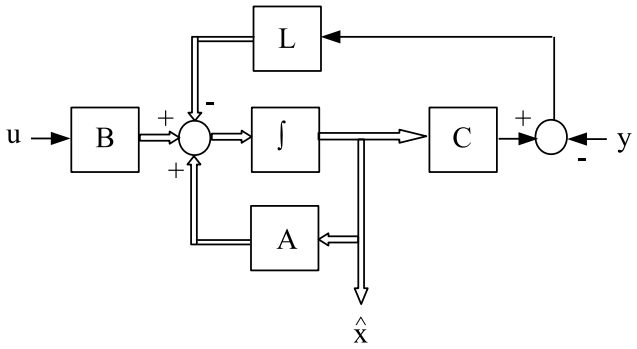

Figure 65: State estimator.

by

$$\varepsilon(t) = \hat{x}(t) - x(t)$$

After substituting and manipulating, the plant equation is

$$\dot{x}(t) = (A - BK_1)\, x(t) - BK_2\sigma(t) - BK_1\varepsilon(t),$$

and the estimator equation is

$$\dot{\varepsilon}(t) = (A - LC)\varepsilon(t)$$

The state and output equations of the combined estimator-state-feedback system are now given:

$$\left[\begin{array}{c} \dot{x}(t) \\ \dot{\sigma}(t) \\ \hline \dot{\varepsilon}(t) \end{array}\right] = \left[\begin{array}{cc|c} A - BK_1 & -BK_2 & -BK_1 \\ C & 0 & 0 \\ \hline 0 & 0 & A - LC \end{array}\right] \left[\begin{array}{c} x(t) \\ \sigma(t) \\ \hline \varepsilon(t) \end{array}\right] + \left[\begin{array}{c} 0 \\ -1 \\ \hline 0 \end{array}\right] r(t) \qquad (221)$$

$$y(t) = \left[\begin{array}{cc|c} C & 0 & 0 \end{array}\right] \left[\begin{array}{c} x(t) \\ \sigma(t) \\ \hline \varepsilon(t) \end{array}\right] \tag{222}$$

where the system has been partitioned [91] in order to separate the regulator and estimator subsystem. The top partition in (221) models the regulator states (position, speed and integrator output) and the bottom partition models the estimator states (position and speed estimation errors). Because of the block diagonal structure of the coefficient matrix in (221), the eigenvalues of the overall system are the union of the eigenvalues of the two subsystem matrices

$$\left[\begin{array}{cc} A - BK_1 & -BK_2 \\ C & 0 \end{array}\right]$$

and

$$[A - LC]$$

seen on the diagonal. For notational convenience let

$$\mathcal{A} = \begin{bmatrix} A & 0 \\ C & 0 \end{bmatrix}, \quad \mathcal{B} = \begin{bmatrix} B \\ 0 \end{bmatrix}, \quad \mathcal{K} = \begin{bmatrix} K_1 & K_2 \end{bmatrix}.$$

so that

$$\left[\begin{array}{cc} A - BK_1 & -BK_2 \\ C & 0 \end{array}\right] = \mathcal{A} - \mathcal{B}\mathcal{K}$$

As a result (after substituting A, B, C and the gains), the matrices that model each subsystem and the roots of their characteristic equations (the system eigenvalues) can now be given. The regulator subsystem is modeled by the matrices

$$\mathcal{A} = \begin{bmatrix} 0 & 1 & 0 \\ 0 & -a & 0 \\ 1 & 0 & 0 \end{bmatrix}, \mathcal{B} = \begin{bmatrix} 0 \\ b \\ 0 \end{bmatrix}, \mathcal{K} = \begin{bmatrix} K_{11} & K_{12} & K_2 \end{bmatrix} \tag{223}$$

The characteristic polynomial is given by

$$|sI - (\mathcal{A} - \mathcal{B}\mathcal{K})| = s^3 + (a + bK_{12})\, s^2 + (bK_{11})\, s + (bK_2) \tag{224}$$

If the closed loop system is desired to have its three roots at $s = -\lambda_r$ then the characteristic polynomial must satisfy

$$(s + \lambda_r)^3 = s^3 + 3\lambda_r s^2 + 3\lambda_r^2 s + \lambda_r^3 \tag{225}$$

and the regulator gains must be

$$K_{11} = \tfrac{1}{b} 3\lambda_r^2, \quad K_{12} = \tfrac{1}{b}\left(3\lambda_r - a\right), \quad K_2 = \tfrac{1}{b}\lambda_r^3 \tag{226}$$

Larger λ_r corresponds to faster transient response but also to large K_{11}, K_{12} and K_2 which could result in problems relating to actuator saturation limits; the selection of λ_r involves a trade-off between rate of response and control effort. The estimator subsystem is governed by the matrices A and L with characteristic polynomial

$$|sI - (A - LC)| = s^2 + (L_1 + a)\, s + (L_1 a + L_2) \tag{227}$$

If the estimator is desired to have its two roots at $s = -\lambda_e$ then the characteristic polynomial must satisfy

$$(s + \lambda_e)^2 = s^2 + 2\lambda_e s + \lambda_e^2 \tag{228}$$

and the estimator gains must be

$$L_1 = 2\lambda_e - a, \quad L_2 = \lambda_e^2 - 2a\lambda_e + a^2 \tag{229}$$

Larger λ_e corresponds to faster estimator, but also to large L_1 and L_2 which could result in problems relating to sensor noise amplification; the selection of λ_e involves a trade-off between rate of response and signal/noise ratio. A system, such as the one studied here, whose coefficient matrices are such that the roots of the characteristic polynomials can be placed as desired on the open left half plane is controllable and observable. The position controller is ready for implementation with the determination

of the gains that can now be substituted into the control law:

$$\begin{aligned} u(t) &= -K_1\hat{\mathbf{x}}(t) - K_2\sigma(t) \\ \dot{\hat{\mathbf{x}}}(t) &= A\hat{\mathbf{x}}(t) + Bu(t) - L\left(C\hat{\mathbf{x}}(t) - y(t)\right) \\ \dot{\sigma}(t) &= y(t) - r(t) \end{aligned}$$

4.5.5 Current Control

The desired phase currents (which are computed as described in the following subsection) are regulated using proportional control where the desired phase voltages are proportional to measured current errors, i.e.

$$v_j{}^d = k_i\left(i_j^d - i_j\right) \tag{230}$$

where i_j^d and i_j are respectively the desired and actual phase currents, v_j^d is the desired phase voltage and k_i is a positive feedback gain. Voltage saturation limits are observed and so the applied voltage is given by

$$v_j = \begin{cases} v_{\max}\,\mathrm{sign}(v_j^d) & ,\text{if } \left|v_j{}^d\right| \geq v_{\max} \\ v_j{}^d & ,\text{otherwise} \end{cases} \tag{231}$$

This formulation implicitly assumes a six-wire connection of the power converter (three separate H-bridge stages) for either the uncoupled or coupled motor.

4.5.5.1 Force-Current Mapping

Desired phase currents are determined by interpolation from lookup tables that map desired force to desired phase currents. The database from which the tables are populated is described in Section 4.4. The lookup tables are indexed based on displacement x and the magnitude $|u|$ of the desired force. The phase currents i_j^p that produce a positive force of magnitude $|u|$ and the phase currents i_j^n that produce a negative force of magnitude $|u|$ are found using (205) and (206) respectively. The

phase currents are determined according to the (if-then) logic below

$$i_j^d = \begin{cases} i_j^p & , u \geq 0 \\ i_j^n & , u < 0 \end{cases} \tag{232}$$

This describes the fundamental mapping from desired force and position to desired phase currents which constitutes the commutation subsystem that produces reference commands for the current controller. However, for improved implementation in the positioning examples presented in this chapter, this mapping is modified as described next.

4.5.5.2 Modified Force-Current Mapping

The force-current mapping described above is modified in the final implementation to facilitate a smooth transition between the cases of negative and positive force commands. This issue is particularly important to address at the end of motion where the force command approaches zero and could switch repeatedly between positive and negative values (causing phase current decision to switch between lookup for i_j^p and i_j^n); if the actual position exceeds the target position, the next force command is of the opposite sign in order to bring the motor back to desired position. Potentially, the positioning error and the corrective force command may cause persistent oscillations about the target position.

To avoid large variation in output force in response to a change in phase current commands and the potential for sustained oscillations, a smoothing function is employed as opposed to executing the lookup commands in (205)-(206) based on the if-then logic (232). Although both coupled and uncoupled motor phase currents are determined based on lookup tables from waveforms computed for only positive force production and although both motors are subject to the 'if-then' logic that leads to a rearrangement (any time the force sign switches) of indexing phase current and position in table lookup operations, the uncoupled motor is more affected: The stored

displacement-current waveforms for the uncoupled motor are pulsed in nature and the displacements where pulses should start and end change based on the commanded force magnitude and sign, can (apart from possible interpolation errors) contribute to jumps or shifts in the returned lookup results between consecutive lookup operations. The actual change in force in response to a current command change (which is sensitive to the slope of inductance at the time the currents are applied) may thus be undesirably large even when change in current command is not.

The smoothing function chosen is the mathematically convenient sigmoidal function

$$\mu_u = \frac{1.0}{1 + e^{-u/\delta}} \tag{233}$$

where δ determines the width of the transition band around $u = 0$. A depiction of this function is shown in Figure 66. The desired phase current is then obtained as

$$i_j^d = (1 - \mu_u) i_j^n + \mu_u i_j^p \tag{234}$$

As the commanded force magnitude increases to the left of the transition band toward $-\infty$ (negative force command), the function μ_u approaches 0 and i_j^d approaches i_j^n. Similarly as the commanded force magnitude increases to the right of the transition band toward $+\infty$ (positive force command), the function μ_u approaches 1 and i_j^d approaches i_j^p. For small force commands (within the transition band), i_j^p and i_j^n each contribute a fraction of the value i_j^d such that the fractions add to 1. Which one of i_j^n or i_j^p contributes the larger fraction depends on whether the commanded force is negative or positive, and in either case that contribution decreases as the command approaches 0 (at which point i_j^n and i_j^p contribute equally to desired phase current computation).

4.5.6 Friction Modeling

The position control design objective includes robustness to modeling imperfections and unknown disturbances, and this includes friction forces that naturally occur in

opposition to the relative motion of bodies in contact. In the plant model used in control design only viscous friction has been modeled (by the coefficient $a = \frac{F_v}{M}$ in (4.5.4)); additional friction forces are treated as disturbance forces (the input labeled w in Figure 64) and are included in system simulation in the numerical results presented in this chapter. Friction is a nonlinear phenomenon that is very difficult to model accurately, but numerous models of utility exist in the literature (see [92] for a survey and [93] for an application example). The simple mathematical model of friction described by the equation below and depicted in Figure 67 captures the most recognized friction components:

$$f_f = F_v\dot{x} + (F_c + (F_s - F_c)e^{-(\dot{x}/\nu_s)^2})\ \text{sign}(\dot{x}) \tag{235}$$

where F_s is the static friction, F_c is the Coulomb friction, F_v is the coefficient of viscous friction, and ν_s is the Stribeck velocity. If the static friction coefficient, the Coulomb friction coefficient and gravitational acceleration are denoted μ_s, μ_k and g then

$$F_s = \mu_s g M,$$

and

$$F_c = \mu_k g M$$

The friction model (235) is problematic for computer simulation when the relative velocity of bodies in contact is near zero. To overcome this problem, a suitable neighborhood near zero is selected outside of which the above model is used and inside of which friction force assumes whatever value in the range $[-F_s, F_s]$ that is necessary to hold velocity at zero. This logic, which is used in the simulations of this chapter, can be concisely described as follows

$$|\dot{x}| \leq \nu_s \text{ AND } |f - F_v\dot{x}| \leq F_s \Rightarrow \dot{x} = 0 \tag{236}$$

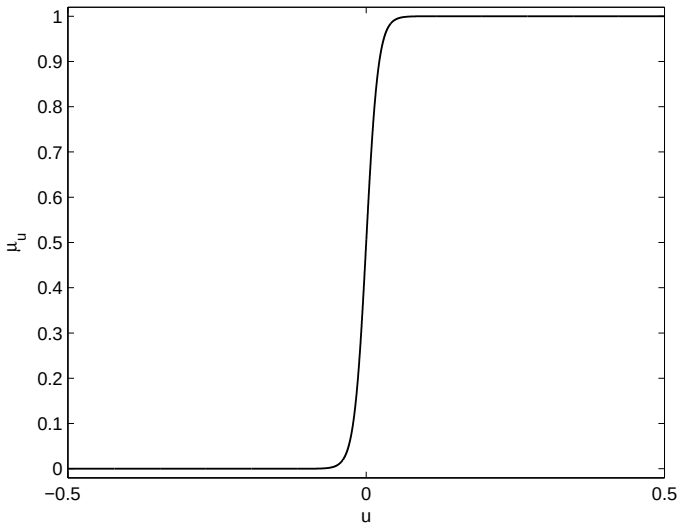

Figure 66: Force-transition smoothing function.

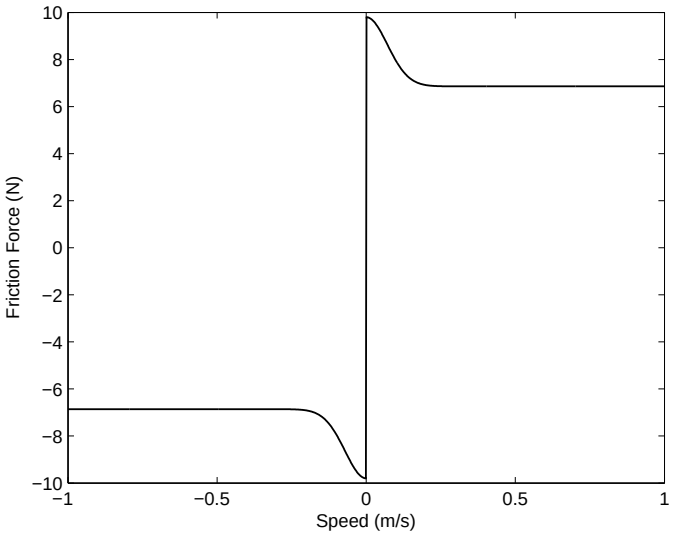

Figure 67: Depiction of typical friction model.

4.5.7 Digital Control Implementation

Microcontroller-based implementation is now the prevalent method of control, and therefore, all subsequent discussion is presented assuming digital implementation. The choice is made to discretize the position controller just derived (as opposed to designing a digital controller for a discretized plant). Discretization is carried out using the forward Euler method where the derivative of the generic signal z is approximated by the difference:

$$\dot{z}(kT_s) \approx \frac{z(kT_s + T_s) - z(kT_s)}{T_s} \tag{237}$$

where T_s represents the microcontroller's sampling period and k represents a discrete-time index. Substitution into the controller equations above leads to the following digital controller (control law and state updates):

$$u[k] = -K_1\hat{\mathbf{x}}[k] - K_2\sigma[k] \tag{238}$$

$$\hat{\mathbf{x}}[k+1] = \hat{\mathbf{x}}[k] + T_s\left(A\hat{\mathbf{x}}[k] + Bu[k] - L\left(C\hat{\mathbf{x}}[k] - y[k]\right)\right) \tag{239}$$

$$\sigma[k+1] = \sigma[k] + T_s\left(y[k] - r[k]\right) \tag{240}$$

The controller output is computed using (238) and then checked to accommodate actuator saturation limit $U_{\max}$ so that the saturated controller output update is given by

$$u[k] = \begin{cases} U_{\max}\,\text{sign}(u[k]) & \text{, if } |u[k]| \geq U_{\max} \\ u[k] & \text{, otherwise} \end{cases} \tag{241}$$

The determination of this saturation limit based on actuator force capability limits and trajectory's task-specified acceleration (force) limit has been explained in Section 4.3 with the help of Figure 58.

4.5.7.1 Integrator Windup Compensation

During the time the actuator is at its saturation limit, when $|u[k]| \geq U_{\max}$, an extra step is needed to ensure that the integrator output is not allowed to windup (increase

inappropriately). One way to do that is to (i) reset the integrator output to a value that produces a control output equal to the actuator's saturation limit and (ii) update the integrator output when the control output would reduce the positioning error and keep the integrator output constant otherwise; the logic is inferred from the signs of the controller output (the force) and the position error. This is summarized as follows

$$|u[k]| \geq U_{\max} \Rightarrow \tag{242}$$

$$\sigma[k] = -(u[k] + K_1\hat{\mathbf{x}}[k])/K_2 \tag{243}$$

$$\sigma[k+1] = \begin{cases} \sigma[k] & \text{, if sign}\left(u[k]\right) = \text{ sign}\left(y[k] - r[k]\right) \\ \sigma[k] + T_s\left(y[k] - r[k]\right) & \text{, otherwise} \end{cases} \tag{244}$$

4.5.7.2 Control System Time Scales

The two-time-scale control structure means that voltage commands are updated at a faster rate than force commands. The force command remains constant during the electrical subsystem control time wherein applied voltages drive phase currents to desired values. The concept is illustrated in Figure 68 depicting the time scales and associated simulation structure. The position controller output (the applied force) is updated every T_s seconds where T_s represents the microcontroller's sampling period. During this interval, the current controller output is updated K_m times where K_m is an integer. Naturally simulated quantities are obtained by computing system response to these commands on a finer mesh using a small simulation step (h seconds as shown on the figure).

4.5.7.3 Sensor and Actuator Resolution

The simulation results presented in this chapter account for the quantization effects encountered in the digital implementation of control systems. Let z represent generically a measured analog quantity (position, current) or a desired analog control output

(phase voltage) and let Q_z be a corresponding quantization parameter such as the resolution of a sensor or an analog to digital converter. The quantized representation z_q of the variable z is given by

$$z_q = Q_z \left\lceil \frac{z}{Q_z} \right\rceil \tag{245}$$

The quantization parameters used are given in Table 14.

4.5.7.4 Simulation Overview

Positioning tasks are simulated in MATLAB using the digital implementation of the two-time-scale control system of Figure 64; the steps are summarized by the pseudo code representation shown in Figure 68. Final selection of simulation parameters such as control gains are made based on best settling time results without introducing instability or violating the final position accuracy requirement. The eigenvalues of the position control system are assumed to be real valued and clustered at λ_r, the estimator eigenvalues are taken to be $\lambda_e = 4\lambda_r$. An initial value of λ_r is selected and is modified manually in small steps until the smallest settling time is achieved; for each selected value the sampling period T_s is set to $0.1\lambda_r$. The current control gain is taken to be 500. The remaining parameters that have not yet been specified are given in Table 16.

Simulation of plant physics is carried out every h seconds (here $h = T_s/100$): Values of position, speed and current (corresponding to time $t_k = kh$), where k represents a discrete time step index, are used in computing new values (corresponding to time $t_k + h$) by integrating the differential equations for these variables. If each of these variables is represented generically by z then (237) gives

$$z(kh + h) \approx \dot{z}(kh)h + z(kh) \tag{246}$$

where $\dot{z}$ represents $\frac{dx}{dt}$, $\frac{d\dot{x}}{dt}$ and $\frac{di}{dt}$ which have been given in (212)–(214). The voltages appearing in (212)–(214) are the current controller outputs defined by (230)–(231)

Table 14: Quantization Parameters

Description	Quantization Parameter Value
Position sensing	10^{-9}
Current sensing	$i_{\max}/2^{12}$
Voltage actuation	$v_{\max}/2^{12}$

and updated every T_m seconds (see Figure 68). The motor flux linkages (43) and output force (48) have been derived in Chapter 2. The friction force is computed according to (235); subsequently the computed speed value is modified according to (236) to account for the so called stick-slip phenomenon.

The phase voltages commanded by the current controller are applied in order to achieve the phase currents needed to produce the force command necessary for trajectory tracking. This force command is generated according to (238), (241) by the position controller every T_s second. Recall from earlier discussion that the phase currents needed to produce this force are found via commutation lookup tables in accordance with (234) and that the currents populating the lookup tables are the heat-minimizing currents discussed in detail in Chapter 3. The state estimates and integrator output values appearing in these equations are found according to (239) and (244) every T_s seconds.

At the completion of the control system simulation for each trajectory, results are examined to ascertain that the main control objectives, namely stability and target-position accuracy, are met, plots are generated and the settling time and average power dissipation are recorded.

4.6 Positioning Performance Assessment

This section presents the numerical results which demonstrate that better settling time is achievable with higher force capability facilitated by high-ripple commutation. The positioning task is defined by $\xi = 500$ mm, $J_{\max} = 1000$ m/s^3, $\Delta x = 10\,\mu$m, and a payload of 10 kg. A solution space, $\mathcal{S}(\xi)$, is generated subsequent to the dynamic

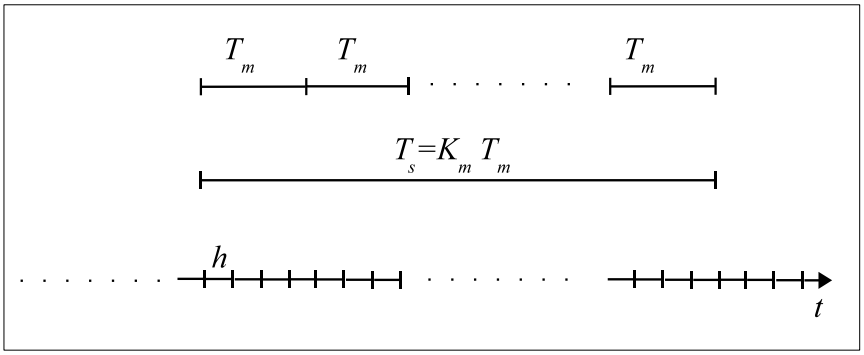

(a) Slow (T_s) and fast (T_m) control intervals.

```
overhead (setting parameters and initial variable values)
loop (main simulation loop): every h seconds
    loop (fast subsystem loop): if mod (t, T_m) = 0
        loop (slow subsystem loop): if mod (t, T_s) = 0
            read and quantize position value
            get position reference command
            compute force command (saturable position controller output)
            update estimator states
            compute desired currents
        end
        read quantized phase current values
        output desired voltages (saturable current-controller output)
    end
    simulate plant physics: compute forces, position, speed, and currents
end
    output results
```

(b) Two-time-scale basic simulation structure.

Figure 68: Two-time-scale control system implementation.

simulation of the positioning scenarios (one associated with each trajectory) and the determination of settling time τ_s and average power dissipation P for each scenario. A solution, $s_p \in \mathcal{S}$, is a point in the solution space specified in terms of settling time and power dissipation:

$$s_p = (\tau_s, P(\tau_s))_p$$

where p is the scenario identifier (and for this case links each solution to a trajectory in Table13). The results from 12 (8 unique) feasible-trajectory simulations for this positioning task are presented in Figures 69–70 for the uncoupled motor and in Figures 71–72 for the coupled motor. The top plot in each figure shows actual position (plotted as solid line) and reference position (plotted as a dashed line). The figures also show actual (solid lines) and computed (dashed lines) speed and force (these are computed from the position reference but are not directly controlled). Table 15 shows settling time and average power dissipation results.

The actuators for the positioning task are taken to be the coupled and uncoupled motors with parameters given in Table 1 (for the case of $\alpha = 1$), and with force capabilities corresponding to commutation with the extreme values of ripple size ($\beta = 0$ and $\beta = 1$). Selection of the force values shown on the table for each speed and ripple value based on the force-speed curves computed in Chapter 3 is illustrated in Section 4.3.1. The position trajectories used (Table 13) have been generated using the minimum time s-curve models in [1], and their graphical depictions have been shown in Figures 59–60 for the uncoupled motor and in Figures 61–62 for the coupled motor.

4.6.1 Comparison of Nominal Trajectory Times

Examination of the nominal trajectory times τ_n (the lower bounds on settling time achievable only with perfect control) for the scenarios specified in Table 13 reveals that, for each motor configuration and each $S_{\max}$ value, the more promising scenarios

Table 15: Solution Space: $\xi = 500$ mm, $J_{\max} = 1000$ m/s^3, $\Delta x = 10\,\mu$m, Load = 10 kg

p	Motor	β	$S_{\max}$ (m/s)	F (N)	File Name	τ_s (s)	P (W)
1	Uncoupled	1	1	145	U_1_1_prof.dat	0.6676	12.3013
2	Uncoupled	1	2	140	U_1_2_prof.dat	0.5187	33.0407
3	Uncoupled	1	3	130	U_1_3_prof.dat	0.5187	33.0407
4	Uncoupled	0	1	70	U_0_1_prof.dat	0.7507	9.8146
5	Uncoupled	0	2	70	U_0_2_prof.dat	0.7027	14.9649
6	Uncoupled	0	3	70	U_0_3_prof.dat	0.7027	14.9649
7	Coupled	1	1	60	C_1_1_prof.dat	0.7874	11.0216
8	Coupled	1	2	60	C_1_2_prof.dat	0.7487	14.9943
9	Coupled	1	3	60	C_1_3_prof.dat	0.7487	14.9943
10	Coupled	0	1	50	C_0_1_prof.dat	0.8562	10.4615
11	Coupled	0	2	50	C_0_2_prof.dat	0.8378	12.5544
12	Coupled	0	3	50	C_0_3_prof.dat	0.8378	12.5544

are associated with unconstrained ripple. For the uncoupled motor, the nominal times of trajectories associated with unconstrained-ripple commutation are 82% (1 m/s speed) and 68% (2 m/s) of those associated with no-ripple commutation. For the coupled motor these percentages are 92% and 89%. If the two motor configurations are both competing for the same task then the uncoupled motor with highest achievable force (highest ripple) and speed provides the fastest trajectory (the lowest τ_n).

4.6.2 Ideal-No-Ripple versus Unconstrained-Ripple Settling

Comparison of the achievable performance with unconstrained-ripple scenarios and the corresponding nominal times, particularly with the no-ripple case reveals that, for each motor configuration and each trajectory-speed value, actual settling times with high ripple commutation are better than the nominal times with low ripple commutation. For the uncoupled motor, comparing scenarios $p = 1 - 3$ in Table 15

Table 16: Positioning Simulation Parameters

Parameter	Symbol	Value
Force smooth transition parameter	δ	$0.1\ N^{-1}$
Stribeck velocity	ν_s	1×10^{-4} m/s
Static friction coefficient	μ_s	0.1
Coulomb friction coefficient	μ_k	0.05
Viscous friction coefficient	F_v	1×10^{-5} N.s/m
Two-time-scale factor	K_m	10

with $p = 4 - 6$ in Table 13 shows

$$\frac{\tau_s|_{\beta=1}}{\tau_n|_{\beta=0}} = \begin{cases} 89.9\% : S_{\max} = 1 \text{ m/s} \\ 74.7\% : S_{\max} = 2,3 \text{ m/s} \end{cases}$$

and for the coupled motor, comparing scenarios $p = 7-9$ in Table 15 with $p = 10-12$ in Table 13 shows

$$\frac{\tau_s|_{\beta=1}}{\tau_n|_{\beta=0}} = \begin{cases} 94.7\% : S_{\max} = 1 \text{ m/s} \\ 92.0\% : S_{\max} = 2,3 \text{ m/s} \end{cases}$$

If the two motor configurations are both competing for the same task then the uncoupled motor with highest achievable force (highest ripple) and speed provides the fastest settling time (lowest τ_s).

Comparisons to the ideal (perfect control, $\tau_s = \tau_n$) no-ripple scenarios is critical for ascertaining that better settling times are achievable with relaxed constraints on force ripple because then it is sufficient to only ascertain that controllers exist to successfully track the higher-ripple faster trajectories. However, it is still valuable to also make comparisons to the no-ripple scenarios under realistic control as in the following section.

4.6.3 No-Ripple versus Unconstrained-Ripple Settling

Comparison of settling times in Table 15 computed under realistic control for both unconstrained and no-ripple scenarios reveals that, for each motor configuration and

each trajectory-speed value, the unconstrained ripple scenarios are favorable. For the uncoupled motor

$$\frac{\tau_s|_{\beta=1}}{\tau_s|_{\beta=0}} = \begin{cases} 88.9\% : S_{\max} = 1 \text{ m/s} \\ 73.8\% : S_{\max} = 2,3 \text{ m/s} \end{cases}$$

and for the coupled motor

$$\frac{\tau_s|_{\beta=1}}{\tau_s|_{\beta=0}} = \begin{cases} 92.0\% : S_{\max} = 1 \text{ m/s} \\ 89.3\% : S_{\max} = 2,3 \text{ m/s} \end{cases}$$

Unlike the results of the previous section (which allow a general association of high ripple commutation and improved positioning performance), the results in this section reflect comparison of best performance with the chosen control structure. With this in mind, the results represent realistic example studies and provide the data for further performance comparisons on the basis of average power dissipation. Higher force (faster positioning) is associated with higher currents and hence a penalty in terms of higher average power dissipation as can be seen from the average dissipation values of Table 15.

4.6.4 Output Force Waveforms

The force plots (the bottom subplots in Figures 69–72) reveal force ripple in actual force production when commanded force is constant. The presence of ripple is expected when high-ripple commutation is used, and in fact is seen to be higher in these plots. In this case, the control system is allowed to command force values that are not available at all displacements (but rather available on average over a spatial period). However another reason for force ripple, common to all cases, is that commutation design assumes that phase currents that would produce a specified force value are available instantaneously. When ripple size is controlled based on current waveform shaping, as is the case in this research, a perfect outcome (exactly as computed) requires a current controller with infinite bandwidth. With finite bandwidth, ripple

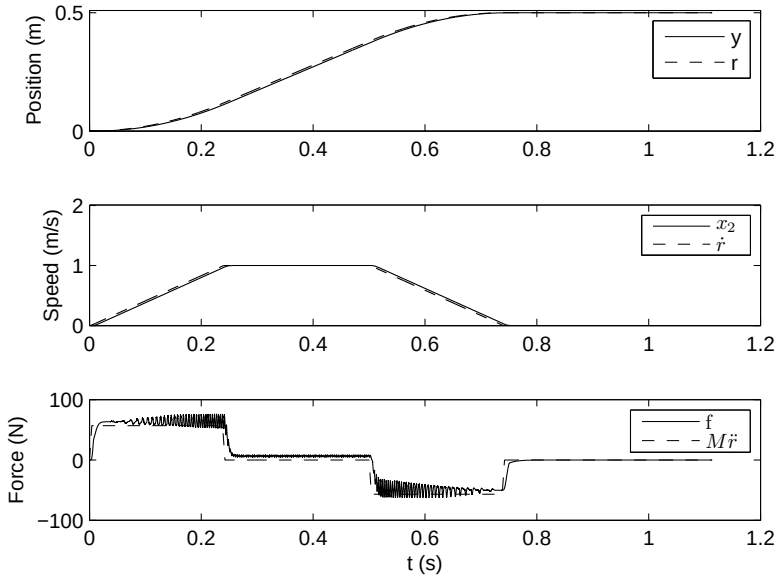

(a) Low force (low ripple).

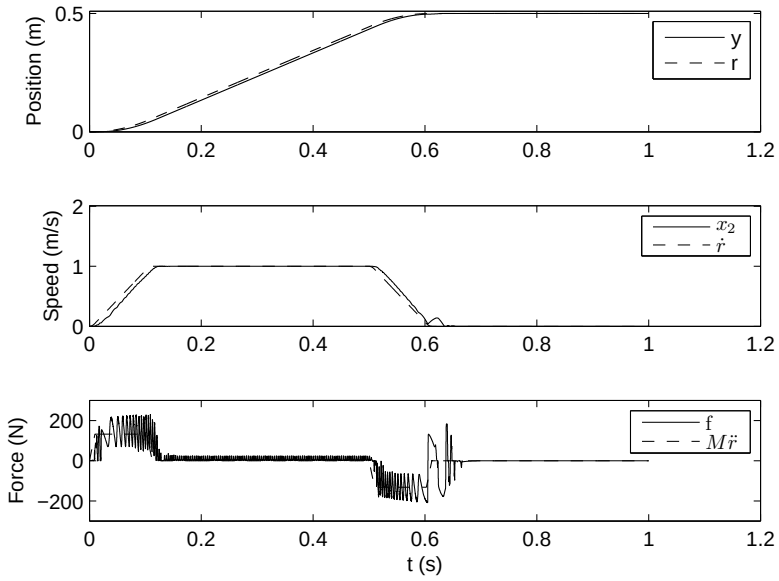

(b) High force (high ripple).

Figure 69: Position task simulation results (uncoupled motor, $S_{\max} = 1$ m/s).

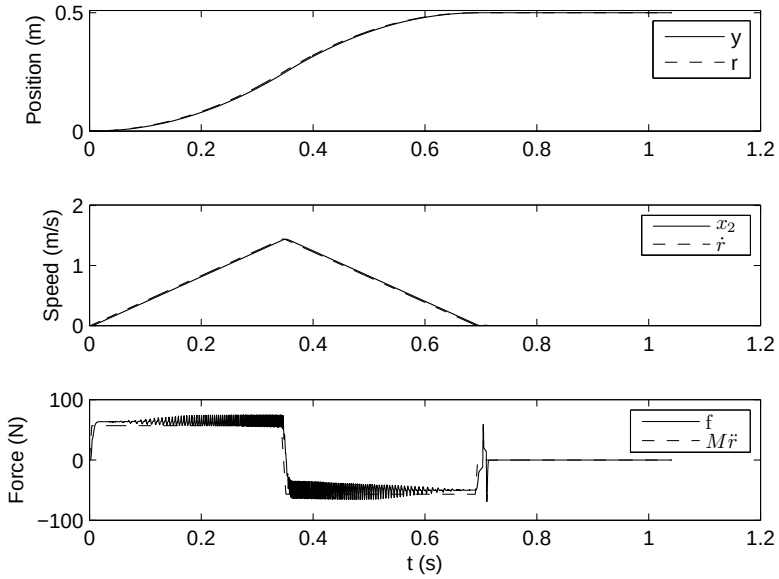

(a) Low force (low ripple).

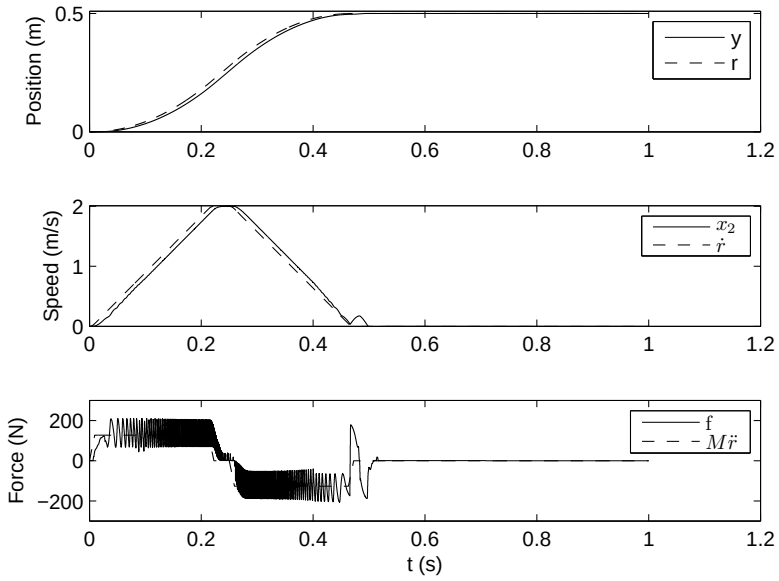

(b) High force (high ripple).

Figure 70: Position task simulation results (uncoupled motor, $S_{\max} = 2$ m/s).

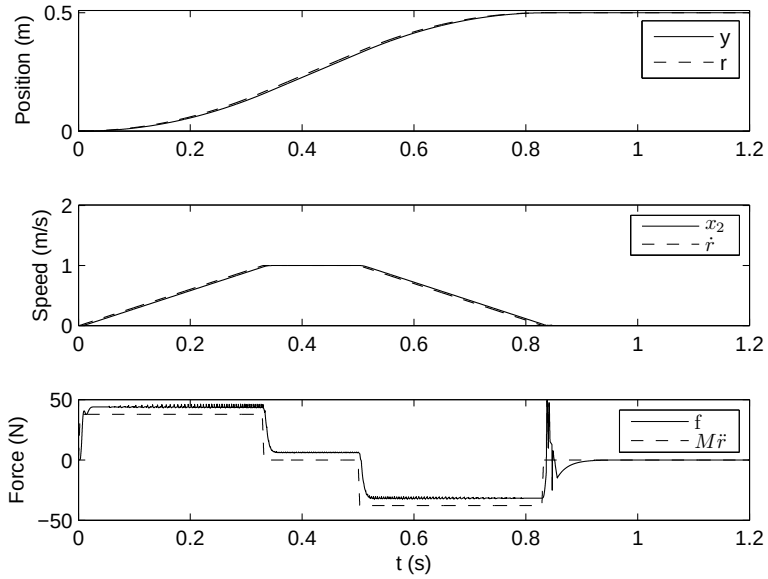

(a) Low force (low ripple).

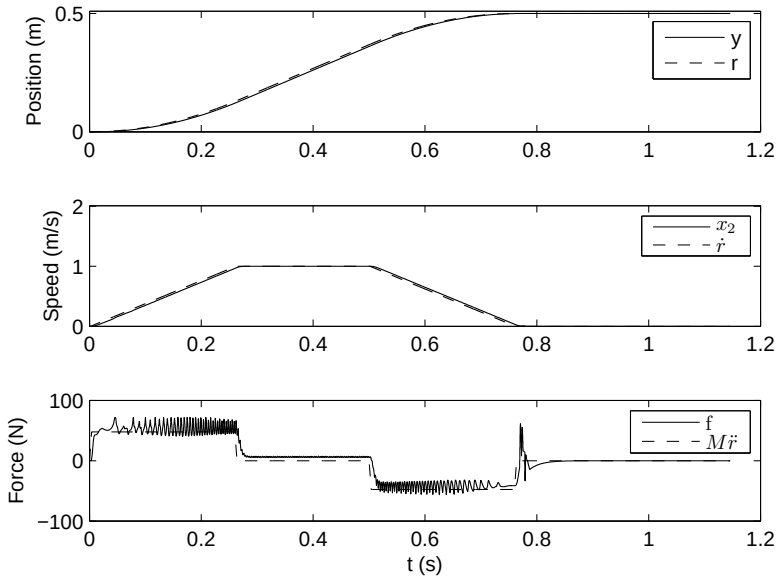

(b) High force (high ripple).

Figure 71: Position task simulation results (coupled motor, $S_{\max} = 1$ m/s).

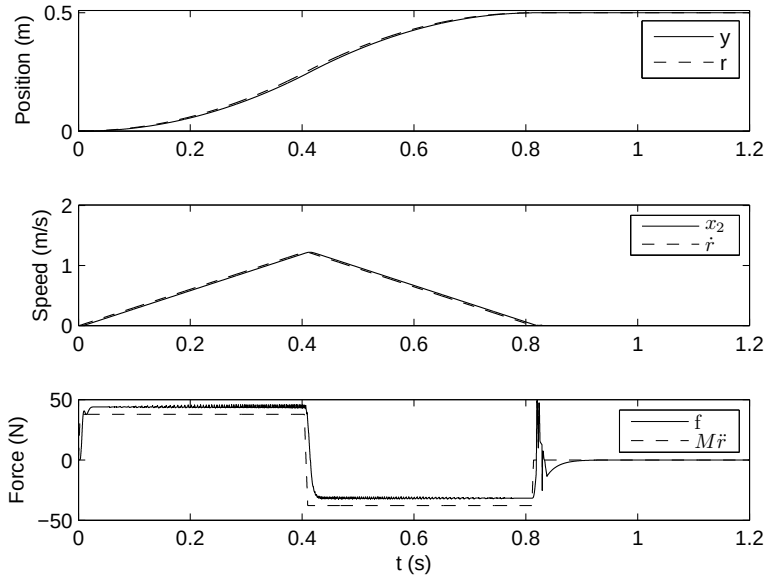

(a) Low force (low ripple).

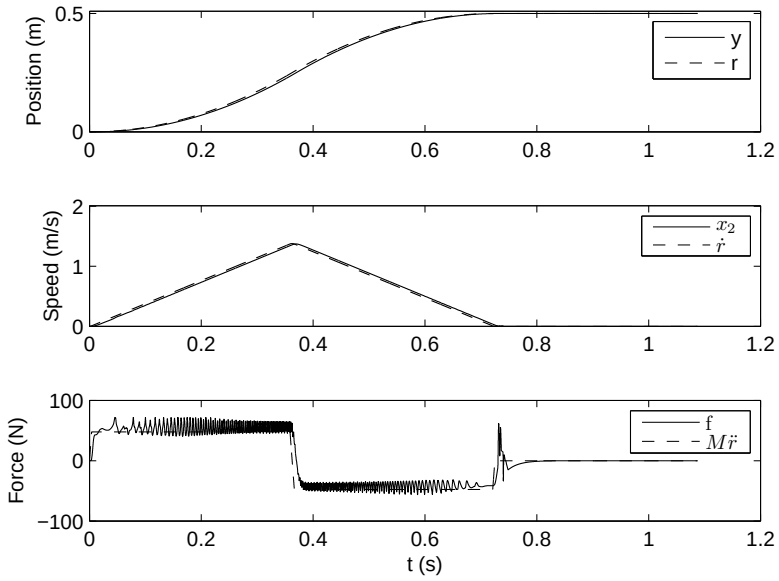

(b) High force (high ripple).

Figure 72: Position task simulation results (coupled motor, $S_{\max} = 2$ m/s).

would increase with increasingly degraded ability to track commanded currents. The high harmonic content of LVR motor current waveforms presents a challenge in command following; it has been noted that while the average torque is most sensitive to the fundamental component of the current, torque ripple is generally most sensitive to the harmonics in the current [94]. Also, current tracking is naturally more challenging at higher speeds of operation with sharper increases in the rate of change of current commands and increases in induced voltage. This is evident in the plots where force ripple increases with increasing speed.

The force plots also show oscillatory behavior at the end of motion. Smoother force profiles are possible with less aggressive control (position controller with smaller eigenvalues). However, the results used in comparative analysis and shown in these figures are based on the fastest settling time while maintaining system stability; this would provide fair comparison since the controlled variable is position not force.

An important issue for future research is the influence of force ripple on residual vibration and ultimately settling time. Some insight has been gained from published research on vibration as discussed in Sections 1.3.2.1 and 4.1.1.5.

4.6.5 Performance of Coupled versus Uncoupled Motors

The simulation results just presented suggest that if the coupled and uncoupled motors compete for the same task, then the uncoupled motor is favorable since it provides faster settling times. However, combining the fact that higher profile speeds provide better settling times and that the coupled motor maintains its force capability over a wider range of speeds, it is reasonable to conclude that if the selected trajectory speed exceeds a certain level (with the uncoupled motor capability declining faster), the coupled motor would become favorable. In addition, by designing the numerical studies for comparing motors that share the same stator bar and all common geometrical parameters (as opposed to having equal volume or mass), the result is a larger

uncoupled motor placing the coupled motor at a disadvantage. This choice has been made in order to emphasize the influence of coupling as opposed to other parameters. In fact, the coupled motor has been shown to provide better acceleration capability in some force range in preliminary comparative results using the same motors in this research [46].

4.6.6 Performance Improvement Premises

There are many steps involved in a complete evaluation of positioning control performance, and so it is important to highlight the premises supporting the claim of settling time improvements (with relaxing force ripple and improving force capability), namely the 'YES' answers to the following questions:

- Does higher-ripple commutation lead to higher force capability? YES ✓
- Do higher force values result in faster motion trajectories? YES ✓
- Do control simulations demonstrate successful tracking of all trajectories (fast and slow)? YES ✓
- Do control simulations show faster realistic-control settling times for high-ripple trajectories than even perfect-control low-ripple trajectories? YES ✓

Having demonstrated positioning performance improvement with increased force ripple, it remains to discuss the trade-offs.

4.6.7 Travel Time, Force Ripple and Power Dissipation Trade-offs

From all previous discussion, it is evident that the set of feasible solutions to point-to-point positioning can be expanded by varying the amount of force ripple permitted in commutation design: a larger set of ripple-specified force values corresponds to a larger set of feasible trajectories, thus expanding the search for better performance under feedback control. This section emphasizes solution selection as represented by

the bottom boxes of the framework in Figure 56 where a choice can be made between faster (hotter) and slower (cooler) feasible solutions.

Recall first two interesting findings from LVR motor optimal excitation studies presented in Chapter 3 in regards to force ripple: (i) force maximization benefits from relaxing force ripple constraints and (ii) minimization of average power dissipation also benefits from relaxing force ripple constraints. It is obvious, on the one hand, that the two optimization goals are antagonistic since higher forces imply higher currents and higher power dissipation, but on the other hand it is possible to choose from slower feasible trajectories that are based on lower force requirements and are therefore associated with lower average power dissipation. Lower force may be combined with lower jerk and/or speed for less aggressive trajectories and less control effort. Control system simulations and subsequent analysis determine the consequences of these choices on positioning performance.

Therefore, whenever the objective of a positioning task is not one of two extremes (the minimum settling time or the minimum average power dissipation), but rather optimizing one goal subject to bounds on the other goal, it is beneficial to have a choice from among a wide range of results (solution space) obtained at the completion of the four-task algorithm in Figure 57. The solution space can be searched for the best solution, $s^* = (t^*, p^*)$, based on whether a limit T^d on travel time or a limit P^d on power dissipation is specified:

$$s^* \in \mathcal{S} \equiv \begin{cases} \text{Find minimum } \tau_s : P(\tau_s) \leq P^d \\ \text{OR} \\ \text{Find minimum } P(\tau_s) : \tau_s \leq T^d \end{cases}$$

4.7 Conclusion

This chapter has demonstrated settling time improvement in point-to-point positioning via several control system simulations; it is demonstrated that tracking of faster positioning reference trajectories (resulting from ripple-facilitated increase in force capability) is possible with realistic closed loop control. A framework is presented that serves as a prescription for planning and assessing positioning task solutions and arriving at improved performance in point-to-point positioning. The steps involved include generation of feasible trajectories for the task, control system design and simulation of the feasible solutions. The results are important for high-throughput positioning applications. In order to reveal the trade-off between fast operation and cool operation, the comparison of settling time results is presented together with the associated average power dissipation.

In the context of high-volume high-throughput positioning, a modest improvement in actuator performance per task may add up to considerable improvement over time. For that reason searching an expanded solution space such as described in this research (for a tradeoff between fast operation and cool operation) is worthwhile. Obvious ways to expand the search include examining additional indices for measuring force ripple and/or expanding the range of ripple-size values (imposed during commutation design) in combination with a wider range of trajectories; for any force ripple value, less aggressive (low jerk and/or speed) trajectories may be compared with more aggressive (higher jerk and/or speed) trajectories. Preliminary studies show improved force capability with higher-ripple commutation for several indices.

CHAPTER 5

CONCLUSIONS

Point-to-point positioning, the controlled motion of an object from one point to another, is the principal task performed by robotic machines in manufacturing automation applications such as circuit board assembly and other product-transfer operations. Because of global competition, automation industries and in turn manufacturers of automation equipment are under great market pressure to minimize production cycle times while meeting increasing demands on production quality and versatility. Complex decision making is required at many levels from human and capital resource management to production planning to controlling the work flow and operation of the individual assembly machines. This research is concerned with performance improvements that can be achieved at the most elementary level in such a hierarchy, namely point-to-point positioning control of the motion actuators inside automation equipment; naturally this would have a direct impact on production cycle time.

This research demonstrates improvement of actuator performance, measured by settling time, in single-axis point-to-point positioning. Four main factors influencing point-to-point positioning are integrated in order to produce a framework that serves to demonstrate the performance improvement and at the same time constitutes a prescription for finding and assessing positioning task solutions: (i) actuator ripple-specified characterization and optimal static commutation, (ii) determination of feasible position trajectories based on optimal capability, (iii) determination of ripple-specified heat-minimizing phase currents to be recalled by the control system indexed by desired force and position, and (iv) position control design and simulation

for performance assessment and comparison to predictions and for examining trade-offs. The general framework is not limited to the motors chosen in this dissertation or linear motors only. No published research has been found that explored this path or produced the same results by some other means.

Achieving and demonstrating performance improvements entails detailed and multi-layered numerical studies; conclusions from these studies are summarized in this chapter and the contributions that resulted from them are highlighted. This chapter also includes several suggestions for future research.

5.1 Summary of Conclusions

Chapter 2 first develops idealized physics-based force models for two LVR motor topologies; magnetic saturation and spatial harmonics are neglected in order to proceed with maximum clarity and at a reduced computational burden. Next, Chapter 2 develops accurate modeling techniques for LVR motors using finite element analysis and least squares. The models are simple in structure, involving cos and tanh functions in a linearly parameterized way. The model coefficients are determined from FEA data using linear least squares methods. The approach has been successfully demonstrated on two coupled LVR motors and three uncoupled LVR motors that differ with respect to tooth geometry. The simplicity of the uncoupled motor allowed the derivation of an analytical model that completely characterizes the motor using functional expressions.

In Chapter 3, the motor models of Chapter 2 are used in conjunction with optimization techniques in solving two static ripple-specified optimal commutation problems, namely force-maximizing optimal commutation (generally finds application in characterization and bang-bang control) and heat-minimizing optimal commutation (generally finds application in force, speed and position control). No published research has accommodated the full range of force ripple in solving these optimization

problems. Moreover, the optimal solutions are obtained without making any assumptions a priori on when to turn a phase on or off or on the number of phases that can be excited simultaneously or how to allocate force production among the excited phases; with few exceptions noted in Section 1.3.2, optimal commutation is typically computed under such assumptions.

The ultimate objective of the force-maximizing problem is to determine the ripple-specified force-speed characteristics. The results show a higher capability with increased ripple allowance; using the higher capability in generating minimum-time s-curve models results in faster positioning trajectories. The objective of heat-minimizing commutation is to determine currents that produce a desired ripple-specified force with minimum power dissipation. The results, which would be recalled during dynamic operation to produce controller commanded force, indicate lower spatial average power dissipation with increased ripple allowance.

The two motor topologies are compared and contrasted. The results of improved force capability and static average power dissipation with increased ripple apply to both but are more pronounced for the uncoupled motor since it exhibits more force ripple and therefore stands to benefit the most from manipulating force ripple. The same optimal commutation formulations are used with both linear and non-linear models with no modification other than in the substitution of the appropriate mathematical expressions. The results show the higher force capability with increased ripple is not a consequence of the magnetic linearity assumptions.

Chapter 4 describes the framework that has been developed to achieve and demonstrate improvement in point-to-point positioning. The control system components and the simulation software are described and the results of multiple positioning tasks are presented. It is shown that the predicted advantage in terms of reduced settling time is confirmed under realistic control system simulation for both LVR motor configurations. The uncoupled motor represents classic linear and rotary variable

reluctance motors whereas the coupled motor exhibits features of both switched and synchronous varieties of variable reluctance motors. Therefore, it is reasonable to expect that the research results are likely to have a broader applicability beyond the specific linear-motion motors studied.

Finally, Chapter 4 discusses the trade-offs among travel time, force ripple and power dissipation; faster operation resulting from allowing high ripple leads to higher average power dissipation. The positioning assessment framework presented here allows for expanding current lookup tables to dynamically match operating speeds rather than conservatively assuming the maximum trajectory speed throughout the motion thus allowing lower average power dissipation at the cost of memory space. Lower dissipation is also possible by choosing lower ripple sizes in commutation design and/or by choosing less aggressive trajectories (lower jerk and/or speed) but this offsets some of the gain in achievable performance. Clearly, expanding the possible solution space is important in the context of high-volume high-throughput positioning so that tradeoff possibilities can be adequately covered.

5.2 New Contributions

1. Modeling of coupled and uncoupled LVR motors

    - Assessment of the accuracy of idealized LVR motor modeling through comparisons to more accurate finite-element based modeling using the coupled motor [41]
    - Analytical modeling using novel functional expressions for coupled (single-phase excitation) and uncoupled LVR motors from accurate numerical data (from finite element analysis or measurement) by employing a novel function fitting approach that removes inaccuracies due to numerical artifacts [44]

2. Solutions to the maximum instantaneous-force production and desired instantaneous force with minimum power dissipation commutation problems

    - Revealing the synchronous-like features of the coupled motor and the associated force control strategy of continuous three-phase excitation [42]
    - Analysis of the internal force production mechanism of LVR motors and the influence of geometry and converter connection [42], [43], [45]
    - Analysis and comparison of idealized coupled and uncoupled LVR motors of varying tooth geometry in terms of their instantaneous acceleration capabilities [46]

3. Solutions to the maximum average-force production and desired average force with minimum power dissipation commutation problems

    (a) Without force ripple specification

    - Comparison of idealized coupled and uncoupled LVR motors in terms of their instantaneous acceleration capabilities and associated performance measures [47]
    - Force-speed characterization and heat minimizing current waveforms for desired average-force production for the uncoupled motor using accurate finite-element based models [48]

    (b) With force ripple specification

    - Production and comparison of force-speed characterization parameterized by ripple for idealized coupled and uncoupled LVR motors
    - Expanded feasible trajectory space for point-to-point positioning by matching minimum-time s-curve trajectories to ripple-based force-speed capability

- Heat-minimizing current waveforms for desired ripple-specified average force production

4. Demonstrating improvements in coupled and uncoupled LVR motor point-to-point positioning performance (reduced settling time) achieved by employing a high-ripple commutation strategy

    - Developing an integrative framework for finding and assessing solutions to the point-to-point positioning control problem for any motor technology
    - Point-to-point position control design for LVR motors incorporating optimal commutation and digital implementation of state-space integral control
    - Analyzing the trade-offs among force ripple, settling time and average power dissipation in the context of single-axis point-to-point positioning

5.3 Future Research

Various opportunities exist for future work including the following:

Experimental Work: Experimental testing of the overall system is necessary for verification of the performance improvements reported in this research.

Actuator Design to Maximize Acceleration: The results of this research, which favor maximizing acceleration for faster point-to-point positioning despite requiring increased force ripple, motivate exploring motor designs that maximize force production and assessing them despite attributes of force or torque production such as ripple that are perceived negative. The results in Chapter 3, which are not all intuitively obvious and which reveal the influence of tooth geometry and motor-converter wire connections on force capability, provide further motivation to explore all design factors and to subsequently use the framework presented here to assess how they ultimately influence positioning performance.

Consideration of Additional Force Ripple Indices: In this research, the 1-norm is used in ripple quantification. The choice of this ripple index is a result of preliminary research indicating lower heat generation. However, preliminary research also showed striking differences in the shapes of force waveforms depending on the ripple index used. Research into input force shaping and its influence on residual vibration, current tracking, and position or speed control might benefit from considering other norms.

Accurate Thermal Modeling: Thermal modeling is important in applications where productivity is limited by steady state temperature. Also, heat losses are not limited to copper losses; other sources of heat include hysteresis losses, eddy-current losses, skin effect losses and mechanical losses and their inclusion would facilitate more accurate prediction of the achievable positioning performance.

Complete Model for the Coupled Motor: Unlike the simpler uncoupled motor, a complete symbolic representation of the coupled motor model is hard to come by, but extra effort to find one is well motivated. Numerical modeling based on finite element data remains an option but it is inferior because of added requirements on memory space and time.

Improved Dynamic Commutation: The excitation currents used in this research come from lookup tables that correspond to the highest profile speed to ensure voltage constraints are not violated at any point during dynamic operation, yet dynamic operation is not constantly at the maximum speed. Therefore, as computation power increases, it may be possible to improve average power dissipation by saving phase current lookup tables that are indexed by instantaneous speed as well as position and desired force. The immediate result would be a reduction in average power dissipation.

Consideration of Structure Vibration: It is important to find out how the non-conventional high force-ripple commutation strategy adopted in this research influences residual vibration and ultimately settling time. The discussion on published research in Sections 1.3.2.1 and 4.1.1.5 motivates the assessment of positioning performance after integrating vibration suppression techniques (particularly command shaping), optimal excitation and control design to find out if advances in vibration control methods will favor faster high-ripple LVR motor operation to slower no-ripple LVR motor operation in the same way that such advances favored robotic systems with faster light structures requiring specialized vibration control to slower structurally stiffened and dampened systems requiring no specialized vibration control.

Further Improvement of Feedback Control Design: It is prudent to explore additional feedback control techniques, for example robust and adaptive schemes, in search of the best control structure, especially in experimental implementation where performance assessment takes into account non-modeled disturbances and temperature rise from all heat sources.

There remain several opportunities for expanding on the research presented in this dissertation; however, it provides a novel framework for identifying, implementing and assessing feasible solutions for point-to-point positioning tasks. In a larger scope, the framework can be implemented in the virtual prototyping of positioning systems by seeking and assessing the positioning performance of force-maximizing designs. The framework, while implemented in this research using LVR motors (thus filling a void in the application of that particular technology in positioning systems), is generally applicable to any type of linear or rotary motor.

REFERENCES

[1] Y. O. Kim and I. J. Ha, "Time-optimal control of a single-DOF mechanical system considering actuator dynamics," *IEEE Transactions on Control Systems Technology*, vol. 11, no. 6, pp. 919–932, 2003.

[2] M. W. Spong and M. Vidyasagar, *Robot Dynamics and Control*. New York, USA: Wiley, 1989.

[3] I. Boldea and S. A. Nasar, *Linear Electric Actuators and Generators*. Cambridge, UK: Cambridge University Press, 1997.

[4] J. F. Gieras and Z. J. Piech, *Linear Synchronous Motors: Transportation and Automation Systems*. Boca Raton, FL: CRC Press, 1999.

[5] F. Aghili, M. Buehler and J. M. Hollerbach, "Torque ripple minimization in direct drive systems," *Proceedings of the IEEE Conference on Intelligent Robots and Systems IROS*, Victoria BC, Canada, vol. 2, pp. 794–799, October 1998.

[6] R. Pupadubsin, N. Chayopitak, D. G. Taylor, N. Nulek, S. Kachapornkul, P. Jitkreeyarn, P. Somsiri and K. Tungpimolrut, "Adaptive integral sliding-mode position control of a coupled-phase linear variable reluctance motor for high-precision applications," *IEEE Transactions on Industry Applications*, vol. 48, no. 4, pp. 1353–1363, 2012.

[7] S. Kato (1999). Recent development of NSK direct-drive motors. *Motion and Control*, no. 6. Retrieved from http://www.jp.nsk.com

[8] Universal Instruments Corporation (2000). High-accuracy and high-throughput placement systems. Retrieved from http://www3.uic.com

[9] E. R. Laithwaite, *A History of Linear Electric Motors*. London, UK: Macmillan, 1987.

[10] S. A. Nasar and I. Boldea, *Linear Electric Motors*. Englewood Cliffs, NJ: Prentice Hall, 1987.

[11] G. W. McLean, "Review of recent progress in linear motors," *IEE Proceedings: Part B*, vol. 135, no. 6, pp. 380–416, 1988.

[12] T. J. E. Miller (editor), *Switched Reluctance Motor Drives: A Reference Book of Collected Papers*. Ventura, CA: Intertec Communications, 1988.

[13] T. J. E. Miller, *Switched Reluctance Motors and their Control*. Oxford, UK: Clarendon Press, 1993.

[14] H. H. Moghbelli and M. H. Rashid, "Performance review of the switched reluctance motor drives," *Proceedings of the 34th Midwest Symposium on Circuits and Systems*, vol. 1, pp. 162–165, 1991.

[15] R. Krishnan, *Switched Reluctance Motor Drives, Modeling, Simulation, Analysis, Design and Applications*. Boca Raton, USA: CRC Press, 2001.

[16] T. J. E. Miller, *Electronic Control of Switched Reluctance Machines*. Oxford, UK: Reed Educational and Professional Publishing Ltd, 2001.

[17] K. Vijayakumar, R. Karthikeyan, S. Paramasivam, R. Arumugam and K. N. Srinivas, "Switched reluctance motor modeling, design, simulation, and analysis: A comprehensive review," *IEEE Transactions on Magnetics*, vol. 44, no. 12, pp. 4605–4617, 2008.

[18] J. Cros and P. Viarouge, "Synthesis of high performance PM motors with concentrated windings," *IEEE Transactions on Energy Conversion*, vol. 17, no. 2, pp. 248–253, 2002.

[19] F. Magnussen and C. Sadarangani, "Windings factor on Joule losses of permanent magnet machines with concentrated windings," *Proceedings of IEEE International Electric Machines and Drives Conference*, Madison, WI, pp. 333–339, June 2003.

[20] W. Wrobel and P. H. Mellor, "Design considerations of a direct drive brushless PM machine with concentrated windings," *Proceedings of IEEE International Electric Machines and Drives Conference*, San Antonio, TX, pp. 655–658, May 2005.

[21] H. D. Chai, "Permeance model and reluctance force between toothed structures," *Proceedings of the 2nd Annual Symposium on Incremental Motion Control Systems and Devices*, Urbana-Champaign, IL, pp. K1–K12, April 1973.

[22] J. P. Pawletko and H. D. Chai, "Linear step motors," *Proceedings of the 2nd Annual Symposium on Incremental Motion Control Systems and Devices*, Urbana-Champaign, IL, pp. V1–V11, April 1973.

[23] J. P. Pawletko and H. D. Chai, "Linear stepping motor with uncoupled phases," *Proceedings of the 13th Annual Symposium on Incremental Motion Control Systems and Devices*, Urbana-Champaign, IL, pp. 245–250, May 1984.

[24] J. P. Pawletko, D. G. Manzer and J. Ish-Shalom, "A direct drive actuator for cartesian robots," *Proceedings of the ASME Winter Annual Meeting*, Miami, FL, pp. 285–290, November 1985.

[25] J. Ish-Shalom and D. G. Manzer, "Commutation and control of step motors," *Proceedings of the 14th Annual Symposium on Incremental Motion Control Systems and Devices*, Urbana-Champaign, IL, pp. 283–292, June 1985.

[26] D. G. Manzer, M. Varghese and J. S. Thorp, "Variable reluctance motor characterization," *IEEE Transactions on Industrial Electronics*, vol. 36, no. 1, pp. 56–63, 1989.

[27] N. Chayopitak and D. Taylor, "Nonlinear magnetic circuit model of a linear variable reluctance motor," *Proceedings of the 36th IEEE Southeastern Symposium on System Theory*, Atlanta, GA, pp. 170–174, 2004.

[28] N. Chayopitak and D. Taylor, "Dynamic simulation of a linear variable reluctance motor using coupled network models," *Proceedings of the 36th IEEE Southeastern Symposium on System Theory*, Atlanta, GA, pp. 160–164, 2004.

[29] N. Chayopitak, R. Pupadubsin, N. Nulek, S. Kachapornkul, P. Jitkreeyarn, P. Somsiri and K. Tungpimolrut, "Development of a nonlinear magnetic circuit model for linear variable reluctance motor," *Proceedings of the International Conference on Electrical Machines and Systems*, Incheon, Korea, pp. 1506–1511, 2010.

[30] S. M. Jang, J. H. Park, D. J. You, J. Y. Choi, Y. H. Kim and H. K. Sung, "Dynamic characteristics analysis of linear switched reluctance motor," *Proceedings of the Eighth International Conference on Electrical Machines and Systems*, vol. 1, pp. 529–534, 2005.

[31] A. E. Santo, M. R. A. Calado and C. M. P. Cabrita, "Linear switched reluctance actuator modelling with flux tubes considering saturation effects," *Proceedings of the 18th International Conference on Electrical Machines*, Vilamoura, Portugal, pp. 1–6, 2008.

[32] J. G. Amoros and G. P. Andrada, "Magnetic circuit analysis of a linear switched reluctance motor," *Proceedings of the 13th European Conference on Power Electronics and Applications*, Barcelona, Spain, pp. 1–9, 2009.

[33] U. S. Deshpande, J. J. Cathey and E. Richter, "High-force density linear switched reluctance machine," *IEEE Transactions on Industry Applications*, vol. 31, no. 2, pp. 345–352, 1995.

[34] J. Corda and M. Wilkinson, "Modelling of static thrust characteristics of cylindrical linear switched reluctance actuator," *Proceedings of the 7th International Conference on Electrical Machines and Drives*, Durham, UK, pp. 354–358, September 1995.

[35] C. T. Liu and J. L. Kuo, "Experimental investigation and 3D modelling of linear variable-reluctance machine with magnetic-flux decoupled windings," *IEEE Transactions on Magnetics*, vol. 30, no. 6, pp. 4737–4739, 1994.

[36] J. Corda and B. Ouhab, "Electromagnetic design optimisation of a linear-cylindrical variable-reluctance motor," *Proceedings of the 9th International Conference on Electrical Machines and Drives*, Canterbury, UK, pp. 276–280, September 1999.

[37] K. Takayama, Y. Takasaki, R. Ueda and T. Sonoda, "Thrust force distribution on the surface of stator and rotor poles of switched reluctance motor," *IEEE Transactions on Magnetics*, vol. 25, no. 5, pp. 3997–3999, 1989.

[38] K. Hirata, Y. Kagami, M. Yanosaka, Y. Ishihara and T. Todaka, "Thrust calculation of linear pulse motors using a combined technique employing the finite element method and the permeance analysis method," *IEEE Transactions on Magnetics*, vol. 28, no. 2, pp. 1394–1397, 1992.

[39] J. G. Amoros, B. B. Molina and P. A. Gascon, "Simulation of linear switched reluctance motor drives," *Proceedings of the 14th European Conference on Power Electronics and Applications*, Birmingham, pp. 1–9, 2011.

[40] W. C. Gan and N. C. Cheung, "Development and control of a low-cost linear variable-reluctance motor for precision manufacturing automation," *IEEE/ASME Transactions on Mechatronics*, vol. 8, no. 3, pp. 326–333, 2003.

[41] D. G. Taylor and R. Ahmed, "Analysis of a linear variable reluctance motor with magnetically coupled phases," *Proceedings of the 34th IEEE Southeastern Symposium on System Theory*, Huntsville, AL, pp. 219–223, March 2002.

[42] D. G. Taylor and R. Ahmed, "Force control of a linear variable reluctance motor with magnetically coupled phases," *Proceedings of the 34th IEEE Southeastern Symposium on System Theory*, Huntsville, AL, pp. 229–233, March 2002.

[43] D. G. Taylor and R. Ahmed, "Optimization based design of excitation currents for linear variable reluctance motors," *Proceedings of the IASTED International Conference on Applied Simulation and Modeling*, Crete, Greece, pp. 627–632, June 2002.

[44] D. G. Taylor and R. Ahmed, "Modeling linear variable reluctance motors by finite element analysis and least squares methods," *Proceedings of the IASTED International Conference on Applied Simulation and Modeling*, Crete, Greece, pp. 633–637, June 2002.

[45] D. G. Taylor and R. Ahmed, "Current limited optimal excitation of magnetically coupled linear variable reluctance motors," *Proceedings of the IEEE International Electric Machines and Drives Conference*, Madison, WI, pp. 857–860, June 2003.

[46] D. G. Taylor and R. Ahmed, "Comparative analysis of linear variable reluctance motors with coupled and uncoupled flux paths," *Proceedings of the 36th IEEE Southeastern Symposium on System Theory*, Atlanta, GA, pp. 436–440, March 2004.

[47] R. Ahmed and D. G. Taylor, "Optimal excitation of linear variable reluctance motors with coupled and uncoupled flux paths," *Proceedings of the IEEE International Symposium on Industrial Electronics*, Montreal, Canada, pp. 2498–2503, July 2006.

[48] R. Ahmed and D. G. Taylor, "Assessment of linear variable reluctance motor performance limits via finite element modeling," *Proceedings of the International Conference on Electrical Machines*, Chania, Greece, 6 pages on CD-ROM, September 2006.

[49] S. J. Evangeline and S. S. Kumar, "Torque ripple minimization of switched reluctance drives - a survey," *IET Conference on Power Electronics, Machines and Drives (PEMD 2010),* pp. 1–6, 2010.

[50] C. Pavlitov, H. Chen, Y. Gorbounov, T. Tashev, T. Georgiev and W. Xing, "Switched reluctance motor torque ripples reduction by the aid of adaptive reference model," *2010 International Symposium on Power Electronics, Electrical Drives, Automation and Motion (SPEEDAM 2010),* pp. 1276–1279, 2010.

[51] H. Ding and J. Wu, "Point-to-point motion control for a high-acceleration positioning table via cascaded learning schemes," *IEEE Transactions on Industrial Electronics*, vol. 54, no. 5, pp. 2735–2744, 2007.

[52] S. W. Zhao, N. C. Cheung, W. C. Gan and J. M. Yang, "High-precision position control of a linear-switched reluctance motor using a self-tuning regulator," *IEEE Transactions on Power Electronics*, vol. 25, no. 11, pp. 2820–2827, 2010.

[53] D. G. Taylor and N. Chayopitak, "Time-optimal position control of electric motors with steady-state temperature constraints," *Proceedings of IEEE International Symposium on Industrial Electronics*, Montreal, Canada, pp. 3142–3146, July 2006.

[54] T. H. Kim, D. H. Lee and J. W. Ahn, "Advanced non-linear logic torque sharing function of SRM for torque ripple reduction," *Proceedings of the 31st International Telecommunication Energy Conference, INTELEC 2009,* pp. 1–4, 2009.

[55] R. Gobbi and K. Ramar, "Optimisation techniques for a hysteresis current controller to minimise torque ripple in switched reluctance motors," *IET Electric Power Applications,* pp. 453–460, 2009.

[56] L. Zhengyu, D. S. Reay, B. W. Williams and H. Xiangning, "On-line torque estimation in a switched reluctance motor for torque ripple minimisation," *IEEE International Symposium on Industrial Electronics,* vol. 2, pp. 981–985, 2004.

[57] S. L. Ho, X. D. Xue and K.W. E. Cheng, "Optimization and evaluation of torque-sharing functions for torque ripple minimization in switched reluctance motor drives," *IEEE Transactions on Power Electronics,* vol. 24, no. 5, pp. 2076–2090, 2009.

[58] M. Shirahase, S. Morimoto and M. Sanada, "Torque ripple reduction of SRM by optimization of current reference," *International Power Electronics Conference (IPEC - Sapporo)*, pp. 2501–2507, 2010.

[59] B. S. Lee, H. K. Bae, P. Vijayraghavan and R. Krishnan, "Design of a linear switched reluctance machine," *IEEE Transactions on Industry Applications*, vol. 36, no. 6, pp. 1571–1580, 2000.

[60] H. C. Lovatt and J. M. Stephenson, "Computer-optimised current waveforms for switched-reluctance motors," *IEE Proceedings, Electric Power Applications*, vol. 141, no. 2, pp. 45–51, 1994.

[61] H. C. Lovatt and J. M. Stephenson, "Computer-optimised smooth-torque current waveforms for switched-reluctance motors," *IEE Proceedings, Electric Power Applications*, vol. 144, no. 5, pp. 310–316, 1997.

[62] N. Chayopitak and D. Taylor, "Design of linear variable reluctance motor using computer-aided design assistant," *Proceedings of the IEEE International Electric Machines and Drives Conference*, San Antonio, TX, pp. 1569–1575, May 2005.

[63] P.H. Meckl and W.P. Seering, "Feedforward control techniques to achieve fast settling time in robots," *Proceedings of the 1986 American Control Conference*, Seattle, WA, vol. 3, pp. 1913–18, June 1986.

[64] S. Rhim, A. P. Hu, N. Sadegh and W. Book, "Combining a multirate repetitive learning controller with command shaping for improved flexible manipulator control," *Transactions of the ASME Journal of Dynamic Systems, Measurement and Control*, vol. 123, no. 3, pp. 385–390, September 2001.

[65] E. Pereira, S. S. Aphale, V. Feliu and S. O. Reza, "Integral resonant control for vibration damping and precise tip-positioning of a single-link flexible manipulator," *IEEE/ASME Transactions on Mechatronic*, vol. 16, no. 2, pp. 232–240, April 2011.

[66] S. C. Bessette, C. A. Coots, J. E. York and A. Zalesski, "Method and apparatus for vibration reduction/control in a variable reluctance linear motor," U.S. Patent 6 078 114, June 20, 2000.

[67] W. Singhose, N. Singer and W. Seering, "Comparison of command shaping methods for reducing residual vibration," *Proceedings of the Third European Control Conference. ECC 95*, vol. 2, pp. 1126–31, September 1995.

[68] P. H. Meckl and W. P. Seering, "Reducing residual vibration in systems with uncertain resonances," *IEEE Control System Magazine*, vol. 8, no. 2, pp. 73–76, April 1988.

[69] P. H. Meckl and W. P. Seering, "Controlling velocity-limited systems to reduce residual vibration," *Proceedings of the 1988 IEEE International Conference on Robotics and Automation*, vol. 3, pp. 1428–1433, April 1988.

[70] M. Kenison and W. Singhose, "Concurrent design of input shaping and proportional plus derivative feedback control," *Transactions of the ASME Journal*

of Dynamic Systems, Measurement and Control, vol. 124, no. 3, pp. 398–405, September 2002.

[71] C. Rao and L. Du, "An active control method for vibration isolation of precision equipments," *ISECS International Colloquium on Computing, Communication, Control, and Management. CCCM 2009*, vol. 3, pp. 368–371, August 2009.

[72] K. Adamiak, D. Barlow, C. P. Choudhury, P. M. Cusack, G. E. Dawson, A. R. Eastham, B. Grady, E. Ho, Y. Hongping, L. Pattison and J. Welch, "The switched reluctance motor as a low-speed linear drive," *Proceedings of the International Conference on MagLev and Linear Drives*, Las Vegas, NV, pp. 39–43, May 1987.

[73] D. Matt, R. Goyet, J. Lucidarme and C. Rioux, "Longitudinal-field multi-airgap linear reluctance actuator," *Electric Machines and Power Systems*, vol. 13, no. 5, pp. 299–313, 1987.

[74] J. Lucidarme, A. Amouri and M. Poloujadoff, "Optimum design of longitudinal field variable reluctance motors—application to a high performance actuator," *IEEE Transactions on Energy Conversion*, vol. 8, no. 3, pp. 357–361, 1993.

[75] U. S. Deshpande, "Two-dimensional finite-element analysis of a high-force-density linear switched reluctance machine including three-dimensional effects," *IEEE Transactions on Industry Applications*, vol. 36, no. 4, pp. 1047–1052, 2000.

[76] T. Suzuki, "DD-type linear motor systems and their applications," *Journal of Robotics and Mechatronics*, vol. 1, pp. 328–332, 1989.

[77] R. R. Hwang, S. Y. Fwu, M. D. Wu and J. S. Chen, "Toward the servo design of a linear variable reluctance motor drive," *Journal of Control Systems and Technology*, vol. 5, no. 3, pp. 181–193, 1997.

[78] H. Yamada, T. Hamajima, S. Xiang and N. Nishizawa, "Six-phase cylindrical linear pulse motor as linear oscillatory actuator," *IEEE Transactions on Magnetics*, vol. 23, no. 5, pp. 2841–2843, 1987.

[79] J. Corda and E. Skopljak, "Linear switched reluctance actuator," *Proceedings of the 6th International Conference on Electrical Machines and Drives*, Oxford, UK, pp. 535–539, September 1993.

[80] J. P. Pawletko, "Dynamic responses and control aspects of linear stepping motors," *Proceedings of the 5th Annual Symposium on Incremental Motion Control Systems and Devices*, Urbana-Champaign, IL, May 1976, pp. P1–P17.

[81] W. C. Gan, N. C. Cheung and L. Qiu, "Position control of linear switched reluctance motors for high-precision applications," *IEEE Transactions on Industry Applications*, vol. 39, no. 5, pp. 1350–1362, 2003.

[82] J. Pan, N. C. Cheung and J. Yang, "High-precision position control of a novel planar switched reluctance motor," *IEEE Transactions on Industrial Electronics*, vol. 5, no. 11, pp. 1644–1652, 2005.

[83] N. Chayopitak and D. G. Taylor, "Fourier series methods for optimal periodic position control," *Proceedings of IEEE Conference on Decision and Control,* San Diego, CA, pp. 1221–1226, December 2006.

[84] R. Pupadubsin, N. Chayopitak, N. Nulek, S. Kachapornkul, P. Jitkreeyarn, P. Somsiri and K. Tungpimolrut, "Position control of a linear variable reluctance motor with magnetically coupled phases," *Proceedings of Elect. Eng./ECTI-CON*, Chiangmai, Thailand, May 2010, pp. 1031–1035.

[85] R. Pupadubsin, N. Chayoptak, N. Nulek, S. Kachapornkul, P. Jitkreeyarn, P. Somsiri and K. Tungpimolrut, "An improved adaptive mode sliding position control of a linear variable reluctance motor," *Proceedings of the 2010 International Conference on Electrical Machines and Systems, ICEMS2010*, Incheon, Korea, pp. 1583–1588, October 2010.

[86] P. C. Kjaer, J. J. Gribble and T. J. E. Miller, "High-grade control of switched reluctance machines," *Conference Record of IEEE Industry Applications Society Annual Meeting,* San Diego, CA, vol. 1, pp. 92–100, October 1996.

[87] P. C. Kjaer, J. J. Gribble and T. J. E. Miller, "Dynamic testing of switched reluctance motors for high-bandwidth actuator applications," *IEEE/ASME Transactions on Mechatronics*, vol. 2, no. 2, pp. 123–135, 1997.

[88] G. G. Lopez, P. C. Kjaer and T. J. E. Miller "High-grade position estimation for SRM drives using flux linkage/current correction model," *IEEE Transactions on Industry Applications,* vol. 35, no. 4, pp. 859–869, 1999.

[89] D. G. Luenberger, *Linear and Nonlinear Programming*, 2nd Edition. Reading, MA: Addison-Wesley, 1984.

[90] *Optimization Toolbox User's Guide*, for use with MATLAB. Natick, MA: The MathWorks, 2001.

[91] D. G. Taylor, *Control System Design*, ECE 4550 Lecture Notes, Atlanta: Georgia Institute of Technology, 2012.

[92] B. H. Armstrong, P. Dupont and C. Canudas de Wit, "A survey of models, analysis tools and compensation methods for the control of machines with friction," *Automatica*, no. 30, pp. 1083–1138, 1994.

[93] D. Karnopp, "Computer simulation of stick-slip friction in mechanical dynamic systems," *ASME Journal of Dynamic Systems, Measurement and Control*, vol. 107, pp. 100–103, 1985.

[94] P. L. Chapman, S. D. Sudhoff, "Design and precise realization of optimized current waveforms for an 8/6 switched reluctance drive," *IEEE Transactions on Power Electronics*, vol. 17, no. 1, pp. 76–83, 2002.

VITA

Raga Ahmed has a bachelor of science degree from the University of Khartoum, Khartoum, Sudan and a master's of electrical engineering degree from Rice University, Houston, Texas. Her most recent experience, while pursuing a doctoral degree at Georgia Institute of Technology, has been in the academic field. She taught electrical engineering classes (2009-2012) at the University of Tennessee, Chattanooga (UTC), the first two years as twice the recipient of a teaching fellowship from UTC's Office of Equity and Diversity. At UTC, she taught both graduate students (modern control systems) and undergraduate students (digital circuits, electrical circuits, and electrical circuits laboratory). Prior to that she was a Student Teacher Enhancement Partnership (STEP) fellow (2006-2007) with the Center for the Enhancement of Teaching and Learning (CETL) at Georgia Institute of Technology where she applied her CETL theoretical and hands-on training locally in classrooms and in teacher training courses. Her professional experience includes working in a joint venture setting as a part-time research engineer (2001-2004) conducting motor design optimization for Litton PolyScientific (by 2004, it changed to Northrop Grumman and then Moog) and designing Microsoft Access event-driven user interfaces to be used with production costing and billing software for electric utilities at Operation Simulation Associates, Ringgold, Georgia (1994-1997). Her doctoral research lead to the publications listed below.

Publications:

1. R. Ahmed and D. G. Taylor, "Assessment of linear variable reluctance motor performance limits via finite element modeling," *Proceedings of the International Conference on Electrical Machines*, Chania, Greece, 6 pages on CD-ROM,

September 2006.

2. R. Ahmed and D. G. Taylor, "Optimal excitation of linear variable reluctance motors with coupled and uncoupled flux paths," *Proceedings of the IEEE International Symposium on Industrial Electronics*, Montreal, Canada, pp. 2498–2503, July 2006.

3. D. G. Taylor and R. Ahmed, "Comparative analysis of linear variable reluctance motors with coupled and uncoupled flux paths," *Proceedings of the 36th IEEE Southeastern Symposium on System Theory*, Atlanta, GA, pp. 436–440, March 2004.

4. D. G. Taylor and R. Ahmed, "Current limited optimal excitation of magnetically coupled linear variable reluctance motors," *Proceedings of the IEEE International Electric Machines and Drives Conference*, Madison, WI, pp. 857–860, June 2003.

5. D. G. Taylor and R. Ahmed, "Modeling linear variable reluctance motors by finite element analysis and least squares methods," *Proceedings of the IASTED International Conference on Applied Simulation and Modeling*, Crete, Greece, pp. 633–637, June 2002.

6. D. G. Taylor and R. Ahmed, "Optimization based design of excitation currents for linear variable reluctance motors," *Proceedings of the IASTED International Conference on Applied Simulation and Modeling*, Crete, Greece, pp. 627–632, June 2002.

7. D. G. Taylor and R. Ahmed, "Force control of a linear variable reluctance motor with magnetically coupled phases," *Proceedings of the 34th IEEE Southeastern Symposium on System Theory*, Huntsville, AL, pp. 229–233, March 2002.

8. D. G. Taylor and R. Ahmed, "Analysis of a linear variable reluctance motor with magnetically coupled phases," *Proceedings of the 34th IEEE Southeastern Symposium on System Theory*, Huntsville, AL, pp. 219–223, March 2002.